Master Thesis
in the program
(M.Sc.) **Climate Physics**

Modelling the upper-tropospheric rotational flow

Faculty of Mathematics and Natural Sciences, Christian-Albrechts-University, Kiel

GEOMAR Helmholtz Centre for Ocean Research Kiel

submitted by **Wolfgang Wicker**
Student Number: 1014728

Kiel, 29.05.2020

Supervisor:	Prof. Dr. Richard J. Greatbatch
Second assessor:	Prof. Dr. Martin Claus

Abstract

For this thesis, a fully non-linear barotropic vorticity equation model is modified to be forced by a time series of realistic Rossby wave source (RWS) diagnosed from the atmospheric reanalysis product ERA5. Comparing two different model configurations with either weak or strong linear friction, 41-year long model experiments for the flow at 200hPa and 300hPa are conducted. In the model, the climatological upper-tropospheric rotational flow is driven by specified RWS and simulated eddy fluxes that result from stirring. Specifically, the model is intended as a framework to analyse equivalent barotropic low-frequency variability, i.e. teleconnections.

However, the expectation to reproduce the upper-tropospheric rotational flow from ERA5 cannot be realised. It is found that the mean-flow westerly jets are too weak and the variance is too high. In terms of variability, the model performs very differently when viewed from a global or regional perspective: There is reasonable temporal coherence between model and reanalysis for area-averaged kinetic energies but the performance for a regional climate index is low. The strong variance in the model can be attributed to barotropic instability. By averaging across an ensemble of model realisations initialised from ten different initial conditions, this internal variability can be removed. The low-frequency flow field, however, remains deteriorated compared to reanalysis. It is hypothesised that the model error arises from the lack of a "baroclinic governor" which bears analogy to the barotropic governor where baroclinic instability is suppressed in the presence of a small barotropic shear. This hypothesis is analysed in terms of normal mode solutions to a simple two-layer quasi-geostrophic model, though not conclusively.

Furthermore, it is found that the traditional RWS is incomplete. Permitting horizontal divergence but neglecting vertical advection does not allow the horizontal momentum equations to be written in flux form due to an inconsistency with the continuity equation. A more complete RWS needs to include the curl of vertical momentum advection: the sum of vortex tilting ($-\omega_x v_p + \omega_y u_p$) and vertical vorticity advection ($-\omega\zeta_p$). These new terms are particularly important for equatorial dynamics at 200hPa and for the subtropics at 300hPa.

Zusammenfassung

Diese Abschlussarbeit behandelt ein vollständig nichtlineares, barotropes Modell für ein divergenzfreies Geschwindigkeitsfeld mit zeitlich variablen, realistischen Randbedigungen für die obere Troposphäre. Die entsprechende Zeitreihe der *Rossby wave source* (RWS, z.Dt. Rossbywellenquelle) wird aus den Daten der Atmosphärenreanalyse ERA5 diagnostiziert. In einem Vergleich zweier Modellkonfigurationen mit unterschiedlichen Reibungskoeffizienten werden Modellexperimente mit einer Länge von jeweils 41 Jahren für die Zirkulation in einer Höhe von 200hPa und 300hPa untersucht. Der klimatologische Mittelwert in dem Modell entsteht durch die mittlere RWS und eine Kovarianz der Abweichungen der simulierten Geschwindigkeiten. Ziel ist die Analyse niedrigfrequenter, barotroper Variabilität – den atmosphärischen Telekonnektionen.

Entgegen den Erwartungen ist es jedoch nicht möglich, das divergenzfreie Geschwindikeitsfeld aus ERA5 zu reproduzieren. Die mittleren Westwinde sind zu schwach, wohingegen

die Varianz zu groß ist. Insbesondere besteht eine Diskrepanz zwischen der global gemittelten und der regionalen Leistungsfähigkeit des Modells: Aus globaler Sicht besteht eine gewisse Kohärenz zwischen der durch das Modell simulierten und der aus ERA5 diagnostizierten kinetischen Energie. Der zeitliche Verlauf eines regionalen Klimaindexes ist hingegen schlecht simuliert. Die große Varianz im Model lässt sich auf barotrope Instabilität zurückführen. Diese lässt sich durch den Mittelwert über ein Ensemble mit zehn unterschiedlichen Anfangsbedingungen herausfiltern. Allerdings wird so keine verbesserte Repräsentation der niedrigfrequenten Zirkulation erzielt. Es wird die Hypthese aufgestellt, dass der Modellfehler durch das Fehlen des *baroclinic governors* ensteht. Der analoge *barotropic governor* bewirkt, dass eine kleine horizontale Geschwindigkeitsscherung barokline Instabilität reduziert. Diese Hypthese wird mittels eines quasigestrophischen Zweischichtmodells untersucht.

Darüber hinaus wird festgestellt, dass die übliche Formulierung der RWS unvollständig ist. Das Vernachlässigen vertikaler Advektion bei gleichzeitiger horizontaler Divergenz widerspricht der Massenerhaltung. Eine vollständige RWS muss die Rotation vertikaler Impulsadvektion berücksichtigen. Diese entspricht der Summe aus *vortex tilting* (z.Dt. Wirbelneigen, $-\omega_x v_p + \omega_y u_p$) und der vertikalen Advektion horizontaler Wirbelstärke ($-\omega\zeta_p$). Diese Terme sind besonders relevant für die äquatorial Dynamik auf 200hPa und für die Subtropen auf 300hPa Höhe.

Plain language summary

The large-scale flow in the atmosphere is horizontal to first approximation. A two-dimensional numerical simulation is, thus, a useful tool to analyse atmospheric variability. More specifically, this thesis attempts to simulate the large-scale flow in the upper troposphere. That is the layer at the top of the convection layer that causes precipitation and lies just beneath the ozone layer. Upper-tropospheric dynamics control extratropical variability on time-scales that are longer than a couple of days.

It turns out that the effect of three-dimensional processes on the large-scale horizontal flow is stronger than expected. For example, high-frequency fluctuations are much more extreme than in reality. Apparently, three-dimensional processes have a mitigating effect on these fluctuations that is not captured by a two-dimensional simulation. Consequently, the strength of the mean-state mid-latitude westerly winds is poorly simulated. In contrast to weak mid-latitude westerlies, the simulations produce strong equatorial easterlies where wind velocities are low in reality. That is due to an incompleteness of the equations that these simulations are based on. This thesis introduces a more complete set of equations that accounts for the effect of vortex tilting in addition to vortex stretching. These findings about idealised two-dimensional simulations are of more than purely academic interest. They can contribute to the understanding of problems in sophisticated climate and weather prediction models and improve statistical analyses of atmospheric variability.

Contents

1. Introduction

Low-frequency atmospheric variability is dominated by so-called teleconnection patterns, mid- and upper-tropospheric variables that vary coherently. Among these are the North Atlantic Oscillation (NAO) and the Pacific-North American pattern (PNA) (Wallace and Gutzler, 1981; Barnston and Livezey, 1987). They are marked by a seesaw in midlatitude geopotential height fields connecting two or more centres of action on a variety of time scales. Atmospheric covariance is not confined to midlatitudes but also connects the tropics and the extratropics (Horel and Wallace, 1981). The positive phase of the El Niño Southern Oscillation (ENSO), for example, with disturbed trade winds over the tropical Pacific goes along with negative pressure anomalies over the North Pacific. Understanding these processes is most relevant for current advances in long-range weather forecasting (e.g. Smith et al., 2012).

In linear theory, teleconnections can be explained by the idea of Rossby wave propagation (Horel and Wallace, 1981). Rossby wave trains can be excited by diabatic heating or orography that cause vertical movement and, ultimately, horizontal divergence. Scaife et al. (2017) find that the tropical Rossby wave source (RWS) maximises as the level of the convective outflow (200hPa) provided that there is strong absolute vorticity. That designates the equatorward flank of subtropical jets as an important source region for Rossby wave trains. These waves can propagate around the globe since the westerly jets act as waveguides (Hoskins and Ambrizzi, 1993). Hoskins and Karoly (1981) show in a simple baroclinic model that barotropic Rossby waves dominate the steady linear response to a low-latitude RWS. Webster (1981) finds that the remote atmospheric response to a sea surface temperature anomaly and the associated diabatic heating of the atmosphere has a barotropic nature poleward to the westerly jet maximum. Based on the theory of barotropic Rossby wave trains, this thesis aims to evaluate the barotropic vorticity equation (BVE) as a simple framework to model the upper-tropospheric flow. This and its suitability for the analysis of teleconnections will be elucidated in more detail below.

1.1. Barotropic vorticity equation

Every smooth two-dimensional vector field $\vec{u}$ on a sphere can be decomposed into components without divergence or rotation respectively, i.e.

$$\vec{u} = \vec{u}_\psi + \vec{u}_\chi = -\nabla \times (\vec{e}_z \psi) + \nabla \chi \tag{1.1a}$$

$$\nabla^2 \psi = \vec{e}_z \cdot (\nabla \times \vec{u}) = \zeta \tag{1.1b}$$

$$\nabla^2 \chi = \nabla \cdot \vec{u} \tag{1.1c}$$

This is called a Helmholtz decomposition (e.g. Lindborg, 2015) where $\vec{u}_\psi$ is the nondivergent and $\vec{u}_\chi$ the irrotational flow, $\vec{e}_z$ points in the direction of the local vertical, and ζ is called

relative vorticity. In this study the terms rotational and divergent flow will be used synonymously for nondivergent and irrotational flow. The decomposition is achieved by defining scalar fields ψ and χ which are called stream function and velocity potential, respectively. The Laplacians of these scalar fields are the vector field's vorticity and divergence that can be easily calculated. Thus, inverting the Laplacian operator on a sphere is the key to the Helmholtz decomposition. It can be made use of the Helmholtz decomposition in order to discuss the large-scale atmospheric flow. Shown by simple scale analysis, the large-scale flow is close to being geostrophically balanced, i.e. its horizontal divergence is close to zero in midlatitudes (e.g. Rossby, 1939). Hence, the rotational flow can be considered as being synonymous with the large-scale flow on a rotating Earth.

The horizontal momentum equations for the atmospheric flow can be converted into two equations for vorticity and divergence. With the simple diagnostic equation (1.1b), the vorticity equation becomes a prognostic equation for the rotational flow. The BVE is derived from the assumption of a completely two-dimensional flow without any vertical dependence. It is obtained by taking the curl of the horizontal momentum equations ($\frac{\partial}{\partial x}(b) - \frac{\partial}{\partial y}(a)$), that are in pressure coordinates:

$$u_t + uu_x + vu_y - fv = -\Phi_x \tag{1.2a}$$

$$v_t + uv_x + vv_y + fu = -\Phi_y \tag{1.2b}$$

and, consequently,

$$\zeta_t + \vec{u} \cdot \nabla(\zeta + f) = -\nabla \cdot \vec{u}(\zeta + f) \tag{1.3}$$

Note that, throughout this study, subscript x, y, p, and t denote partial derivatives with respect to these coordinates. The material derivative on the left-hand side of (1.3) includes the advection of absolute vorticity and is balanced by vortex stretching on the right-hand side of (1.3). In a vorticity equation model, the horizontal velocities used for the advection term are deduced from relative vorticity by inverting the Laplacian. Therefore, the formulation of the differential equation with the correct inhomogeneity requires a separation between the rotational and divergent flow $\vec{u}_\psi$ and $\vec{u}_\chi$ (Sardeshmukh and Hoskins, 1988):

$$\zeta_t + \vec{u_\psi} \cdot \nabla(\zeta + f) = RWS \tag{1.4a}$$

$$RWS = -(\nabla \cdot \vec{u_\chi})(\zeta + f) - \vec{u_\chi} \cdot \nabla(\zeta + f) \tag{1.4b}$$

Sardeshmukh and Hoskins (1988) expression for the Rossby wave source includes horizontal advection of absolute vorticity by the divergent flow in addition to vortex stretching. Equation (1.4) corresponds to the conservation of absolute vorticity in the absence of any divergence. In other words, the rotational flow is driven by divergence. The solution of the fully non-linear homogeneous BVE includes two kinds of motion: Rossby waves and geostrophic turbulence. This is similar to the quasi-geostrophic framework of potential vorticity conservation. The analysis of the quasi-geostrophic framework revealed a wave-turbulence cross-over at the Rhines scale $L \approx \sqrt{U/\beta}$ (Rhines, 1975) with waves acting on larger scales than turbulence. In the following, these solutions to the homogeneous BVE will be introduced in more detail. The model results presented in chapter (3) are solutions to the inhomogeneous BVE and can be expected to include Rossby waves and geostrophic turbulence.

Rossby waves The Rossby waves supported by the BVE are linear solutions to the conservation of absolute vorticity (Vallis, 2017, Ch. 6.4.). Their propagation properties can be inferred from the dispersion relation. That is derived by linearising equation (1.4) around a zonal-mean flow indicated by an overbar, i.e. $\zeta = \bar{\zeta}(y) + \zeta'(x, y, t)$. Note that $\bar{v} = 0$, $(\bar{\zeta} + f)_x = 0$, and $\bar{\zeta} = -\bar{u}_y$, and that subscripts x, y, and t denote partial derivatives with respect to x, y, and t. Thus, the linearised homogeneous BVE for perturbations is

$$\zeta'_t + \bar{u}\zeta'_x + v'(\bar{u}_{yy} + \beta) = 0 \tag{1.5}$$

To find plane wave solutions $\psi' = \Re[\tilde{\psi} e^{i(kx+ly-\omega t)}]$ this equation has to be expressed in terms of stream function with $\zeta' = \nabla^2 \psi'$

$$(\nabla^2 \psi')_t + \bar{u}(\nabla^2 \psi')_x + \psi'_x(\beta - \bar{u}_{yy}) = 0 \tag{1.6}$$

Inserting the plane wave ansatz into (1.6) and neglecting spatial variations of wavenumber, one obtains a dispersion relation

$$\omega = \bar{u}k - \frac{(\beta - \bar{u}_{yy})k}{k^2 + l^2} \tag{1.7}$$

and horizontal group velocities

$$c_g^x = \frac{\partial \omega}{\partial k} = \bar{u} + \frac{(k^2 - l^2)(\beta - \bar{u}_{yy})}{(k^2 + l^2)^2} \tag{1.8a}$$

$$c_g^y = \frac{\partial \omega}{\partial l} = \frac{2kl(\beta - \bar{u}_{yy})}{(k^2 + l^2)^2} \tag{1.8b}$$

Note that in contrast to a quasi-geostrophic model, equation (1.5) does not feature vortex stretching as a restoring force to wave motion. The denominator in the dispersion relation (1.7) does, in consequence, not include an expression c/f that is called the radius of deformation where c is gravity wave speed and f is the Coriolis parameter. In other words, the barotropic model involves only waves with wavelengths that are small compared to the radius of deformation. On the other hand, it allows the Coriolis parameter to vary over the full range on the surface of a sphere and is not restricted to a β-plane.

These abstract considerations are useful in teleconnection studies for the application of WKBJ Rossby wave ray tracing (e.g. Hoskins and Karoly, 1981; Hoskins and Ambrizzi, 1993; Scaife et al., 2017). WKBJ theory treats slowly varying media where waves behave locally as a plane wave and the wave path can be inferred directly from its group velocities ($x/y = c_g^x/c_g^y$) (Vallis, 2017, Ch. 6.A.). An example of ray tracing for stationary Rossby waves ($\omega = c = 0$) from Hoskins and Karoly (1981) is shown in figure (1.1). A tropical RWS located at 15° N in the zonally averaged 300mb climatological flow excites wave trains with different zonal wavenumbers. In this setup, frequency and zonal wavenumber remain constant whereas the meridional wavenumber varies along the wave path. It is visible how low zonal wavenumbers radiate polewards, whereas high wavenumbers are trapped equatorward of the northern flank of the jet as the meridional vorticity gradient diminishes.

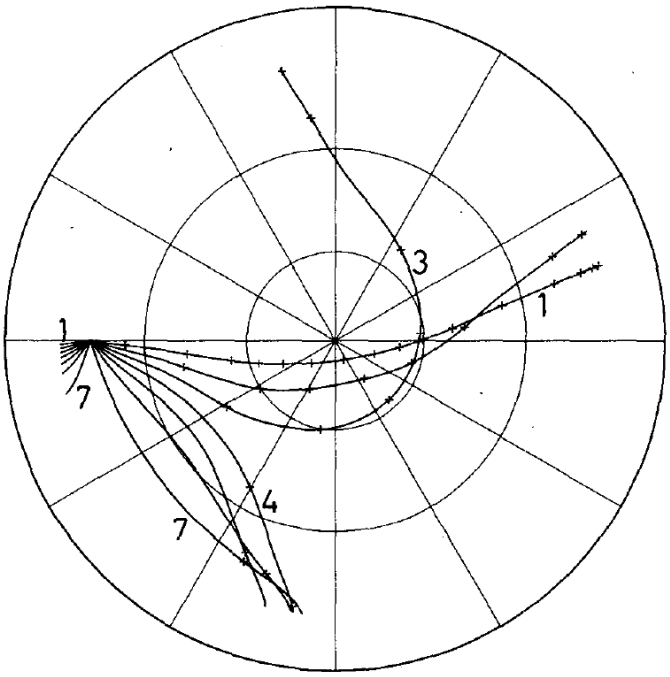

Figure 1.1.: *Stationary Rossby wave rays for a RWS at 15°N in the zonally averaged 300mb climatological flow for zonal wavenumbers 1-7, adapted from Hoskins and Karoly (1981).*

Qualitative insight into the horizontal propagation properties of Rossby waves and better understanding of figure (1.1) can be gained by discussing the limits of linear Rossby wave theory. The dispersion relation (1.7) can be transformed into an equation for the meridional wavenumber l with the zonal phase speed $c = \omega/k$:

$$l^2(y) = \frac{\beta - \bar{u}_{yy}}{\bar{u} - c} - k^2 \tag{1.9}$$

Linear theory fails when $l^2 < 0$ or $\bar{u} = c$ (Vallis, 2017, Ch. 16.2.). The first limit can be reached when either the meridional gradient of zonal-mean absolute vorticity ($\beta - \bar{u}_{yy}$) reduces or $\bar{u}$ increases to such an extent that $l \to 0$ and $c_g^y \to 0$. That produces a turning latitude depending on wavenumber. In the second case, $l \to \infty$ at a critical latitude where $\bar{u} = c$. That imposes a lower limit on $\bar{u}$ and, usually, one considers stationary waves with $c = 0$. In other words, Rossby waves can only exist in a positive meridional absolute vorticity gradient where the wind is westerly. Depending on wavenumber there is an upper and lower boundary for the strength of these westerlies.

It is important to note that westerly jets form a local maximum of the absolute vorticity gradient. They are bounded by two turning latitudes and, thus, represent a waveguide. This is summarised schematically in figure (1.2). Rossby waves excited in the tropics and subtropics propagate poleward until they reach their turning latitude. Their climate signal can be transmitted around the globe following waveguides. No Rossby waves can exist in the tropical easterlies.

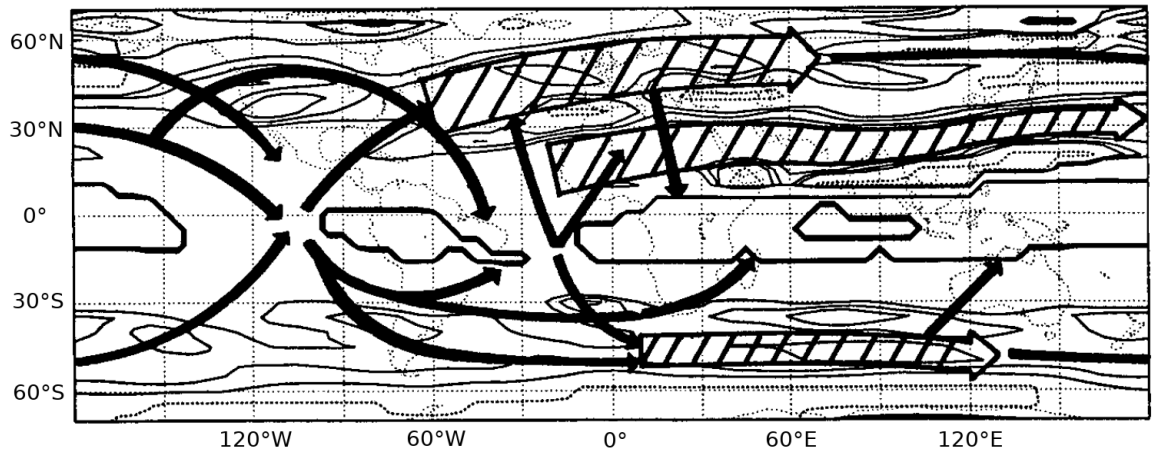

Figure 1.2.: *Schematic summary of waveguides (cross-hatched shafted arrows) with preferred Rossby wave rays (single shafted arrows), adapted from Hoskins and Ambrizzi (1993).*

Geostrophic turbulence Motions where non-linear terms dominate are called turbulence (Vallis, 2017, Ch. 11 & 12). On very small scales, turbulence is usually three dimensional and isotropic. In the atmosphere, however, the non-linear terms in the momentum equations and the effect of rotation create jointly large scale, two-dimensional turbulence (Charney, 1971). This is referred to as geostrophic turbulence. Many findings for geostrophic turbulence are based on quasi-geostrophic considerations (Rhines, 1979). The essential features, however, are also present in a barotropic model since the two frameworks share important conservation properties.

Many important characteristics of turbulence can be illustrated by the product of two sinusoids

$$\sin x \sin y = \tfrac{1}{2}(\cos(x-y) - \cos(x+y)) \tag{1.10}$$

It is evident that the products in the advection term in the governing equations cause interactions of different waves to create waves with the sum or difference of the individual wavenumbers (*triad interaction*). That introduces a so-called closure problem. The inevitable truncation of large wavenumbers in a numerical model neglects the effect of sub-grid-scale motion onto larger scales. Furthermore, these triad interactions cause the chaotic nature of turbulent motions as small disturbances can grow substantially (Lorenz, 1963). This is the so-called sensitive dependence on initial conditions.

An important constraint in isotropic turbulence is the conservation of globally integrated kinetic energy. In two-dimensional turbulence, the conservation of enstrophy q^2 (squared absolute vorticity) provides an additional constraint (Vallis, 2017, Ch. 11.3). Due to the chain rule of differentiation the material derivative of enstrophy is connected to the conservation of absolute vorticity by a simple multiplication $Dq^2/Dt = 2q \cdot Dq/Dt = 0$. It follows from Gauss' theorem that enstrophy is conserved not only following the flow but also in a global integral:

$$\begin{aligned} \frac{d}{dt}\int_A q^2 dA = \int_A 2q\frac{dq}{dt}dA = -2\int_A q(\vec{u_\psi}\cdot\nabla)qdA \\ = -\int_A \vec{u_\psi}\cdot\nabla q^2 dA = -\int_A \nabla\cdot(\vec{u_\psi}q^2)dA = 0 \end{aligned} \tag{1.11}$$

It is hard to say anything analytically about turbulence, but Kolmogorov (1941) formulated a theory on the energy spectrum of three-dimensional turbulence based on the spectral energy flux. The basic assumption is that the scale of energy supply and that of energy dissipation are well separated by an inertial range. In the inertial range, energy is cascaded to smaller scales and the spectrum falls off proportional to $k^{-5/3}$ (where k is wavenumber). By similar reasoning to Kolmogorov's theory, Kraichnan (1967) introduced two inertial ranges for two-dimensional turbulence: one on either side of the scale of energy supply k_i. In these inertial ranges, enstrophy is cascaded to smaller scales and energy is transferred to larger scales by an inverse cascade. The energy spectrum is predicted to be proportional to $k^{-5/3}$ in the energy inertial range ($k < k_i$) and proportional to k^{-3} where enstrophy is cascaded to smaller scale ($k > k_i$). The spectrum of enstrophy is connected to the spectrum of energy by a factor of k^2. The finding of an inverse energy cascade in two-dimensional turbulence is important for the atmospheric flow since it offers the possibility to drive a large scale flow by small scale structures.

In this regard, barotropic vorticity equation models have been used extensively to model two dimensional turbulence (Lilly, 1969; Maltrud and Vallis, 1991). The success of these simulations in reproducing the $k^{-5/3}$ and k^{-3} inertial ranges does depend on resolution amongst other things. The drawbacks of limited resolution can partially be compensated by using backscatter parameterisations to account for sub-grid-scale processes (e.g. Thuburn et al., 2014; Jansen et al., 2015).

1.2. Upper-tropospheric circulation

By means of a BVE model and with the aim to analyse teleconnections, this thesis attempts to simulate the large-scale upper-tropospheric circulation. The understanding of this flow can be based on the radiative imbalance between the tropics and the extratropics (Holton and Hakim, 2013, Ch. 10). The resulting temperature difference introduces a latitudinal dependence of the vertical pressure gradient, and consequently a meridional pressure gradient at height. The compensating flow forms a thermally direct Hadley cell with equatorward motion at the surface and poleward motion in the upper troposphere. Next to the radiative energy budget, the Earth's rotation has a major influence on the atmospheric circulation. Because of that, the upper-tropospheric flow is deflected eastward on its way poleward conserving its angular momentum. The resulting subtropical westerly jet forms the poleward edge of the Hadley cell (Holton and Hakim, 2013, Ch. 10). In particular, the conservation of angular momentum induces a relationship between the strength of the subtropical jet and the width of the Hadley cell. Together, these are determined thermodynamically and radiatively by the meridional temperature gradient that balances the vertical shear introduced by the jet (Vallis, 2017). Poleward to the Hadley cells, thermally indirect Ferrell cells with

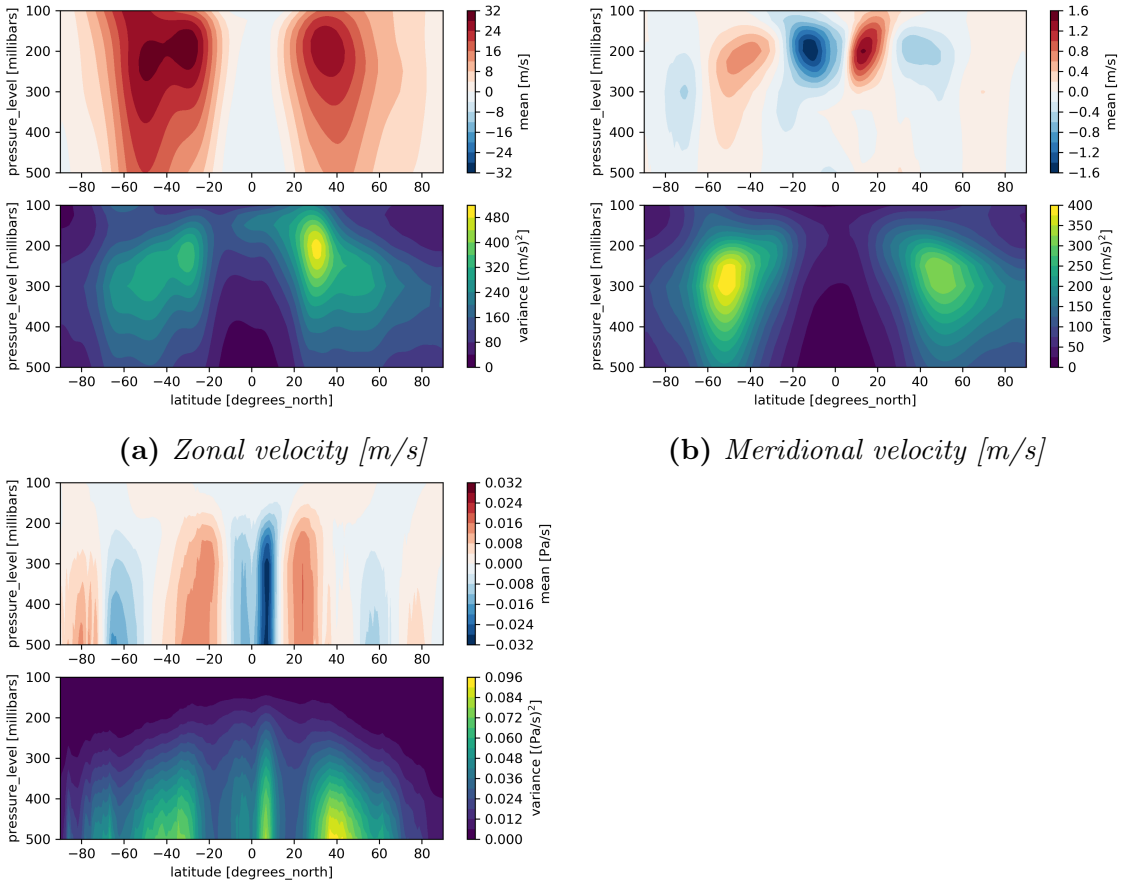

(a) *Zonal velocity [m/s]*

(b) *Meridional velocity [m/s]*

(c) *Vertical velocity [Pa/s]*

Figure 1.3.: *Eulerian zonal-mean annual mean of middle- and upper-tropospheric velocities from ERA5 and mean squared anomalies from that mean. Note that (c) shows* $\omega = \frac{Dp}{Dt}$ *which is negative for ascent.*

an eddy-driven, rather barotropic jet can be found (Holton and Hakim, 2013, Ch. 10). In reality, the subtropical and the eddy-driven jets are not easily distinguished.

Reanalysis data (see Ch. 2.3 for details) of horizontal and vertical velocities illustrate the description above. The time-mean, zonal-mean zonal wind (Fig. 1.3a) shows strong westerlies covering the displayed vertical range from the middle troposphere into the stratosphere. They are stronger in the southern hemisphere maximising around 30 m/s. In the southern hemisphere, the eddy-driven and the subtropical jet are distinguishable, not so well in the northern hemisphere. At the equator, there are very weak mean easterlies of less than 4 m/s. The mean squared anomalies mirror the time-mean zonal mean, but they are stronger in the northern hemisphere. There is a non-negligible variance also at the equator close to the tropopause. In contrast to the zonal wind, the mean meridional velocities (Fig. 1.3b) are restricted to the upper troposphere and are about one order of magnitude smaller. They are dominated by the convective outflow between 20° N/S. Poleward to that at the top of the Ferrell cell, much weaker winds blow in the opposite direction. The variance of the

meridional velocity is comparable to that of the zonal velocity, although shifted towards the poles. It is the image of the eddy-driven jet. Vertical motion (Fig. 1.3c) is restricted to the troposphere. There is time-mean, zonal-mean rising motion at the equator. Poleward of the descending branch of the Hadley cell, one can see rising air in the extratropical low pressure systems and descending air over the poles.

For the sake of this thesis, the author wants to draw attention to two characteristics of the atmospheric circulation: The equivalent barotropic nature of the extratropics and the momentum flux balance of the equatorial circulation.

Equator Upper-tropospheric zonal velocities have a local minimum at the equator. That is important for teleconnection studies since, consequently, absolute vorticity is zero at the equator. So there is no significant RWS at the equator. The close-to-zero mean zonal wind results from a balance of counteracting momentum fluxes.

In a nondivergent flow, the advective terms in the momentum equations can be rewritten into momentum flux convergences. Analysing 200hPa reanalysis data, Lee (1999) splits the time-mean, zonal-mean horizontal momentum flux convergence into contributions by transient eddies, stationary eddies, transient zonal-mean circulation, and time-mean zonal-mean circulation:

$$-\overline{[uv]}_y = -\overline{[u*'\, v*']}_y - [\bar{u}*\bar{v}*]_y - \overline{([u]'[v]')}_y - ([\bar{u}][\bar{v}])_y \tag{1.12}$$

The asterisks and primes in this equation denote perturbations from the time and zonal mean that are, in turn, represented by an overbar and [ ], respectively. Lee (1999) finds that the transient zonal-mean circulation drives equatorial easterlies whereas transient eddies, stationary eddies, and the time-mean zonal-mean circulation cause westerly acceleration. Space-time cross-spectral analysis of the transient eddies reveals peaks of equatorward momentum flux on interannual timescale and by the Madden-Julian Oscillation (MJO). More specifically, Lee (1999) finds an opposing effect between the easterly acceleration due to the seasonal cycle and the westerly acceleration caused by a convergence of equatorward eddy flux associated with the MJO. This view is confirmed for example by Dima et al. (2005) and Gollan and Greatbatch (2015). In a BVE model, the eddy momentum flux by rotational velocities is simulated but the rest has to be specified as a forcing.

Extratropics In contrast to the subtropical jet forming the poleward edge of the Hadley cell, the eddy-driven has a barotropic structure. These westerlies, thus, have to be maintained against surface friction by an eddy momentum flux convergence (Vallis, 2017, Ch. 15). The most relevant mechanism driving that momentum flux convergence is the barotropic decay of baroclinic waves. In a baroclinic atmosphere, the available potential energy is converted to eddy kinetic energy by baroclinic instability (e.g. Simmons and Hoskins, 1978). Simmons and Hoskins (1978) demonstrate how baroclinic growth is followed by a barotropic decay turning eddy kinetic energy into mean flow kinetic energy. The momentum flux convergence associated with this process can be understood in terms of Rossby wave radiation (Vallis, 2017, Ch. 15). More specifically, the barotropic Rossby waves created by baroclinic instability flux westerly momentum into their source region due to their phase relation-

ship (boomerang-shaped eddies) when propagating away and dissipating at distance. Vallis et al. (2004) illustrate this by a discussion of the pseudomomentum budget for flow subject to stirring. In reality, however, this simple argument is complicated by an interaction of midlatitude waves with the subtropical and tropical circulation.

This mechanism to create the barotropic jet is driven by high-frequency synoptic variability as demonstrated by Vallis et al. (2004) in a modelling study. Baroclinic instability specified as RWS is integrated to a barotropic response with power on longer time scales than the decorrelation time scale of the RWS. For this reason, the extratropical variability in a baroclinic atmosphere turns out to be essentially barotropic when daily fluctuations are removed by a low pass filter (Baxter and Nigam, 2013). In particular, this point argues in favour of a barotropic model to analyse low-frequency atmospheric variability. It can be expected to capture the dynamics of the eddy-driven jet, only the stirring by the baroclinic flow has to be specified as a forcing.

1.3. Outline

The characteristics of the upper-tropospheric large-scale flow introduced in the sections above - the zonal-mean subtropical and eddy-driven jet, and the teleconnection patterns produced by Rossby wave trains - are expected to be well simulated by the rotational flow in a BVE model. RWS forcing, representing baroclinic instability and the feedback of the divergent on the rotational flow in general, is meant to drive the basic state of the large scale flow by an inverse energy cascade. To the limit of the chaotic nature of a turbulent flow, the model is expected to reproduce the rotational flow of the dataset from which the RWS is diagnosed.

This hypothesis will be tested by driving the BVE model with a long time series of realistic RWS. This is, in particular, not a steady-state response experiment to a certain anomalous forcing. Both the mean state and the variability in the model will be compared to the reference dataset, the reanalysis product *ERA5* in this case. To the author's knowledge, there is no other study that follows this approach. The advantage of a simplified model like this is the attributability of results which is important for non-linear experiments. A future study could feature experiments with filtered or regionalised forcing.

One alternative approach, that is often used to drive a BVE model, is to maintain the basic state of the flow artificially by an initial time step correction $\overline{F}$ and apply RWS anomalies F' only (e.g. Simmons, 1982; Hoskins and Ambrizzi, 1993; O'Reilly et al., 2018; Baker et al., 2019).

$$F = \overline{F} + F' \tag{1.13}$$

In order to do so, $\overline{F}$ is determined so that the initial basic state is an exact solution of the model. It depends on both the specified initial flow and the model's internal properties. This approach represents a linearisation of the model around the basic state. It allows the investigation of perturbations to that basic state caused by the anomalous forcing. This is reasonable for stationary response experiments where the signal is the difference between the final state and the basic state. In contrast to that approach, the model used for this

thesis needs to generate the climatological basic state internally, which turns out to be more difficult than expected. However, the linearisation implied by an initial time step correction can pose a restriction to the variability in the model and, therefore, is not suitable when analysing atmospheric variability.

Another approach, that was used to look at variability, is to apply random stirring representing the effect of baroclinic instability on the barotropic flow (e.g. Maltrud and Vallis, 1991; Vallis et al., 2004; Barnes et al., 2010). Although this approach captures many essential features, it represents an idealisation of the jet and does not allow a direct comparison with realistic time series. More specifically, random stirring does not produce features of the atmospheric flow, that are created by a time-mean forcing, like the subtropical jet.

This thesis is continued by a detailed description of the numerical model in chapter (2). It is based on an idealised spectral model released by the Geophysical Fluid Dynamics Laboratory (GFDL). Special focus will be on the implementation of the time series forcing from reanalysis and the respective modifications to the algorithm. After characterising the RWS forcing in chapter (3.1), the model output is analysed in chapter (3.2). More specifically, the mean state of the model, domain-averaged kinetic energies, and a regional climate index will be compared to the rotational, upper-tropospheric flow from reanalysis. In comparison to reanalysis, the mean state in the model is deteriorated by intense barotropic instability. This finding is discussed by evaluating the influence of baroclinic shear on normal mode growth due to barotropic instability in a simple quasi-geostrophic model (see Ch. 4). It is referred to as the baroclinic governor in analogy with the better known barotropic governor (James, 1987; Mak, 2011). The analysis of the barotropic model also reveals strong equatorial easterlies where in reality wind velocities are weak. This can at least partially be attributed to deficiencies in the forcing. A more complete RWS for the upper-tropospheric flow that includes the effect of vertical momentum advection is, therefore, presented in chapter (5). Finally, the conclusion (Ch. 6) will discuss where the expectations in the model have been failed and what lessons can be learned. The findings in this study might, in fact, be relevant for problems seen in sophisticated atmospheric general circulation models as well. The conclusion is rounded off with a short outline for proceeding studies.

2. Model description

The model used in this study is based upon the barotropic version of the Idealized Global Atmospheric Models with Spectral Dynamics published by the Geophysical Fluid Dynamics Laboratory (GFDL)*. The public release has been used to analyse the nonlinear barotropic decay of certain initial conditions (Held and Phillips, 1987) or to integrate the barotropic vorticity equation (BVE) with random stirring (Vallis et al., 2004). For this study, the GFDL barotropic model is modified to be driven by a time series of realistic forcing. The necessary modifications to the algorithm are discussed in section (2.2). The specific equation integrated by the numerical model is

$$\frac{\partial \zeta}{\partial t} + \nabla \cdot (\vec{u}_\psi(\zeta + f)) = -r\zeta - \kappa\nabla^4\zeta + S \tag{2.1}$$

where ζ is relative vorticity, $\vec{u}_\psi$ is the rotational flow, f is the Coriolis parameter, and S is the forcing. In such a simplified model, dissipation processes need to be parameterised. These processes act to remove energy at large scales and enstrophy at small scales (Maltrud and Vallis, 1991). Several different damping schemes exist in literature (Hoskins and Karoly, 1981; Held and Phillips, 1987; Sardeshmukh and Hoskins, 1988; Hoskins and Ambrizzi, 1993; Vallis et al., 2004) that use linear friction and biharmonic diffusion to implement this behaviour. In equation (2.1), these are represented by the linear friction time scale r^{-1} and viscosity κ. The model is a spectral model using spherical harmonics. A detailed elaboration on the properties of spherical harmonics is given in section (2.1). The model algorithm is explained in section (2.2) and the forcing in section (2.3) and (2.4). The choice of model parameters like damping coefficients and spectral resolution is presented in section (2.5).

2.1. Spectral model

In order to integrate eq. (2.1) numerically, one could discretise the spatial derivatives using the grid point method. Alternatively, one can use a spectral model with spherical harmonics where spatial derivatives can be solved analytically. The latter is advantageous for two reasons (Durran, 2010, Ch. 6.4): First, it solves the pole problem. In a rectangular latitude-longitude grid on a sphere, poles pose a singularity that has to be taken care of when defining derivatives. When using spherical harmonics these are defined to be zero. Second, it suits the inversion of the Laplacian operator, which has to be performed at every time step to deduce the horizontal velocities from vorticity in order to capture the nonlinear terms.

In the following, it is demonstrated that spherical harmonics are eigenvectors of the Laplacian operator. For calculations on a sphere, it is convenient to use spherical coordinates

*retrieved from: `https://www.gfdl.noaa.gov/idealized-spectral-models-quickstart/`, March 2019

(λ, θ, a). The transformation into right-handed Cartesian coordinates with the origin at the center of the Earth and the z-dimension parallel to the Earth's rotation axis is given by

$$\vec{r} = \begin{pmatrix} a\cos\theta\cos\lambda \\ a\cos\theta\sin\lambda \\ a\sin\theta \end{pmatrix} \tag{2.2}$$

where a is the radius of the sphere, θ the latitude and λ the longitude on that sphere. Please note that on the surface of a sphere, a is constant. The aim is to express the Laplacian operator, given by $\nabla^2 = (\nabla \cdot \nabla)$, in spherical coordinates. So, we are interested in the horizontal gradient of a scalar field $A = A(\theta, \lambda)$ and the divergence of a two-dimensional vector field $\vec{v} = \vec{v}(\theta, \lambda)$. These are given in spherical coordinates as

$$\nabla A = \frac{1}{a}\frac{\partial A}{\partial \theta}\vec{e_\theta} + \frac{1}{a\cos\theta}\frac{\partial A}{\partial \lambda}\vec{e_\lambda} \tag{2.3a}$$

$$\nabla \cdot \vec{v} = \frac{1}{a\cos\theta}\frac{\partial}{\partial \theta}(\cos\theta v_\theta) + \frac{1}{a\cos\theta}\frac{\partial v_\lambda}{\partial \lambda} \tag{2.3b}$$

where $\vec{e_\lambda}$, $\vec{e_\theta}$ are orthogonal unit vectors pointing towards increasing λ, θ and v_λ, v_θ are the components of $\vec{v}$ for this basis. In particular, that means for vorticity ζ and stream function ψ

$$\zeta = \nabla^2\psi = \nabla \cdot (\nabla\psi) = \frac{1}{a^2}\left(\frac{1}{1-\mu^2}\frac{\partial^2\psi}{\partial\lambda^2} + \frac{\partial}{\partial\mu}(1-\mu^2)\frac{\partial\psi}{\partial\mu}\right) \tag{2.4}$$

with $\mu = \sin\theta$. In order to find the spherical harmonics, the eigenvalue problem associated with eq. (2.4) can be solved by a separation of variables for eigenvectors $\psi = P(\mu)L(\lambda)$ and eigenvalues ρ (Krishnamurti et al., 1998, Ch. 6):

$$\frac{1}{a^2}\left(\frac{1}{1-\mu^2}P(\mu)\frac{\partial^2 L}{\partial\lambda^2} + L(\lambda)\frac{\partial}{\partial\mu}(1-\mu^2)\frac{\partial P}{\partial\mu}\right) = \rho P(\mu)L(\lambda) \tag{2.5a}$$

$$\Rightarrow \frac{(1-\mu^2)}{P(\mu)}\frac{\partial}{\partial\mu}(1-\mu^2)\frac{\partial P}{\partial\mu} - \rho a^2(1-\mu^2) = -\frac{1}{L(\lambda)}\frac{\partial^2 L}{\partial\lambda^2} \tag{2.5b}$$

The right-hand side of (2.5b) can be solved by $L_m = e^{\pm im\lambda}$. That leaves the so-called associated Legendre equation for the left-hand side of (2.5b).

$$\frac{\partial}{\partial\mu}(1-\mu^2)\frac{\partial P}{\partial\mu} + \left(\rho a^2 - \frac{m^2}{1-\mu^2}\right)P = 0 \tag{2.6}$$

Eq. (2.6) is solved by the associated Legendre polynomials

$$P_l^m(\mu) = \frac{(1-\mu^2)^{m/2}}{2^l l!}\frac{d^{l+m}}{d\mu^{l+m}}(\mu^2-1)^l, \qquad |\mu| \leq 1 \tag{2.7}$$

Hence, the eigenvalues of the Laplacian are

$$\rho = \frac{-l(l+1)}{a^2} \tag{2.8}$$

The spherical harmonics $Y_{l,m} = P_l^m(\sin\theta)L_m(\lambda)$ are orthogonal and can be normalised

$$\frac{1}{2\pi}\int_{-\pi/2}^{\pi/2}\cos(\theta)d\theta\int_0^{2\pi}d\lambda Y_{l,m}(\theta,\lambda)Y^*_{l',m'}(\theta,\lambda) = \delta_{l,l'}\delta_{m,m'} \tag{2.9}$$

Stream function and vorticity can, therefore, be expressed as a series expansion of spherical harmonics:

$$\psi(\theta,\lambda) = \sum_{l=0}^{\infty}\sum_{m=-l}^{l}\psi_{l,m}Y_{l,m}(\theta,\lambda) = \sum_{l=0}^{\infty}\sum_{m=-l}^{l}\psi_{l,m}P_l^m(\sin\theta)e^{im\lambda} \tag{2.10a}$$

$$\zeta(\theta,\lambda) = \sum_{l=0}^{\infty}\sum_{m=-l}^{l}\zeta_{l,m}Y_{l,m}(\theta,\lambda) = \sum_{l=0}^{\infty}\sum_{m=-l}^{l}\zeta_{l,m}P_l^m(\sin\theta)e^{im\lambda} \tag{2.10b}$$

$$\zeta_{l,m} = \frac{-l(l+1)}{a^2}\psi_{l,m} \tag{2.10c}$$

The variables $\psi_{l,m}$ and $\zeta_{l,m}$ are the spectral coefficients of the series expansions of stream function and vorticity. These are connected in (2.10c) by the corresponding eigenvalue of the Laplacian. The inversion of the Laplacian operator is, thus, achieved by simple multiplication. As discussed in chapter (1.1), nondivergent horizontal velocities u_ψ, v_ψ can be inferred from stream function as a meridional and zonal derivative. It is convenient to define $U = u_\psi\cos\theta$ and $V = v_\psi\cos\theta$ with

$$U = -\frac{1}{a}\left((1-\mu^2)\frac{\partial\psi}{\partial\mu}\right) = \sum_{l=0}^{\infty}\sum_{m=-l}^{l}U_{l,m}Y_{l,m}(\theta,\lambda) \tag{2.11a}$$

$$V = \frac{1}{a}\left(\frac{\partial\psi}{\partial\lambda}\right) = \sum_{l=0}^{\infty}\sum_{m=-l}^{l}V_{l,m}Y_{l,m}(\theta,\lambda) \tag{2.11b}$$

$$U_{l,m} = \frac{1}{a}\left((l-1)\epsilon_{l,m}\psi_{l-1,m} - (l+2)\epsilon_{l+1,m}\psi_{l+1,m}\right) \tag{2.11c}$$

$$V_{l,m} = \frac{1}{a}\left(im\psi_{l,m}\right) \tag{2.11d}$$

$$\epsilon_{l,m} = \left(\frac{l^2-m^2}{4l^2-1}\right)^{1/2} \tag{2.11e}$$

The expression (2.11c) is obtained with the recurrence relation

$$(1-\mu^2)\frac{dY_{l,m}}{d\mu} = -l\epsilon_{l+1,m}Y_{l+1,m} + (l+1)\epsilon_{l,m}Y_{l-1,m} \tag{2.12}$$

This relation means that the meridional derivative of a spherical harmonic projects onto adjacent harmonics. Consequently, for the expression eq. (2.11c) one has to consider the harmonics $(l-1,m)$ and $(l+1,m)$ as their meridional derivative projects onto the harmonic (l,m). To make a note for the interpretation of spherical harmonics, m represents a zonal angular wavenumber on a unit sphere. Interestingly, the associated Legendre polynomials

have $l-m$ roots between the poles. So $l-m$ can be interpreted as a meridional wavenumber and l as a total horizontal wavenumber (Krishnamurti et al., 1998, Ch. 6)

Some of the advantages of a spectral model using spherical harmonics are discussed at the beginning of this section. In addtion to those, such a model solves the problem that regular latitude-longitude grids involve a very small zonal grid spacing close to the poles and, consequently, require a very small time step because of the Courant-Friedrichs-Lewy (CFL) condition (Durran, 2010, Ch. 6.4). Also, the use of spherical harmonics transforms the biharmonic diffusion used in equation (2.1) to simple linear friction with an individual friction time scale for each wavenumber. That allows a computationally efficient treatment of the right-hand side of eq. (2.1).

However, the product of nondivergent velocity and absolute vorticity for the vorticity flux in equation (2.1) is not easily transformed into spectral space. The most efficient approach is to apply the transform method (Durran, 2010, Ch. 6.4): The nonlinear product is calculated in grid space and then transformed to spectral space at each time step. The transformation between grid space and spectral space is done separately for the zonal and meridional dimensions. For the zonal dimension the fast Fourier transform (FFT) constitutes an efficient algorithm, and for the meridional dimension, Gaussian quadrature facilitates the transformation. Gaussian quadrature requires the model variables to be stored on a Gaussian grid, i.e. for latitudinal grid points θ_i, the sinuses, $\sin\theta_i$, have to be the roots of a Legendre polynomial. In order to avoid aliasing during the transformation of a series of spherical harmonics truncated triangularly at wave number M, one needs at least $(3M+1)/2$ meridional grid points and $3M+1$ zonal grid points (Durran, 2010, Ch. 6.4). The triangular truncation used in this study is discussed in section (2.5).

2.2. Model algorithm

Given these advantages of a spectral model when using the transform method, equation (2.1) is integrated using the following algorithm. At each time step the model

1. calculates the absolute vorticity flux in grid space,
2. calculates the convergence of that flux in spectral space,
3. sums the vorticity flux convergence, the relative vorticity multiplied by the damping coefficients, and the forcing in spectral space
4. performs the time stepping to compute future relative vorticity in spectral space,
5. inverts the Laplacian to deduce future stream function and nondivergent velocities and transforms them into grid space.

All linear calculations are done in spectral space. The product of absolute vorticity and horizontal velocities in step (1), however, needs to be computed in grid space as discussed above. The multiplication of relative vorticity in step (3) accounts for friction and biharmonic diffusion. Note again that using spherical harmonics biharmonic diffusion has the form of linear friction. Hence, the damping coefficients are the sums of the linear friction parameter and the squared eigenvalues of the Laplacian multiplied by the biharmonic viscosity. The time stepping in the step (4) follows a certain numerical scheme that involves

values of relative vorticity from different time steps, as discussed below.

The numerical scheme used in the public release of the GFDL barotropic model is a semi-implicit leapfrog scheme

$$\widetilde{\zeta}_{n+1} = \widetilde{\zeta}_{n-1} + 2\Delta t \cdot \mathrm{coeff}(\widetilde{\mathrm{adv}}_n + \widetilde{\mathrm{diss}}_{n-1}) \tag{2.13a}$$

$$\mathrm{coeff} = \frac{1}{1 + (r + \kappa\frac{(l(l+1))^2}{a^4})2\Delta t} \tag{2.13b}$$

$$\widetilde{\mathrm{adv}} = -\nabla \cdot \widetilde{\begin{pmatrix} u(\zeta+f) \\ v(\zeta+f) \end{pmatrix}} \tag{2.13c}$$

$$\widetilde{\mathrm{diss}} = -(r + \kappa\frac{(l(l+1))^2}{a^4})\widetilde{\zeta} \tag{2.13d}$$

followed by a Robert-Asselin filter.

$$\widetilde{\zeta_n} = (1-2\gamma)\widetilde{\zeta_n} + \gamma(\widetilde{\zeta_{n+1}} + \widetilde{\zeta_{n-1}}) \tag{2.14}$$

These equations are written in terms of spectral coefficients indicated by a tilde. Equations (2.13 b, c & d) express the implicity factor, the absolute vorticity flux convergence, and the sum of linear friction and biharmonic diffusion in spectral space, respectively. The parameters denote the time step Δt, the total wave number l, the Earth's radius a and the filtering coefficient γ.

The leapfrog scheme is a simple second-order accurate three-level scheme that is widely used to solve the advection equation (Messinger and Arakawa, 1976). However, it is unstable for the friction equation. Therefore, the damping terms are treated using the backward scheme. Being a three-level scheme, leapfrog requires a second initial condition that is acquired with one forward time step. The major disadvantage of leapfrog is the undamped computational mode that is unconnected to the physical mode (Messinger and Arakawa, 1976). The filter (2.14) is designed to damp the computational mode by connecting consecutive time steps with a small filtering coefficient (Robert, 1966; Asselin et al., 1972).

This time splitting problem is of particular relevance in this study. With the implementation of time-varying forcing the model became numerically unstable. The instability was mitigated by a high filtering coefficient. However, the numerical scheme thereby lost its second-order accuracy and long multi-year runs were still not possible. This problem is solved successfully by using the third-order Adams-Bashforth scheme as promoted by Durran (1991):

$$\widetilde{\zeta}_{n+1} = \widetilde{\zeta}_n + \frac{\Delta t}{12}\left(23h(\widetilde{\zeta}_n) - 16h(\widetilde{\zeta}_{n-1}) + 5h(\widetilde{\zeta}_{n-2})\right) \tag{2.15}$$

where $h(\widetilde{\zeta_n})$ is the sum of vorticity flux convergence, dissipation, and forcing at time step n. That scheme can be used for both the advection and the damping terms, and the computational mode is damped. So, there is no need for filtering. Compared to the second-order Adams-Bashforth scheme (Marshall et al., 1997), a much larger time step can be used. It is almost as time-efficient as the leapfrog scheme. The larger memory consumption of a four-level scheme does not pose a problem. The second and third initial condition for this four-level scheme are obtained by two forward time steps. The application of the third-order

Adams-Bashforth scheme is the first major modification made on the public release of the GFDL barotropic model.

The applicable time step length Δt depends on the size of the linear friction parameter. For a 12 days friction time scale at spectral resolution T85, Δt was set to 300s, and for a 6 days friction time scale it was set to 360s. The computations for this study were performed on the NEC HPC-Linux-cluster at the computing center at Kiel University[†]. Parallelised onto 16 cores, one model year with Δt=300s takes on average 1500s of computing time. At a spectral resolution T85 the third-order Adams-Bashforth scheme requires 1.2 GB memory for execution.

For a thorough numerical stability analysis, the model would have to be written as a matrix equation and the eigenvalues of that matrix would have to be compared with the stability region of the numerical scheme in use. Nonetheless, that proves complicated for a spherical model using the transform method. Instead, the model time step is compared to the stability criteria for purely real or imaginary eigenvalues ϵ and ω with third-order Adams-Bashforth. These are taken from Kantha and Clayson (2000) and Durran (1991):

$$\Delta t < 0.55/|\epsilon| \quad \text{, for negative real eigenvalues } \epsilon \tag{2.16a}$$

$$\Delta t < 0.72/|\omega| \quad \text{, for imaginary eigenvalues } \omega \tag{2.16b}$$

As already noted, in spectral coordinates biharmonic diffusion looks like the friction equation and the shortest damping time scale corresponds to a negative real eigenvalue of $\epsilon = -1/8640s$. That is well inside the stability area of third-order Adams-Bashforth. Horizontal advection with a phase speed c creates imaginary eigenvalues $\omega = ck_{max}$, with $k_{max} = 85/a \approx 1/75km$ in this case. Hence, the largest phase velocities that fulfil the stability criterion for $\Delta t = 300s$ and $\Delta t = 360s$ are $c_{max} \approx 180m/s$ and $c_{max} \approx 150m/s$ respectively. These are larger than the maximum horizontal velocity found in the model output. Still, it is evident that advection determines the applicable time step length Δt and that its dependence on the linear friction parameter arises from different maximum velocities.

The second modification to the algorithm is the interpolation of initial relative vorticity and forcing from NetCDF (Network Common Data Format) files to the model. That was achieved by adapting the `time_interp_external_mod` module from the complex AM3 GFDL atmospheric model to the idealised barotropic model. It offers functionality to read in and interpolate external fields linearly to a model grid and model time. Importantly, it supports distributed reads for parallel computations. The interpolation of the forcing takes place every time step. The computation of the forcing itself is done offline, so the spatial and temporal resolution is determined solely by the resolution of the original input data. However, an online calculation of RWS forcing was tested and did not improve the model performance.

[†]see `https://www.rz.uni-kiel.de/en/our-portfolio/hiperf/nec-linux-cluster?set_language=en`

2.3. Forcing from reanalysis & model output

This study intends to simulate the large scale upper-tropospheric flow using an idealised barotropic model. For that purpose, atmospheric reanalysis products provide a reference that can be regarded as a good representation of reality. Therefore, an atmospheric reanalysis dataset is assumed to be the appropriate basis from which to derive the model forcing. A fundamental hypothesis of this study, that is to be tested below, is that the barotropic model driven by RWS diagnosed from reanalysis should fully reproduce the nondivergent horizontal flow from reanalysis.

The European Center for Medium-Range Weather Forecasts provides a reanalysis dataset called *ERA5* which is based on 4D-Var data assimilation using a recent model cycle of the Integrated Forecasting System (IFS) (Hersbach et al., 2019). The IFS atmospheric model features a high horizontal resolution of 31km and 137 vertical levels up to 1hPa. In the following, by reanalysis it will always be referred to ERA5. For this study, 6-hourly horizontal and vertical velocity data was downloaded, covering the period 1979-2019 and interpolated to a $0.75^\circ \times 0.75^\circ$ latitude/longitude grid and pressure levels (100hPa, 125hPa, 150hPa, 175hPa, 200hPa, 225hPa, 250hPa, 300hPa, 350hPa, 400hPa, 450hPa, 500hPa). The analyses are predominantly performed with 200hPa and 300hPa data.

Both initial relative vorticity and forcing are taken from reanalysis. On that basis, long model runs with a length of 41 years and a single initialization in January 1979 were performed. The influence of initial conditions is lost rapidly but a certain coherence between model and reanalysis induced by the time series forcing can be expected. For the diagnosis of the 6-hourly forcing, reanalysis data was interpolated onto a T85 Gaussian de-aliasing grid that is exactly the model resolution. The Rossby wave source (RWS) can then be calculated following equation (1.4b). The separation of wind data into nondivergent and irrotational components was performed using the *windspharm* python module (Dawson, 2016). It features the calculation of horizontal derivatives on a sphere and the inversion of the Laplacian operator using spherical harmonics. As always, products of variables have to be calculated in grid space. To the end of this thesis, a new forcing expression will be developed that requires the calculation of vertical gradients (see Ch. 5). These are computed using the centred difference approximation on the pressure levels specified above.

The output variables of the model are relative vorticity, horizontal stream function, and nondivergent velocities u and v in grid space. In addition to that, the forcing interpolated to the model grid and time can be written to the output NetCDF files to check for errors in the interpolation process. The original output data are 6-hourly snapshots that are transformed into daily means after the model run using climate data operators (CDO). For the analysis in this thesis, all products and anomalies are calculated on the basis of daily means if not specified otherwise. For comparability, the reanalysis data is treated accordingly, i.e. it is transformed into daily means and interpolated onto the model grid. Solely the forcing uses 6-hourly resolution.

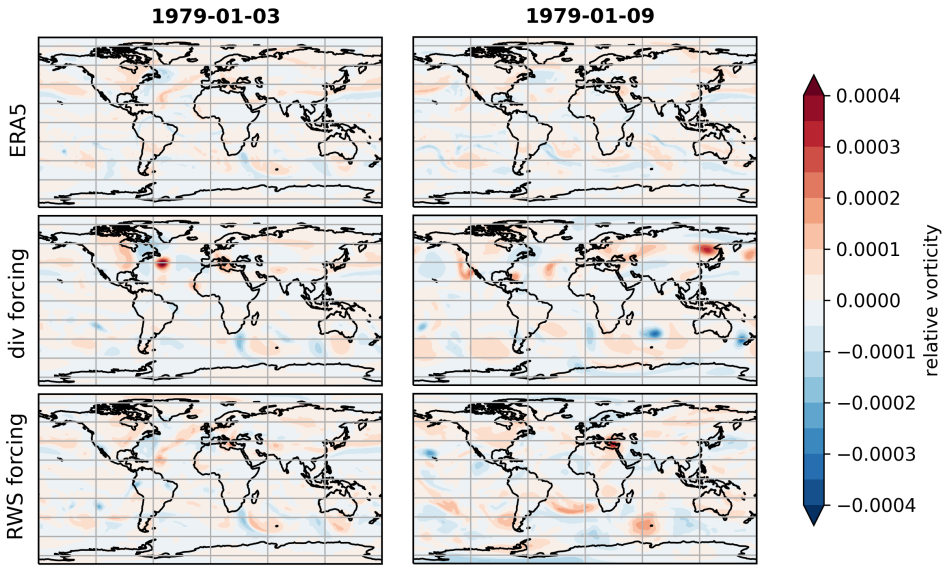

Figure 2.1.: *Snapshots of relative vorticity [1/s] at 1979-01-03 & 1979-01-09 from ERA5 (upper), the model with divergence forcing / interactive RWS (middle), and the model with RWS forcing (lower).*

2.4. Rossby wave source vs. divergence forcing

The RWS defined by Sardeshmukh and Hoskins (1988) is the horizontal convergence of the flux defined by the product of absolute vorticity and the divergent flow. The natural way to force a model that simulates the rotational flow is to specify the divergent flow only and to calculate RWS interactively by adding the divergent flow to the model velocities when calculating the absolute vorticity flux in step (1) of the algorithm. That was the first approach taken in this study. However, this approach was not successful. Figure (2.1) shows snapshots of relative vorticity from the model and reanalysis shortly after initialization. Extreme vortices with a circular shape and with positive vorticity on the northern hemisphere and negative vorticity on the southern hemisphere develop in the model when RWS is calculated interactively (i.e. divergence forcing). These instabilities deteriorate the modelled flow severely by creating large-scale extratropical easterlies. Of the different contributions to the RWS, the stretching of planetary vorticity was identified to be responsible for these instabilities. A broad range of measures was taken to cure these vortices which are

- a shorter time step
- a stronger linear friction
- a higher diffusivity
- a lower order of diffusion
- a higher spatial resolution
- a smoothed forcing

Neither of those measures were successful. Although the third-order Adams-Bashforth

scheme should be suitable for both friction and oscillation type equations, a mixed Adams-Bashforth-trapezoidal scheme was tested to treat vortex stretching separately. The tested algorithm

1. calculates the absolute vorticity flux by nondivergent velocities in grid space
2. calculates the flux convergence in spectral space
3. adds vorticity damping to the tendency in spectral space
4. treats that first part of vorticity tendency in spectral space using the Adams-Bashforth scheme
5. transforms that part of vorticity tendency to grid space
6. interpolates future divergence to model grid and time
7. treats the part of vorticity tendency due to vortex stretching in grid space using the trapezoidal scheme
8. deduces future variables

That mixed-scheme algorithm is more complicated due to the fact that the vorticity flux convergence and damping are most easily treated in spectral space but vortex stretching has to be treated in grid space due to the product of divergence and absolute vorticity. The time-stepping (step 4. & 7.) is summarized by the following equation where ζ is relative vorticity, f is planetary vorticity, h is the sum of absolute vorticity flux convergence and damping, and λ is the divergence specified as forcing:

$$\zeta^{n+1} = \zeta^n + \frac{1}{12}\left(23h(\widetilde{\zeta^n}) - 16h(\widetilde{\zeta^{n-1}}) + 5h(\widetilde{\zeta^{n-2}})\right) + \frac{1}{2}\left(\lambda^n(\zeta^n + f) + \lambda^{n+1}(\zeta^{n+1} + f)\right) \tag{2.17}$$

However, the approach to use a mixed Adams-Bashforth-trapezoidal scheme was not successful either. Therefore, the original intention to specify divergence and calculate RWS interactively was altered and the model is forced by RWS calculated with absolute vorticity from reanalysis. This has to be kept in mind for the interpretation of model results since much more information from reanalysis than the divergent flow only is specified to the model.

Although model experiments forced by RWS instead of divergence do diverge from reanalysis (see snapshots from 1979-01-09 in Fig. 2.1) and develop instabilities that are discussed below (see Ch. 3.2), RWS forcing performs fundamentally better than divergence forcing since it drives extratropical westerlies. The instabilities in RWS experiments are different in shape and do not show the sign sensitivity like the instabilities in divergence forcing experiments. They are believed to be of physical and not numerical origin. The model experiments driven by RWS are entitled `rws_200hPa_12days_initial1`, marking the vertical level of the forcing, the linear friction time scale in use, and the initial condition.

2.5. Damping parameters and resolution

The model uses linear friction and biharmonic diffusion to remove energy or enstrophy at large and very small scales (see eq. 2.1). The choice of the linear friction time scale r^{-1} has

a strong effect on the model output. Consequently, two different choices that encompass the range of time scales in the literature, 6 days and 12 days, will be tested throughout this study. The biharmonic diffusion is scale selective with a l^4 (horizontal wavenumber) proportionality. The viscosity κ (3.568×10^{15} m^4/s) is set to ensure a damping time scale of 0.1 days at the smallest resolved scale. This is rather low compared to other values used in the literature but it is sufficient to prevent enstrophy from piling up at small scales. More common values for viscosity like 2.338×10^{16} m^4/s (Simmons and Hoskins, 1978) were developed for models with lower resolution and introduce much shorter damping time scales in a relatively highly resolved model like this.

The horizontal resolution of the model is set by triangular truncation at wavenumber 85 (T85). That corresponds to a grid resolution of 1.4° on average. In order to test this model configuration, parameters like the biharmonic viscosity and model resolution were varied. Figure (2.2) shows the resultant time-mean enstrophy spectra from 1979 in comparison with reanalysis. More specifically model output and reanalysis vorticity are transformed into spherical harmonics. The absolute values of the squared complex spectral coefficients are then averaged over time and all combinations of zonal wavenumber m and meridional wavenumber n that share a common total wavenumber $l = m + n$ and plotted against total wavenumber. For an explanation of spherical harmonics and wavenumbers see section (2.1).

These enstrophy spectra should be seen in the context of geostrophic turbulence (see Ch. 1.1 for details). Spectral enstrophy is largest at intermediate wavenumbers caused by stirring from the specified RWS and damped at small and large wavenumbers by linear friction and biharmonic diffusion. In between, inertial ranges in the form of power laws can be seen. The linear friction parameter r clearly has a strong effect at small horizontal wavenumbers ($l < 10$) with less enstrophy for stronger friction. The discrepancy with reanalysis illustrates a model bias that will be elaborated on in section (3.2). (For details on the reanalysis data see section 2.3.) At high wavenumbers, the effect of linear friction is small and diffusion dominates. The viscosity chosen for this study ensures a quite realistic enstrophy spectrum when compared to reanalysis. A higher viscosity deteriorates the enstrophy inertial range and a lower viscosity allows enstrophy to pile up at very large wavenumbers. The benefit of a finer model resolution, T127 instead of T85, is small in particular at small wavenumbers. For the sake of computational efficiency, the spectral resolution of T85 was chosen for the rest of this study. Moreover, the model appears to be insensitive to very small scale forcing since the effect of smoothing forcing to a spectral resolution of T42 is negligible. That vindicates the choice of T85 as the spectral resolution for the forcing and the model.

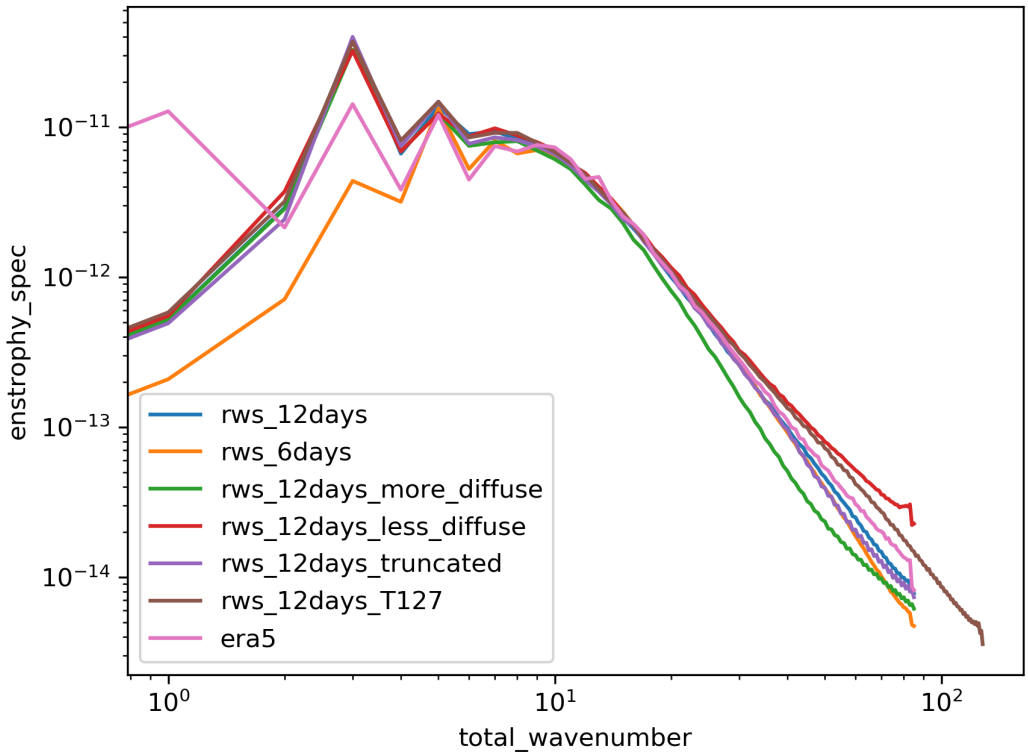

Figure 2.2.: *Time-mean (1979) spectral coefficients of enstrophy ζ^2 averaged across zonal wavenumbers for various model experiments and for ERA5 reanalysis data. The model experiments are forced by RWS. Unless specified differently they have a spectral resolution of T85, a linear friction time scale of 12 days, and a viscosity of 3.568×10^{15} m^4/s. The more diffuse experiment has a viscosity of 2.338×10^{16} m^4/s, the less diffuse experiment has a viscosity of 7.122×10^{14} m^4/s and for the truncated experiment the forcing was smoothed horizontally to T42.*

3. A barotropic model with realistic Rossby wave source

This chapter starts the evaluation of the barotropic vorticity equation model driven by a time series of Rossby wave source (RWS) which is diagnosed from the atmospheric reanlysis ERA5. The model is expected to reproduce the upper-tropospheric (200hPa & 300hPa) rotational flow from reanalysis, an expectation that cannot be realised. Before evaluating the model performance, the forcing will be examined in detail and the horizontally nondivergent flow from reanalysis will be illustrated in maps of the climatological mean. These are then compared to the output of two different model configurations (weak & strong linear friction). The role of barotropic instability is analysed by means of climatological mean kinetic energy in ensemble experiments. To gain further insight, the variability of area-averaged kinetic energies and a regional climate index is investigated.

3.1. Rossby wave source diagnosed from reanalysis

Figure (3.1) shows time-mean Rossby wave source RWS and variance of daily means diagnosed from reanalysis at 200hPa and 300hPa. Please note that these fields are smoothed to a spectral resolution of T42 and resampled into daily means for the purpose of plotting, to remove intense small scale peaks. Thus, they differ from those fields actually specified to the model (see Ch. 2.3 for details). For the interpretation of figure (3.1), bear in mind that RWS is connected to the flow by the vorticity tendency equation. It means that a positive RWS to the left and a negative RWS to the right in the direction of the flow maintains a positive flow anomaly against dissipation or advection. In the climatological mean, this is the case for the subtropical jets: At 200hPa over the subtropical North Atlantic and over China, positive time-mean RWS north of negative values indicates a westerly jet entry whereas negative time-mean RWS north of positive values over the Eastern Pacific indicates a jet exit region. Mountain ranges like the Himalaya and the Andes cause small scale structures in the RWS. High variance of RWS can be seen in the extratropics, e.g. over Japan and the western North Atlantic. These are also the locations of eddy-driven jets. (The jets' locations in reanalysis and the barotropic model will be discussed below; see fig. 3.5, 3.7 & 3.9). Also, note that both time mean and variance of RWS are very weak in the deep tropics. Chapter (5) will put special emphasis on this point.

The general picture at 300hPa is similar to 200hPa. The temporal mean RWS is slightly weaker compared to 200hPa. In terms of variance, the differences are more interesting. In the northern hemisphere, the variance is moved poleward at 300hPa compared to 200hPa. In the southern hemisphere, the variance is reduced substantially at 300hPa, particularly for the subtropical jet. To assist the understanding of these differences between levels, note that the tropopause height shallows from the tropics to higher latitudes. From personal ex-

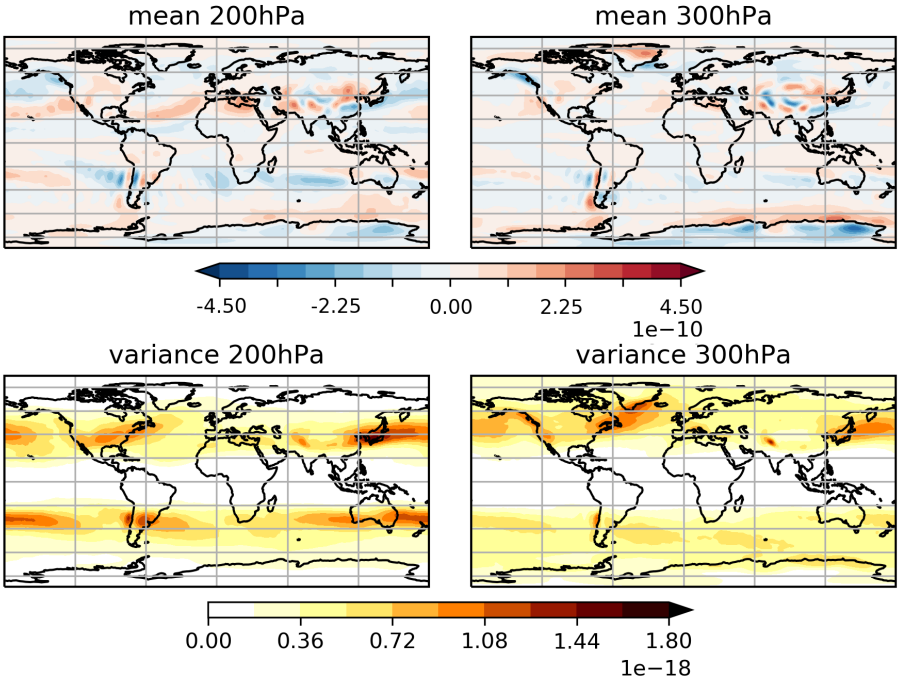

Figure 3.1.: *Temporal mean & variance of daily mean Rossby wave source [s^{-2}] at 200hPa & 300hPa from reanalysis smoothed to T42.*

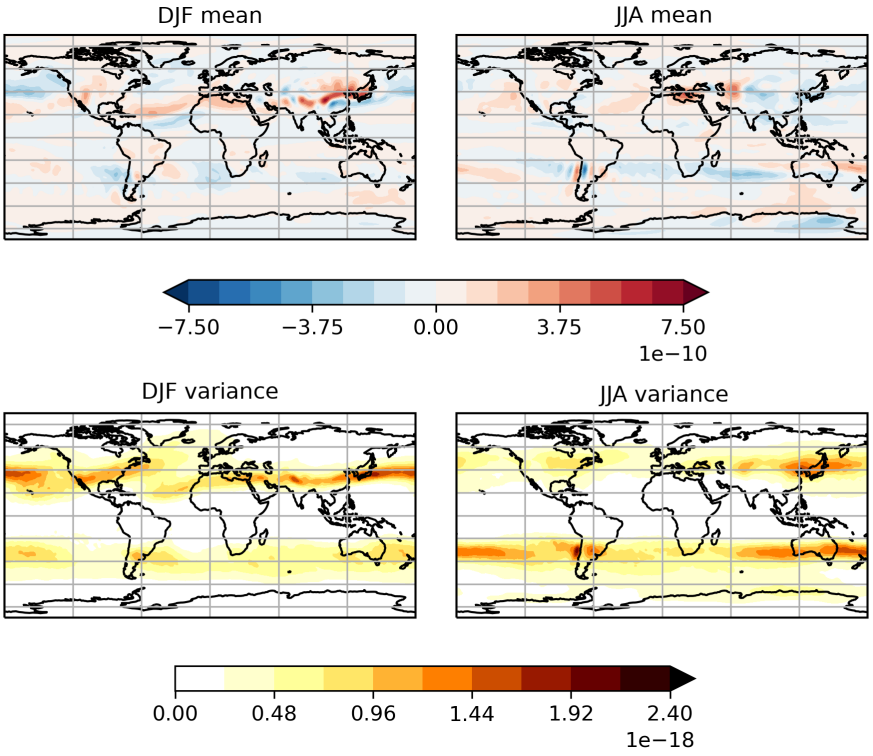

Figure 3.2.: *Temporal mean & variance of daily mean Rossby wave source [s^{-2}] at 200hPa from reanalysis grouped by season and smoothed to T42.*

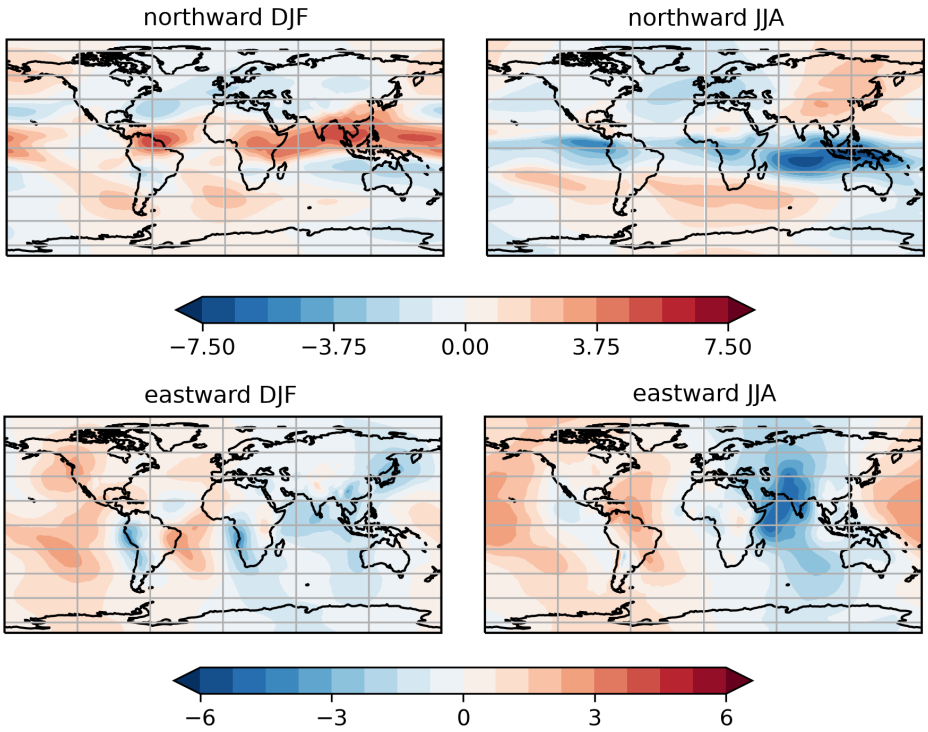

Figure 3.3.: *Seasonal mean irrotational wind [m/s] at 200hPa from reanalysis.*

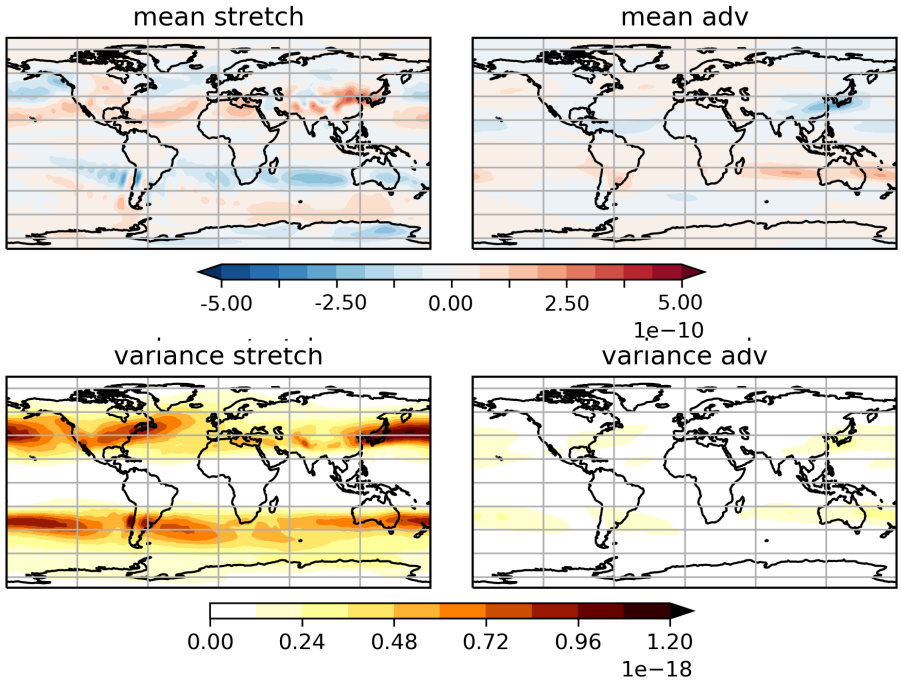

Figure 3.4.: *Temporal mean & variance of daily mean vortex stretching [s^{-2}] and horizontal vorticity advection by the divergent flow [s^{-2}] at 200hPa calculated from daily mean reanalysis data and smoothed to T42.*

perience with synoptic weather charts, the author would expect 200hPa to be more relevant for the subtropical and 300hPa more relevant for the eddy-driven jet.

RWS in reanalysis has a pronounced seasonal cycle. Seasonal means and variance are shown separately for boreal winter and summer in figure (3.2). Spring and autumn comprise the transition between these two states. In both hemispheres, the seasonal mean is strongest in winter with strong meridional contrasts between positive and negative vorticity forcing. The strengthening in winter holds for variance as well. In addition to that, an equatorward shift of variance can be seen in comparison to summer.

An important source of seasonality in RWS is the seasonal cycle of the divergent flow $\vec{u_\chi}$ displayed in figure (3.3). The meridionally moving Intertropical Convergence Zone (ITCZ) is associated with strong northward flow in DJF and southward flow in JJA in the equatorial band. The irrotational zonal wind represents the Walker circulation caused by rising motion over the Maritime Continent which is strongest in JJA. At 300hPa the divergent flow is considerably weaker than at 200hPa both in terms of temporal mean and variance (not shown). This explains the differences in temporal mean RWS between 200hPa and 300hPa and the reduction of RWS variance at the southern hemispheric subtropical jet at 300hPa.

The RWS plotted in figures (3.1,3.2) consists of contributions due to vortex stretching $(-(\nabla_h \cdot \vec{u_\chi})(\zeta + f))$ and horizontal advection of absolute vorticity by the divergent flow $(-\vec{u_\chi} \cdot \nabla_h(\zeta + f))$. To gain further insight into how these contributions drive the upper tropospheric flow, they are illustrated separately in figure (3.4). Jointly, the temporal means of vortex stretching and vorticity advection create the subtropical jet. At the poleward flank of the jet in the northern hemisphere, positive vorticity tendency by stretching can be seen. At the equatorward flank, the poleward divergent flow advects negative vorticity. In the southern hemisphere, the two contributions have inverse signs. In contrast, the variance of daily mean RWS - and therefore the eddy-driven jet - is caused almost entirely by vortex stretching. Small contributions of vorticity advection to the variance of RWS can be seen to the east of the Chinese coast and around Australia, equatorward of the variance caused by vortex stretching.

3.2. Characteristics of a nonlinear barotropic model

In order to compare reanalysis data to the output of the vorticity equation model, the rotational (nondivergent) flow was first extracted from its horizontal velocities. The evaluation is started by investigating the climatological mean horizontal flow.

In reanalysis, the seasonal mean zonal winds at 200hPa are dominated by the westerly jets that peak around 90m/s over the North Pacific in DJF (see Fig. 3.5 a). The zonal mean character of the subtropical and the eddy-driven jet is elaborated in chapter (1.2). However, figure (3.5 a) reveals zonal asymmetry. There is an Atlantic jet tilted northeast, an Asian jet oriented zonally from North Africa to the Pacific, and a third jet on the southern hemisphere spanning across the globe. These jets are strongest in winter and change their spatial structure over the year. Equatorial winds are relatively weak compared to the westerly jets but they tend to be easterly over the Indian Ocean and westerly over the eastern Pacific.

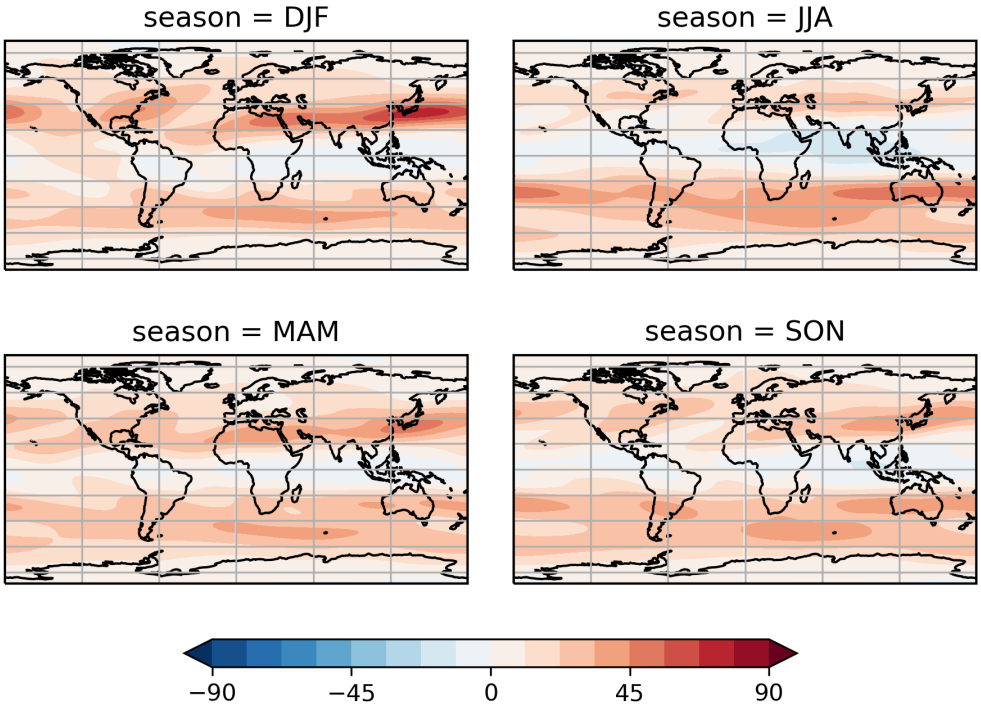

(a) *seasonal mean* $[m/s]$

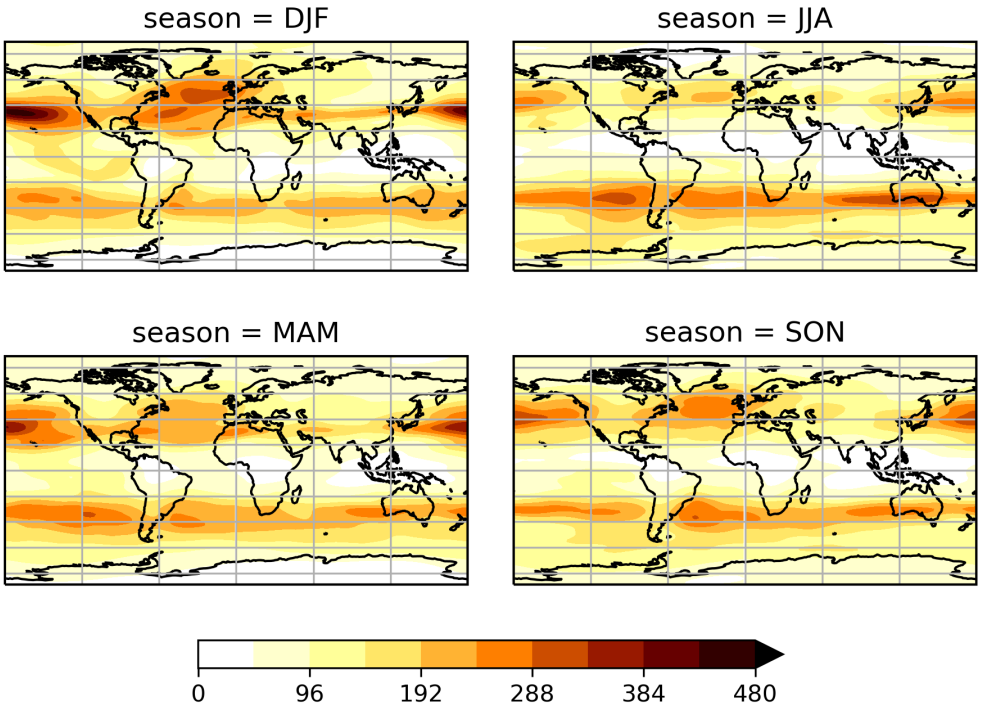

(b) *variance of daily means* $[(m/s)^2]$

Figure 3.5.: *Nondivergent zonal wind from reanalysis at 200hPa.*

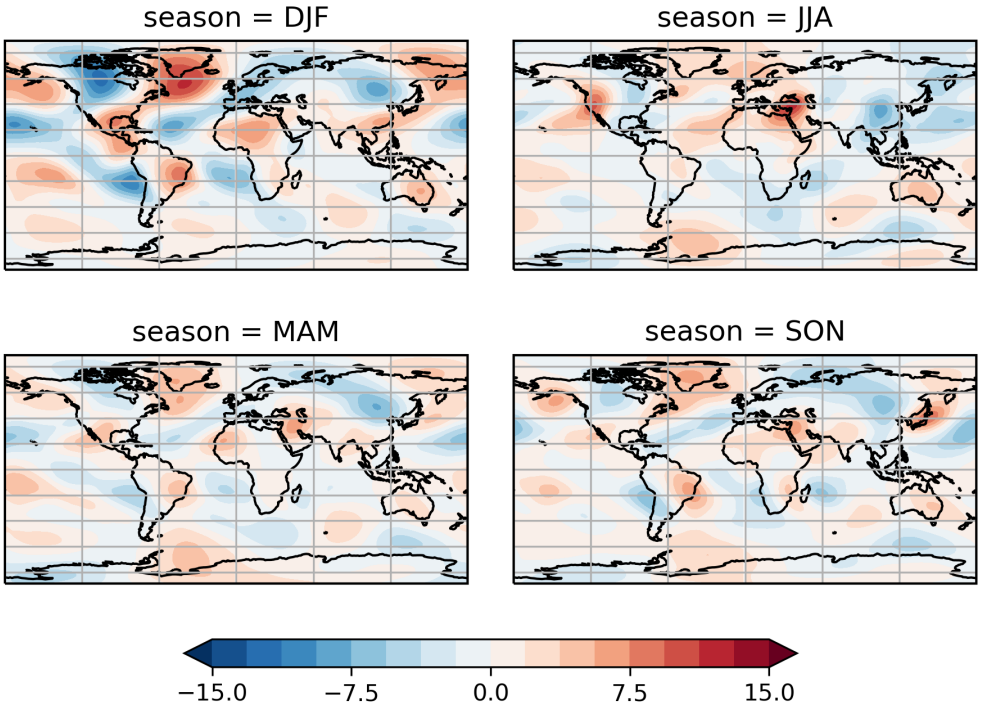

(a) *Nondivergent meridional wind* $[m/s]$

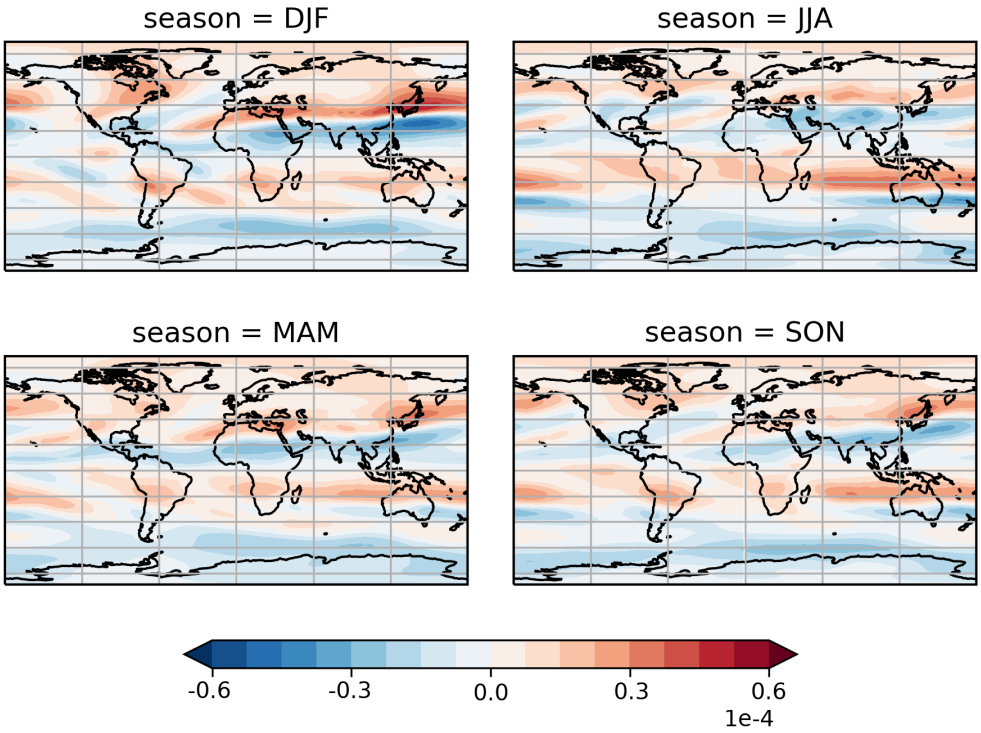

(b) *Relative vorticity* $[1/s]$

Figure 3.6.: *Seasonal means from reanalysis at 200hPa.*

The seasonal mean meridional wind (Fig. 3.6a) depicts the stationary eddies caused by topography and land-sea heat contrast. There is meridional convergence at the jet entry (e.g. over the Mediterranean and China in DJF) and divergence at the jet exit. That is reasonable, of course, as meridional convergence has to feed zonal divergence in a horizontally nondivergent flow. Seasonal mean meridional velocities are substantially weaker than the zonal wind speeds. Favoured by stronger temperature gradients, the stationary eddies in the northern hemisphere are strongest from December to February. The variance of horizontal velocities mirrors the spatial structure of the seasonal mean jets, although, stronger over the ocean than over the continents (Fig. 3.5b). Variance is shown for zonal velocity only but it is similar in structure and amplitude to the variance of meridional velocity. Similar to the seasonal means of horizontal velocities, also the variance exhibits a seasonal cycle, being strongest in the winter hemisphere. The plots of seasonal mean relative vorticity (Fig. 3.6b) do not provide any additional information to that given by the seasonal means of nondivergent zonal and meridional velocity (Fig. 3.5a & 3.6a). However, it is an alternative way to illustrate the locations of the jet given as strong contrasts of relative vorticity with positive values to left in the direction of the flow. Also, they are useful to compare with plots of RWS (Fig. 3.1 & 3.2).

Model evaluation: temporal mean The barotropic vorticity equation model reproduces the nondivergent flow from reanalysis to only a limited extent. The figures (3.7) and (3.8) are the equivalent to figures (3.5) and (3.6) for reanalysis but show model results for the weak linear friction (12 days) case. Most obvious is the weakness of the westerly jets, about half in strength compared to reanalysis (note the different color scales). They are also different in terms of zonal symmetry: the Asian jet is wavier and the maxima of jets are slightly shifted upstream compared to reanalysis. The weakness and waviness of the jets can be seen in plots seasonal mean relative vorticity too (Fig. 3.8b). Contrasts of relative vorticity are weaker than in reanalysis and less elongated in the dimension of longitude. Meridional winds are quite realistic in strength. But interestingly, there is a strong upstream phase shift of the stationary eddies (Fig. 3.8a compared to 3.6a). This phase shift could be explained by the weakened zonal-mean zonal wind, and consequently a reduced self-advection of the flow in the model. This shift of the stationary eddies might feedback on the strength of extratropical jets. Therefore it is important to be understood. Relative to the big discrepancy in the time-mean strength of the westerly jets, the seasonal cycle is well captured with the jets being considerably stronger in winter than in summer. The tropics show much stronger and zonally more symmetric easterlies than seen in reanalysis. This will be elaborated on in detail together with equatorial RWS in chapter (5).

Equally conspicuous as the weakening of the seasonal mean zonal wind in the model compared to reanalysis is the strengthening of variance (Fig. 3.7b). For both zonal and meridional velocity, the variance is increased more than twice. In addition to the increase, a broadening in spatial extent can be observed. The excess variance in the model is not evenly distributed across time scales, as discussed below, indicating a misrepresentation of internal processes on synoptic and sub-seasonal timescales. Apparently, the westerly jets in this barotropic model are more unstable than in reality and therefore weakened.

One way to reduce the excess variance in the model is to increase linear friction. The variance of horizontal velocities is reduced by about one quarter if the damping time scale is reduced

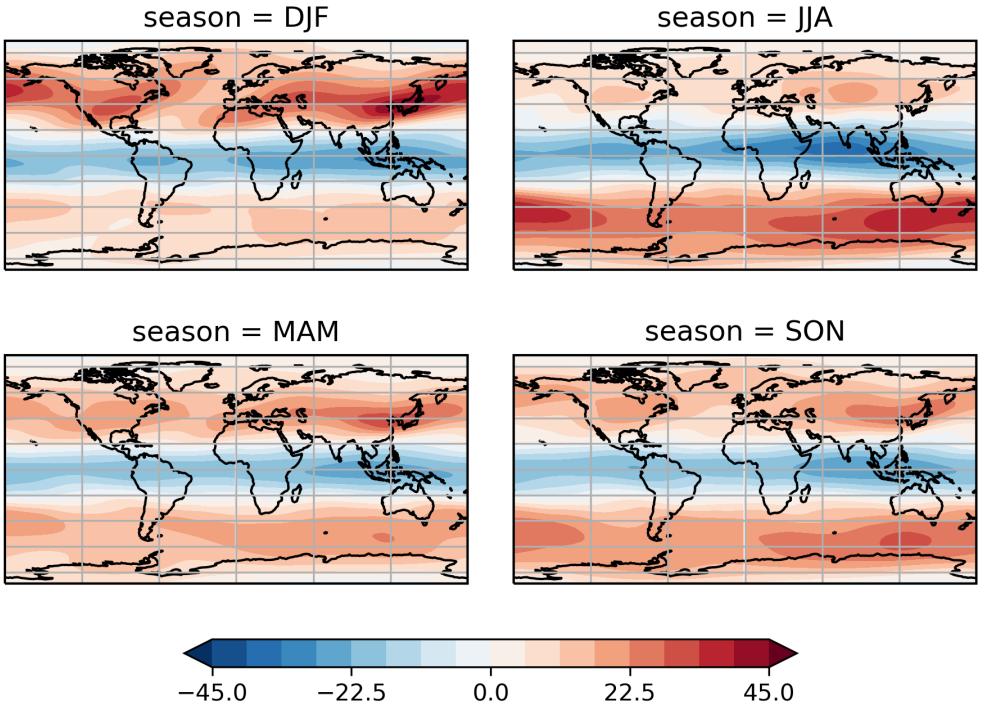

(a) *seasonal mean* $[m/s]$

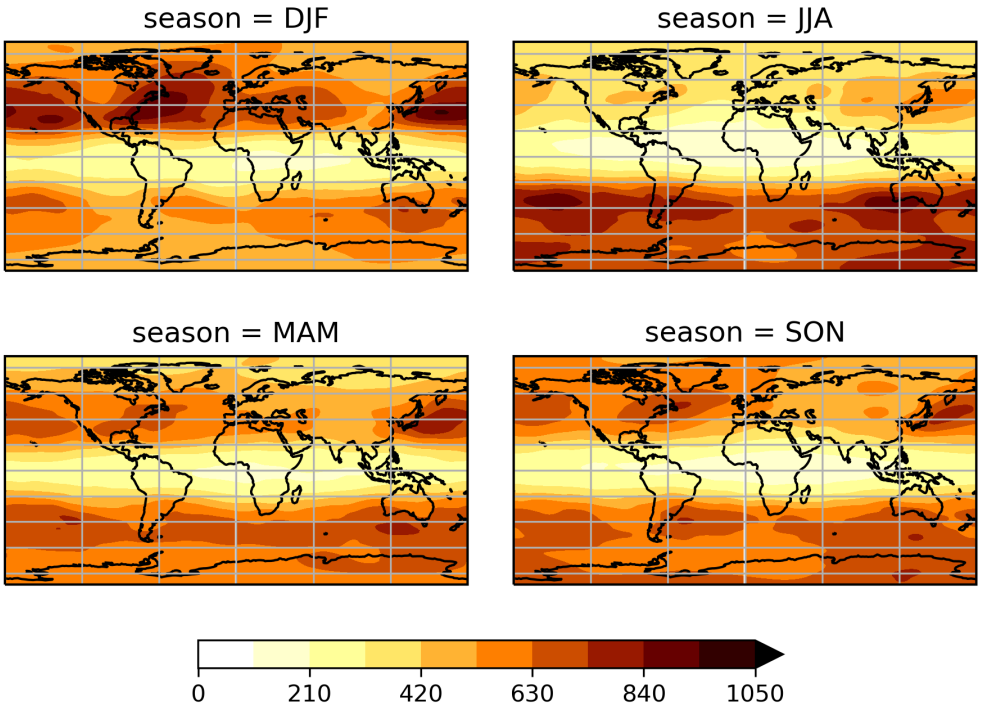

(b) *variance of daily means* $[(m/s)^2]$

Figure 3.7.: *Modelled zonal wind from a single realisation with a 12-day linear friction time scale.*

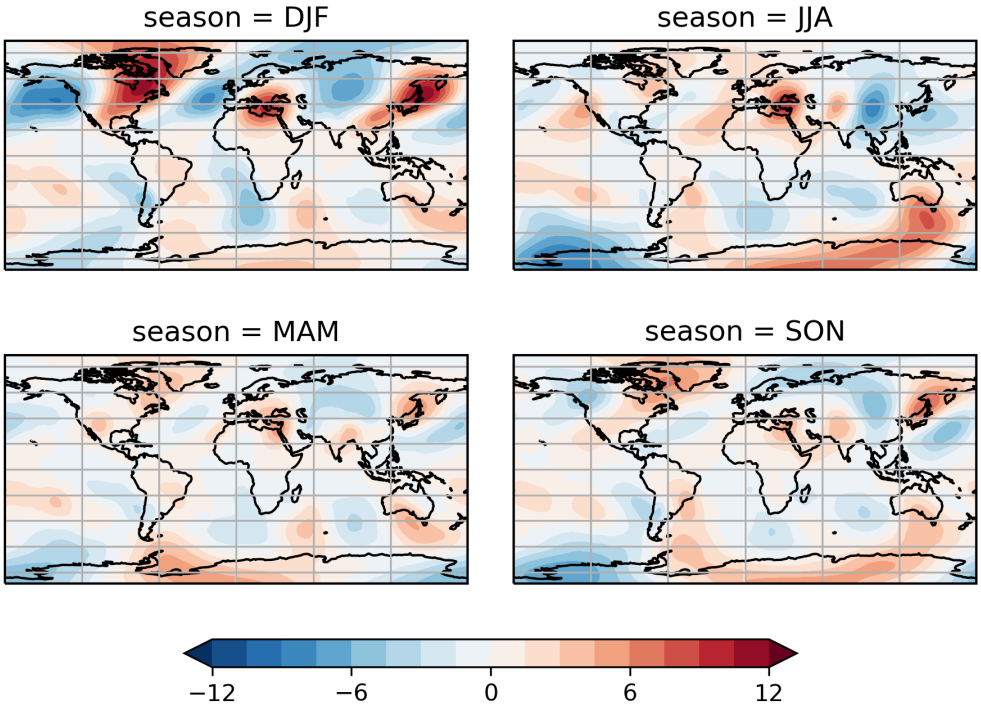

(a) *Meridional wind* $[m/s]$

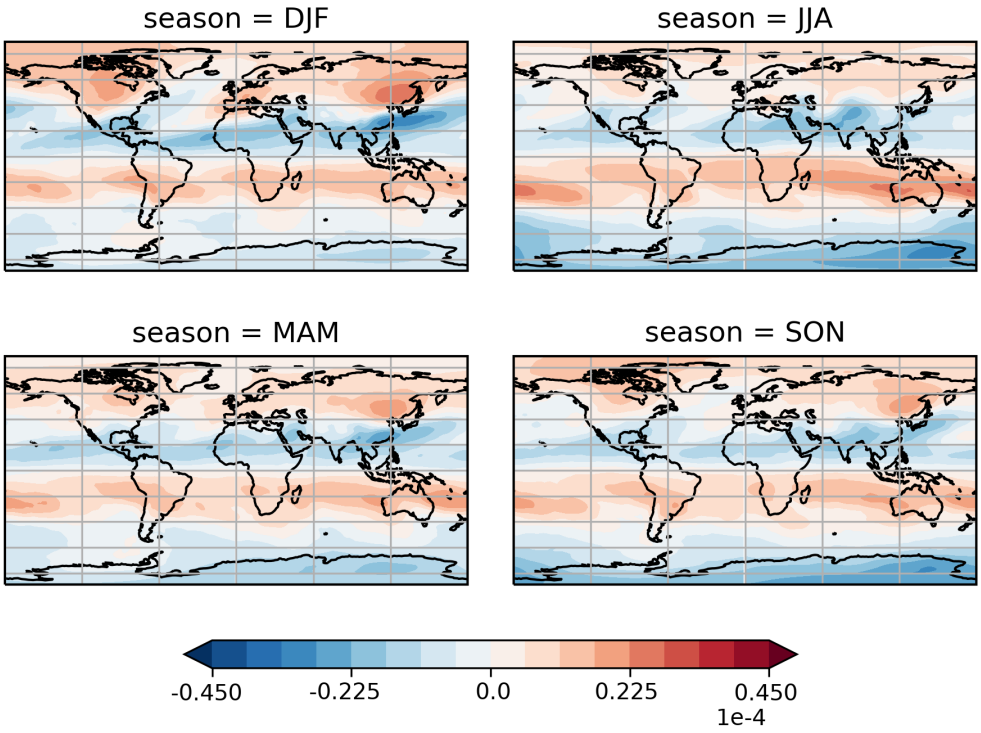

(b) *Relative vorticity* $[1/s]$

Figure 3.8.: *Seasonal means from a single realisation of the model with a 12-day linear friction time scale.*

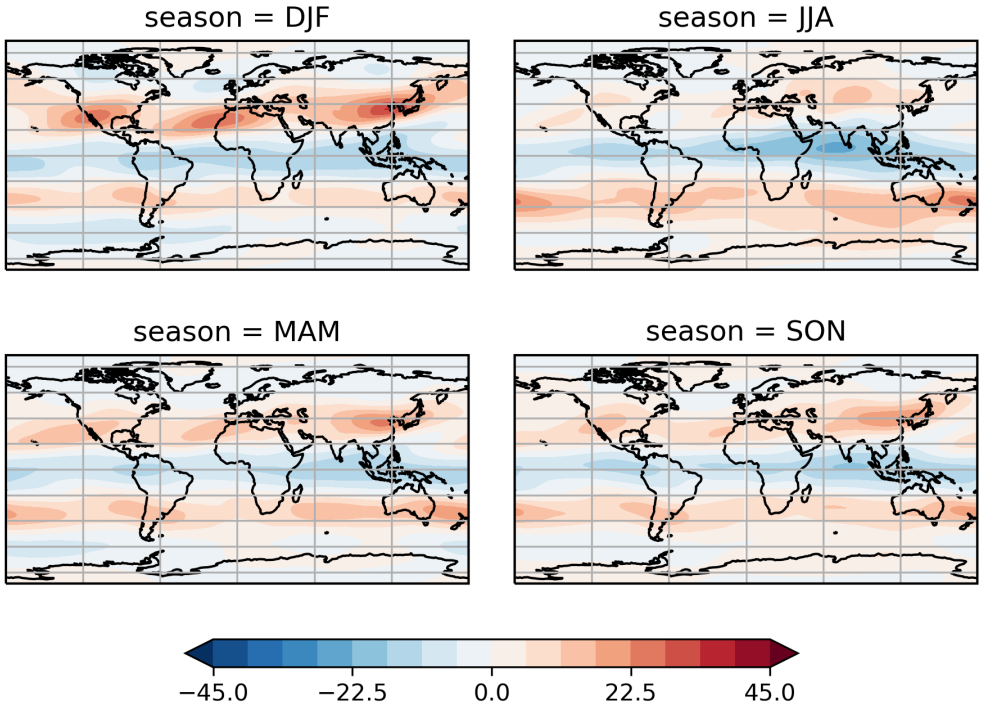

Figure 3.9.: *Seasonal mean modelled zonal wind* $[m/s]$ *from a single realisation with a 6 days linear friction time scale.*

from twelve to six days (not shown). It is still too high though, and the spatial structure does not change substantially. This improvement has to be paid for with additional weakening of the seasonal mean jets compared to reanalysis (see Fig. 3.9). In the northern hemisphere, the two jets split into three maxima over the United States, northwest Africa and over China. That represents an additional upstream shift in comparison to reanalysis. Furthermore, easterly winds develop poleward of the westerly jets and the equatorial easterlies remain. A trade-off has to be made between the variance and the mean state. The 12-day friction time scale might be the better choice.

So far, the barotropic model and reanalysis have been compared using a number of global horizontal maps. A more direct comparison of model experiments with different friction parameters at different vertical levels to reanalysis is enabled by reducing dimensionality and plotting time-mean, zonal-mean zonal wind in figure (3.10). The severe effect of strong linear friction (6-day time scale) is directly visible. The zonal-mean velocity in the extratropics is far too weak if not even easterly. The extratropical mean state is represented much better in the model with a 12-day friction time scale, although, the maximum of zonal-mean zonal wind is shifted polewards in comparison with reanalysis. This shift might be an indication for a larger model bias for the baroclinic subtropical jet than for the barotropic eddy-driven or polar jet. In reanalysis, the difference between 200hPa and 300hPa is a weakening of the subtropical jet, and in the model, a stronger poleward shift. And again the discrepancy of the model at the equator has to be stressed. The zonal-mean equatorial easterlies are too

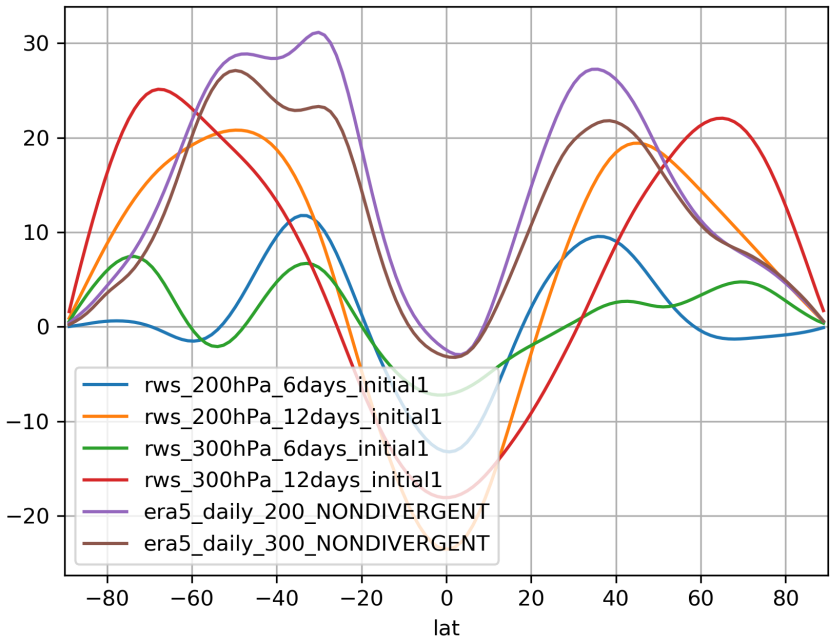

Figure 3.10.: *Time-mean, zonal-mean zonal wind* $[m/s]$ *from various model experiments and reanalysis.*

strong by a factor of up to ten.

In addition to tuning linear friction, two ways to reduce the excess variance in the model have been testes: nudging and ensemble averaging. Nudging means a relaxation of the model to time-mean vorticity on the same time scale as linear friction (6 & 12 days). This approach also implies that only RWS anomalies from the time mean are specified. (The overbars in eq. (3.1) denote a climatological annual mean.)

$$\frac{\partial \zeta}{\partial t} + \nabla \cdot (\vec{u}_\psi(\zeta + f)) = -r(\zeta - \overline{\zeta}) - \kappa \nabla^4 \zeta + (RWS - \overline{RWS}) \tag{3.1}$$

At this point, it is worth noting that nudging is equivalent to penalising a high rate of change, demonstrated by simple integration in the following equations. The constant ϵ in (3.2) represents r in (3.1) and C represents $r\overline{\zeta}$.

$$\frac{d}{dt}\left(\frac{dU}{dt}\right) = -\epsilon \frac{dU}{dt} \tag{3.2a}$$

$$\Rightarrow \frac{dU}{dt} = -\epsilon U + C \tag{3.2b}$$

However, this approach was not successful. The variance was reduced but was still too large by more than 50%. Despite this improvement, the seasonal mean zonal wind suffered by an increased zonal symmetry and a weakened seasonal cycle (not shown). So the intention to have RWS creating the seasonal cycle, and to specify anomalies from the climatological annual mean, failed. Therefore, nudging will not be considered any further.

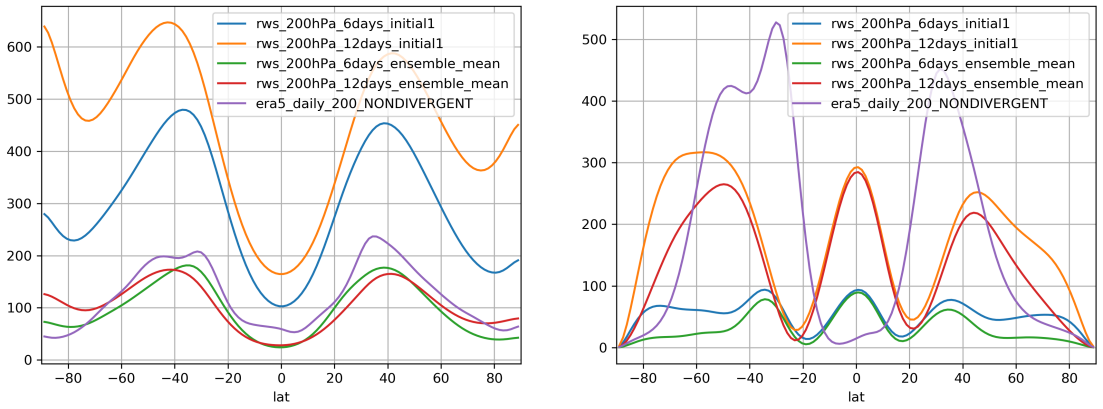

(a) *Eddy kinetic energy* ($\overline{eKE}$) **(b)** *Zonal mean flow kinetic energy* ($\overline{KEzm}$)

Figure 3.11.: *Time-mean, zonal-mean kinetic energy* $[m^2/s^2]$ *from various model experiments and reanalysis at 200hPa.*

Ensemble averaging, on the other hand, is meant to remove internal and isolate forced variability. It turns out to be more successful than nudging. Each ensemble is made of ten members with ten different initial conditions. All members were initialized at 01.01.1979 00:00:00 and experience the same forcing. The initial conditions were evenly spaced and taken from the first nine days of January 1979. The choice for initial conditions encompasses synoptic variability but should not influence more low-frequency processes like teleconnections. Ten ensemble members should be enough to calculate a meaningful average. A quick test for the convergence of the ensemble mean regarding ensemble size is made below by comparing power spectra of relative vorticity.

Ensemble averaging does not change the time-mean flow as it is plotted for example in figure (3.10), in contrast to the time mean of squared quantities. Evaluating the benefit of ensemble averaging is thus started by showing time-mean, zonal-mean kinetic energy, (Fig. 3.11). The zonal-mean kinetic energy of the total flow is, of course, larger than the kinetic energy of the zonal-mean flow $[u]$, $[v]$ (KEzm). The deviations from the zonal-mean flow u^*, v^* will be called *eddies* and their zonal-mean energy *eddy kinetic energy* (eKE). (That terminology differs from oceanography standard.) Hence, the zonal-mean kinetic energy is

$$\frac{1}{2}\left[u^2+v^2\right] = \underbrace{\frac{1}{2}\left([u]^2+[v]^2\right)}_{KEzm} + \underbrace{\frac{1}{2}\left[(u^*)^2+(v^*)^2\right]}_{eKE} \tag{3.3}$$

For a single realisation, time-mean $\overline{\text{eKE}}$ computed from daily data is increased more than twice compared to reanalysis depending on the strength of linear friction (Fig. (3.11a)). The latitudinal structure of $\overline{\text{eKE}}$ with maxima in mid-latitudes and minima at the equator and in high latitudes is similar. The benefit of ensemble averaging in this matter is strong. Using the ensemble mean flow to compute energies reduces the amplitude of $\overline{\text{eKE}}$ to that level seen in reanalysis. The biggest discrepancy can be seen at the equator with too little energy in the model. Interestingly, the strength of linear friction plays a minor role after ensemble averaging.

The picture of time-mean $\overline{\text{KEzm}}$ is, to some extent, quite similar to the time-mean, zonal-mean flow. The model results differ from reanalysis in both amplitude and latitudinal structure. That is true regardless of whether energies are calculated for a single realisation or the ensemble-averaged flow. However, ensemble averaging does reduce $\overline{\text{KEzm}}$ in higher latitudes. That might be simply because small scale structures project more strongly onto the zonal mean in high latitudes than in low latitudes. In contrast to the plots of $\overline{\text{eKE}}$, the strength of linear friction does matter after ensemble averaging.

Model evaluation: domain averaged variability Time-mean quantities give some indication about model characteristics. However, it is insightful to examine variability as well. In order to do so, kinetic energies are split into contributions by the time-mean flow $\bar{u}$, $\bar{v}$ and the transient flow u', v' for both KEzm and eKE. The following equations for time-mean, zonal-mean kinetic energy include contributions due to the time-mean, zonal-mean flow ($\text{KE}\overline{\text{zm}}$), the transient zonal-mean flow ($\overline{\text{KEzm}'}$), the stationary eddies ($\bar{\text{e}}$KE), and the transient eddies ($\overline{\text{e}'\text{KE}}$).

$$\underbrace{\frac{1}{2}\overline{([u]^2+[v]^2)}}_{\overline{KEzm}} = \underbrace{\frac{1}{2}\left([\overline{u}]^2+[\overline{v}]^2\right)}_{KE\overline{zm}} + \underbrace{\frac{1}{2}\overline{([u']^2+[v']^2)}}_{\overline{KEzm'}} \qquad \text{(KEzm)} \qquad (3.4a)$$

$$\underbrace{\frac{1}{2}\overline{[(u^*)^2+(v^*)^2]}}_{\overline{eKE}} = \underbrace{\frac{1}{2}\left[(\overline{u}^*)^2+(\overline{v}^*)^2\right]}_{\bar{e}KE} + \underbrace{\frac{1}{2}\overline{[(u'^*)^2+(v'^*)^2]}}_{\overline{e'KE}} \qquad \text{(eKE)} \qquad (3.4b)$$

Table (3.1) lists the kinetic energies of the time-mean flow from reanalysis, single realisations and ensemble averages of the model experiments. As shown already in figure (3.10), the time-mean, zonal-mean flow in the model has too weak extratropical westerlies and too strong tropical easterlies depending upon friction but independent of ensemble averaging. That is demonstrated again by the area-averaged $\text{KE}\overline{\text{zm}}$. The stationary eddy flow is represented significantly better, although, the values of $\bar{\text{e}}$KE are too small in the model compared to reanalysis.

The qq-plots in figure (3.12) compare the probability distributions of transient flow kinetic energies from the model experiments to those from reanalysis. More specifically, the percentiles of zonal-mean flow kinetic energy and eddy kinetic energy distributions are cal-

Table 3.1.: *Area averages of time-mean flow kinetic energies in m^2s^{-2}, i.e. extratropical and tropical zonal-mean flow kinetic energy ($KE\overline{zm}$) and eddy flow kinetic energy ($\bar{e}KE$), from several datasets.*

	90N-20N $\text{KE}\overline{\text{zm}}$	90N-20N $\bar{\text{e}}$KE	20N-20S $\text{KE}\overline{\text{zm}}$	20N-20S $\bar{\text{e}}$KE
era5_200_NONDIVERGENT	204	19	23	14
rws_200hPa_6days_initial1	18	11	41	5
rws_200hPa_6days_ensemble_mean	18	11	40	5
rws_200hPa_12days_initial1	94	9	155	5
rws_200hPa_12days_ensemble_mean	93	9	155	5

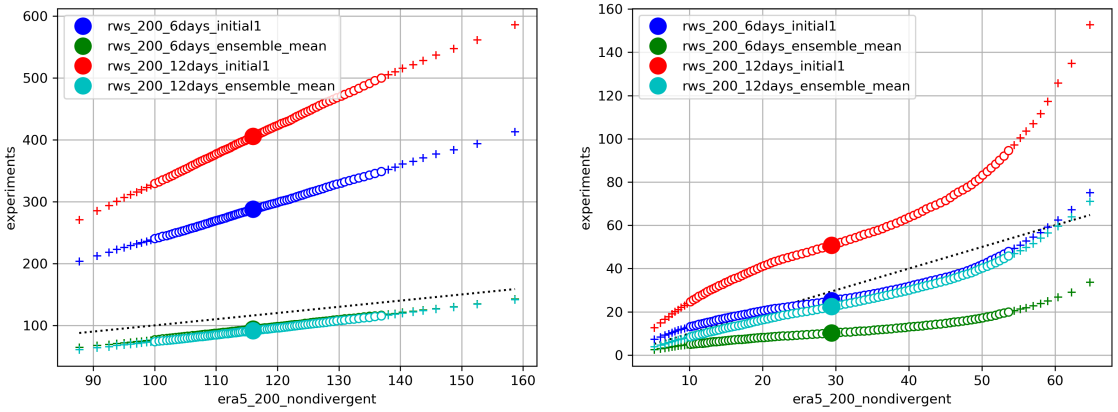

(a) *Eddy kinetic energy of daily mean anomalies ($e'KE$)*

(b) *Zonal-mean flow kinetic energy of daily mean anomalies ($KEzm'$)*

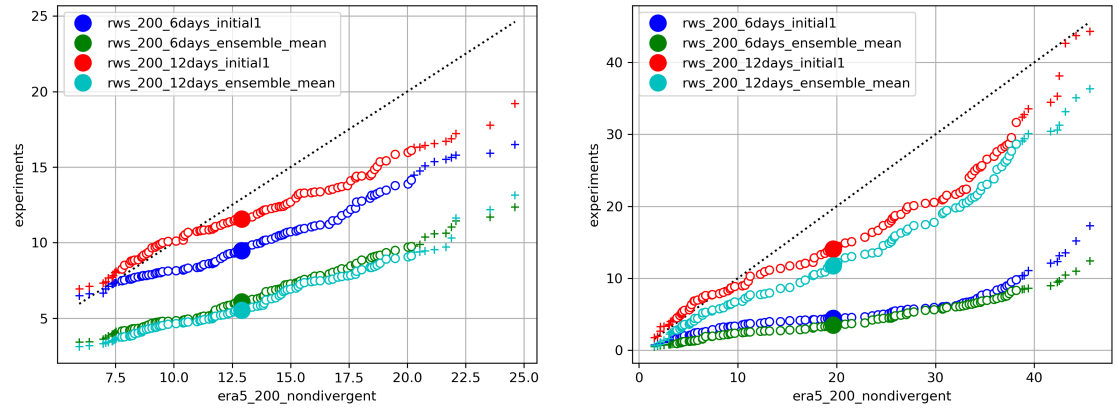

(c) *Eddy kinetic energy of 90-day mean anomalies ($e'KE$)*

(d) *Zonal-mean flow kinetic energy of 90-day mean anomalies ($KEzm'$)*

Figure 3.12.: *Percentiles of globally averaged kinetic energies of the transient flow from model experiments plotted against the percentiles from reanalysis (the solid circle indicates the median, crosses indicate the <10% and >90% extremes, the main diagonal is dashed).*

culated from transient velocities resampled to daily means and 90-day means. An overall vertical displacement of the data points from the main diagonal represents a mean shift of the distribution and the slope of the data points represents its variance. A departure from a straight line is caused by differing higher statistical moments, e.g. skewness and kurtosis, of the experiments' energy distributions compared to the reference dataset.

On daily timescales, the eddy field of a single realisation of a model experiment is too energetic (Fig. 3.12 a). The strong mean and variance of e′KE are cured by using the ensemble mean. Also resampling to 90-day means reduces the mean and variance of modelled e′KE, both absolutely and relatively compared to reanalysis. Indeed, on long time scales the values of e′KE are not too high but too low compared to reanalysis. As seen before (Fig. 3.11), the strength of linear friction does not matter for the ensemble mean eddy flow. The kinetic energy of the zonal-mean transient flow (KEzm′) depends on the damping time

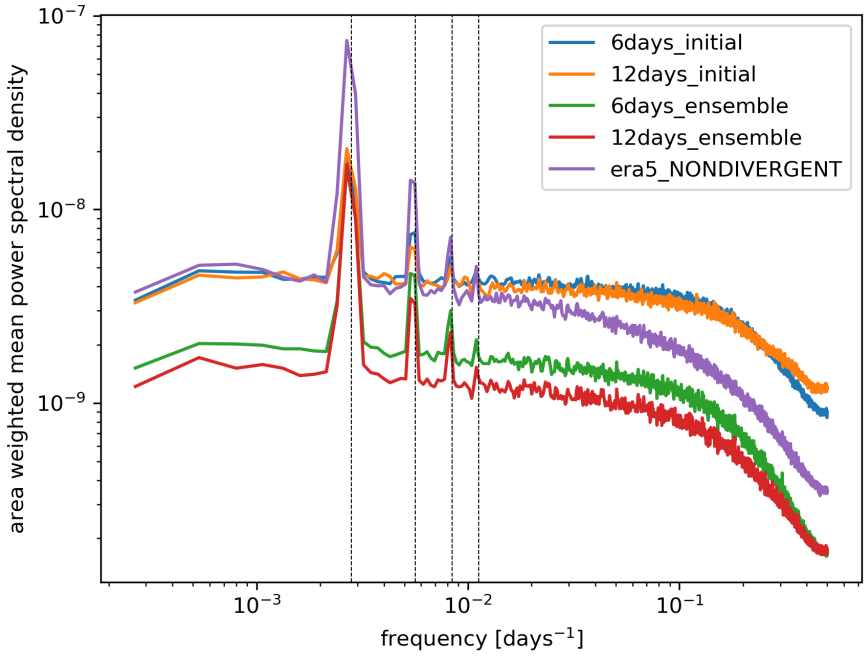

Figure 3.13.: *Area-weighted global mean power spectral density of vorticity [$s^{-2}/days^{-1}$] from reanalysis and RWS model experiments at 200hPa; vertical lines indicate the annual cycle and first three higher harmonics.*

scale and the ensemble size (i.e. single realisation or ensemble mean). The latter loses its relevance on long timescales. In the model, KEzm′ is more strongly tailed than in reanalysis (i.e. higher kurtosis and skewness). The 90-day zonal-mean flow has too little mean energy and energy variance.

More insight in how variance is distributed across time scales can be provided by vorticity power spectra in frequency space. Figure (3.13) shows on logarithmic coordinate axes the global average of power spectral density (PSD) of vorticity from model experiments and reanalysis at individual grid points. To reduce noise, Welch's method was applied with four linearly detrended sub time series with zero mean. These power spectra look like white noise at low frequencies, have peaks at the annual cycle ((365 days)$^{-1}$) and its higher harmonics, and look like red noise at high frequencies.

Single realisations of the model agree well with reanalysis at low frequencies where both model and reanalysis have white noise characteristics. At high frequencies, however, the model has a much larger PSD than reanalysis. More specifically, PSD is sloping in the model only for frequencies higher than 0.1 days^{-1} which is about the inverse friction time scale. In contrast to that, the decline of PSD in reanalysis already starts at intermediate frequencies around 0.01 days^{-1} where PSD remains constant in the model. The annual cycle (peaks at (365 days)$^{-1}$) and its higher harmonics are too weak in the model compared to reanalysis.

Visible both in figure (3.13) and (3.14), ensemble averaging reduces power spectral density on almost all time scales. The annual cycle poses an exception. On all other frequencies,

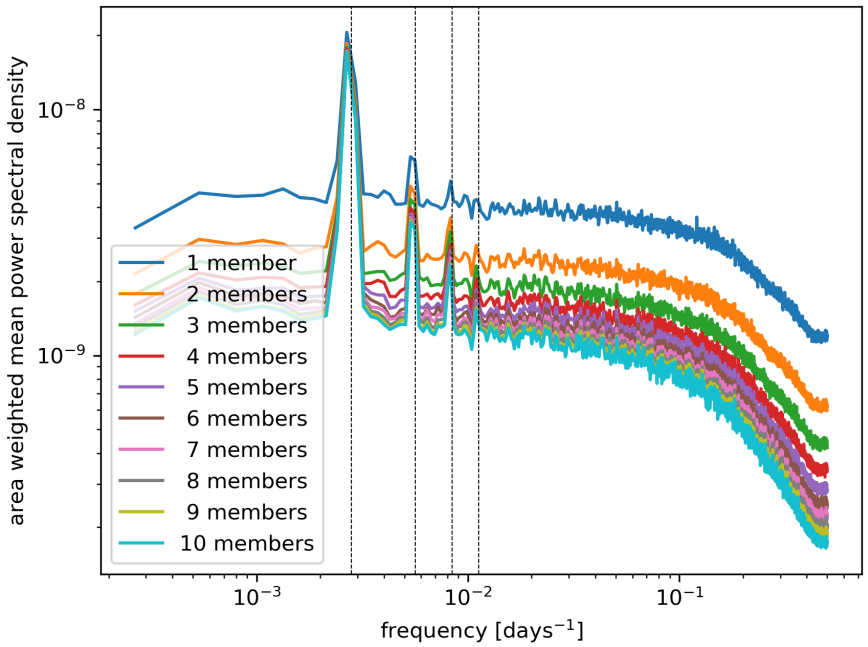

Figure 3.14.: *As fig. (3.13) for the 12-day friction experiment ensemble mean with different ensemble sizes.*

there is a constant factor between the PSD of a single realisation of the model and the PSD of the ensemble mean that increases with increasing ensemble size. Overall, the PSD of the ensemble mean is comparable with reanalysis at high frequencies and too small at low frequencies. Figure (3.14) is also meant to argue in favor of the convergence of the ensemble mean. The spectra for more than 6 members show only slight differences. However, it should be noted that a much larger ensemble size could lead to a further reduction of variance.

The instabilities in the model deteriorate both the time-mean flow and the energy probability distribution of the transients. Next, the model performance regarding the temporal coherence of the transient flow with reanalysis is evaluated. Table (3.2) shows correlation coefficients of area-averaged kinetic energies for different sampling frequencies of the flow. Squared quantities like kinetic energies cannot be expected to be normally distributed. Therefore, the Spearman rank correlation coefficients were calculated instead of the ordinary Pearson's r (see Von Storch and Zwiers (2001) p.149 for reference on these two correlation coefficients). All correlations are highly significant to a 99.9% level, although the estimation of confidence intervals might have suffered from the relatively small sample size at low sampling frequencies.

In Table (3.2), it is visible that the model performance improves for increasing time scales and reaches correlations up to 0.87. At short time scales, the model's e′KE is more strongly correlated with reanalysis than KEzm′, although KEzm′ benefits from using the ensemble mean. Interestingly, the model performs better in terms of KEzm′ for a longer friction time scale and better in terms of e′KE for a shorter friction time scale. Overall, these correlations appear reasonable despite the deteriorated climatology.

Table 3.2.: *Spearman rank correlation coefficients of area-averaged kinetic energy of the transient flow from model experiments with kinetic energies from reanalysis at different sampling frequencies.*

daily means	90N-20N KEzm′	90N-20N e′KE	20N-20S KEzm′	20N-20S e′KE
rws_200hPa_6days_initial1	0.12	0.60	0.17	0.44
rws_200hPa_6days_ensembel_mean	0.36	0.63	0.37	0.58
rws_200hPa_12days_initial1	0.24	0.52	0.25	0.38
rws_200hPa_12days_ensemble_mean	0.61	0.59	0.47	0.49
10-day means	**90N-20N KEzm′**	**90N-20N e′KE**	**20N-20S KEzm′**	**20N-20S e′KE**
rws_200hPa_6days_initial1	0.26	0.44	0.28	0.54
rws_200hPa_6days_ensembel_mean	0.46	0.65	0.43	0.69
rws_200hPa_12days_initial1	0.42	0.31	0.37	0.46
rws_200hPa_12days_ensemble_mean	0.68	0.57	0.53	0.64
30-day means	**90N-20N KEzm′**	**90N-20N e′KE**	**20N-20S KEzm′**	**20N-20S e′KE**
rws_200hPa_6days_initial1	0.43	0.51	0.39	0.63
rws_200hPa_6days_ensembel_mean	0.60	0.73	0.53	0.74
rws_200hPa_12days_initial1	0.56	0.31	0.48	0.50
rws_200hPa_12days_ensemble_mean	0.76	0.65	0.62	0.69
90-day means	**90N-20N KEzm′**	**90N-20N e′KE**	**20N-20S KEzm′**	**20N-20S e′KE**
rws_200hPa_6days_initial1	0.57	0.74	0.64	0.81
rws_200hPa_6days_ensembel_mean	0.70	0.87	0.67	0.85
rws_200hPa_12days_initial1	0.77	0.54	0.63	0.71
rws_200hPa_12days_ensemble_mean	0.83	0.82	0.76	0.79

Model evaluation: regional variability So far, the model has been evaluated by comparing temporal and spatial averages of squared quantities, i.e. kinetic energy. Another important metric is the North Atlantic Oscillation (NAO) index. It contains information for a regional climate and can be expected to be normally distributed.

There are several possibilities to create an NAO index (see e.g. Hurrell and Deser, 2010). One way is to identify principal components of surface pressure or geopotential height. Alternatively, one can use the normalised pressure difference between observation stations, e.g. Lisbon, Portugal and Reykjavik, Iceland. In contrast to the station-based index, the principal component-based NAO index is able to capture the change of the NAO's spatial signature over the year. However, it has to be treated carefully due to the implications of the principle component algorithm (Dommenget and Latif, 2002). Neither of those approaches is applicable to the output of this model for the upper-tropospheric flow because geopotential height is not simulated. Contours of geopotential height and horizontal stream function do not align due to the variable Coriolis parameter. Hence, the first few EOFs of horizontal stream function do not include an NAO-like pattern.

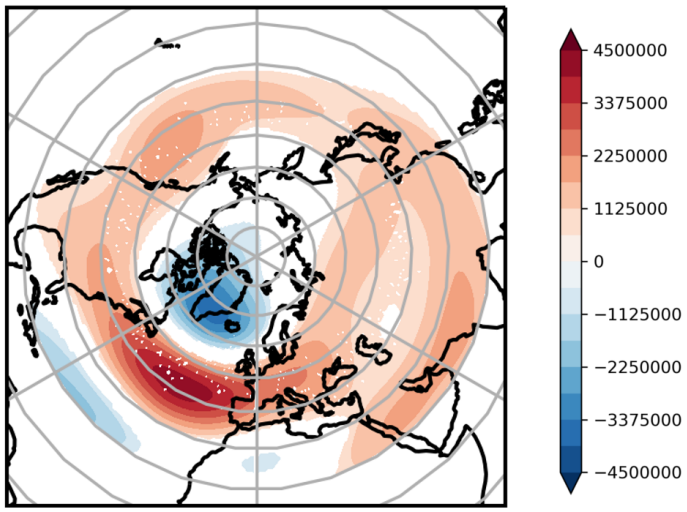

Figure 3.15.: *Monthly DJF 20N-90N stream function at 200hPa from reanalysis regressed on station-based NAO index (masked where not significant at 5% level).*

This issue is solved by defining an NAO pattern based upon regression coefficients of upper tropospheric stream function against a station based NAO index*. More specifically, monthly mean 20N-90N stream function at 200hPa from reanalysis are used and the pattern is masked where correlation is not significant at a 95% confidence level. The associated index is obtained by projecting stream function from the model experiments onto this pattern derived from reanalysis (masked grid points were discarded). Because of the seasonality of the NAO signature and the limitation of the station-based index, the analysis was limited to boreal winter. The resulting regression pattern is shown in figure (3.15). It reveals a dipole over the Atlantic associated with a westerly flow anomaly between Canada and northern Europe or a meridional shift of the westerly jet. The NAO pattern does project onto the zonal mean but it is dominated by the North Atlantic sector which varies independently from the Pacific, in reanalysis at least (Deser, 2000). So in contrast to zonal-mean kinetic energies, the NAO can be regarded as an index for a regional climate.

The distributions of the NAO indices from the model shown in figure (3.16) compare well with reanalysis. Small differences in variance occur depending on the friction time scale and ensemble size. In figure (3.16), the distributions of and index are plotted that is produced by the projection of 10-day mean stream function. But the general picture is constant across time scales. The comparable variance of the NAO index goes along with a similar amount of explained variance by the NAO in the model and in reanalysis. However, model and reanalysis are uncorrelated from daily to seasonal time scales in terms of the NAO index. It is a serious deficiency of the model. Perhaps, this could be improved with a much larger ensemble size. Clearly, the ten-member ensemble used in this study cannot isolate a significant signal which is forced by a RWS anomaly.

*Hurrell, James & National Center for Atmospheric Research Staff (Eds). Last modified 09 Jan 2020. "The Climate Data Guide: Hurrell North Atlantic Oscillation (NAO) Index (station-based)." Retrieved from `https://climatedataguide.ucar.edu/climate-data/hurrell-north-atlantic-oscillation-nao-index-station-based`.

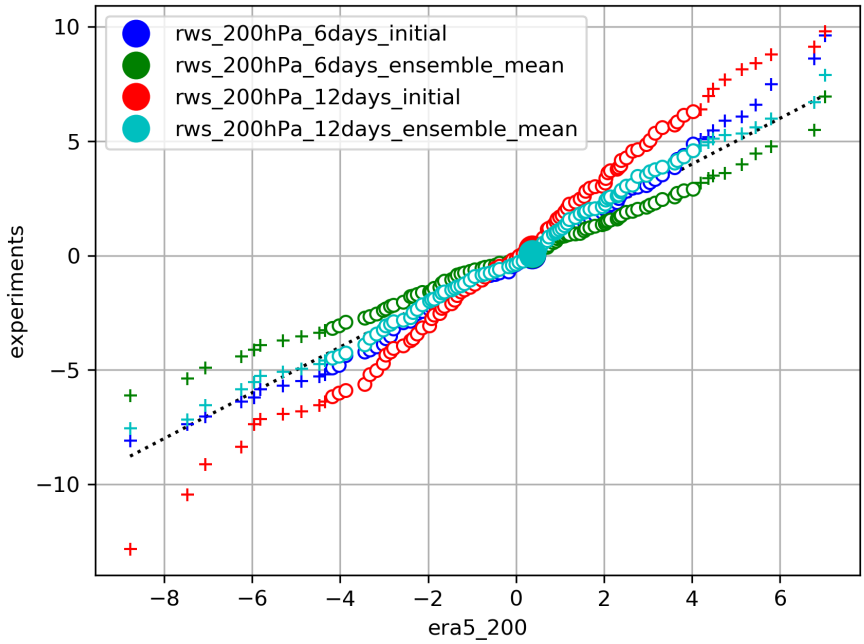

Figure 3.16.: *Percentiles of 10-day mean DJF NAO index from model experiments plotted against the percentiles from reanalysis (the solid circle indicates the median, crosses indicate the <10% and >90% extremes, the main diagonal is dashed).*

Overall, the model performs very differently in terms of regional flow anomalies, like the NAO, compared to domain averaged kinetic energies. The model has some limitations reproducing the probability distribution of kinetic energies seen in reanalysis. In contrast to that, the probability distribution of a regional flow anomaly like the NAO is well simulated. More interesting than simply comparing probability distributions is to evaluate temporal coherence. In the global perspective, there is a reasonable coherence seen in the correlations of zonally averaged kinetic energies with reanalysis. A temporal coherence of a regional climate index, on the other hand, is nonexistent, despite the well-simulated distribution of the index. That can be seen as an expression of a spatial incoherence of the transients between model and reanalysis. Apparently, the same spatial incoherence exists between individual ensemble members, as ensemble averaging reduces variance dramatically. One can speculate that this is due to the deteriorated basic or mean flow in the model and consequently an erroneous wave propagation or advection of anomalies across the globe.

4. The baroclinic governor in a simple model

The motivation for the use of a barotropic model is discussed in chapter (1). Specifically, a barotropic model is expected to simulate the essential processes controling eddy-driven jet dynamics and, therefore, to capture extratropical low-frequency variability which is essentially barotropic (Vallis et al., 2004; Baxter and Nigam, 2013). Also, it is noted that in early modelling studies the upper-tropospheric extratropical response to thermal and orographic forcing is produced by barotropic Rossby waves, and baroclinic Rossby waves are of minor importance (Hoskins and Karoly, 1981). In other words, wavelengths can be considered small compared to the radius of deformation. However, this thesis reveals the limitations of the restriction to a purely barotropic flow. The climate in a barotropic model is shaped by barotropic instabilities that appear to be suppressed in a baroclinic world.

On the other hand, there is a long known interaction between a barotropic and baroclinic shear: the barotropic-governor. James and Gray (1986) find that reducing surface drag and permitting stronger barotropic shear suppresses baroclinic instability in numerical experiments. Simmons and Hoskins (1980) show that a barotropic jet modifies the nonlinear life cycle of a baroclinic jet. The name of a barotropic governor was developed by James (1987) who finds that a small barotropic shear reduces normal mode growth rates in a two-layer quasi-geostrophic model. Mak (2011)[Ch. 8C.2] extends this idea investigating the effect of a small baroclinic shear on barotropic instability and referring to it as a baroclinic governor.

This study adds relevance to the idea of a baroclinic governor. In the following, it will be evaluated to what extent the model results in this thesis can be explained with the simplified approach by Mak (2011). First, the model will be introduced by demonstrating the effect of a small barotropic shear on baroclinic instability. This methodology will then be adapted to analyse the effect of a small baroclinic shear on barotropic instability. The governing equations for potential vorticity perturbations q'_j in the two-layer quasi-geostrophic model linearized around a zonally symmetric basic state are

$$q'_{1t} + U_1 q'_{1x} + \psi'_{1x}\bar{q}_{1y} = 0 \tag{4.1a}$$
$$q'_{3t} + U_3 q'_{3x} + \psi'_{3x}\bar{q}_{3y} = 0 \tag{4.1b}$$

with

$$q'_1 = \nabla^2\psi'_1 - \lambda^2(\psi'_1 - \psi'_3) \tag{4.2a}$$
$$q'_3 = \nabla^2\psi'_3 - \lambda^2(\psi'_3 - \psi'_1) \tag{4.2b}$$

The corresponding gradients of the basic state potential vorticity $\bar{q}_j$ are

$$\bar{q}_{1y} = \beta - U_{1yy} + \lambda^2(U_1 - U_3) \tag{4.3a}$$
$$\bar{q}_{3y} = \beta - U_{3yy} + \lambda^2(U_3 - U_1) \tag{4.3b}$$

where U_j denotes the basic flow, ψ_j' the stream function perturbations, λ^{-1} the Rossby radius of deformation, and β the meridional gradient of planetary vorticity. Normal mode solutions to this model in a reentrant channel bounded by two rigid walls ($-\infty < x < \infty, -Y \leq y \leq Y$) have the form of

$$\psi_j' = \xi_j(y) e^{i(kx - \sigma t)} \tag{4.4}$$

In that ansatz, $\sigma, \xi_j(y) \in \mathbb{C}$. The real part $\Re(\sigma)$ takes the form an angular frequency for an oscillatory behaviour. For a non-zero imaginary part $\Im(\sigma)$, the normal mode is either growing or decaying. The amplitude function $\xi_j(y)$ determines the meridional structure and a zonal phase shift of the solution. Its boundary conditions are $\xi_j(\pm Y) = 0$. This ansatz is inserted into equations (4.1) and (4.2) to obtain the following non-dimensional differential equations that govern $\xi_j(y)$:

$$\widetilde{\sigma}\left[\left(\frac{\partial^2}{\partial \widetilde{y}^2} - \widetilde{k}^2 - 1\right)\xi_1 + \xi_3\right] = \widetilde{k}\widetilde{U}_1\left[\left(\frac{\partial^2}{\partial \widetilde{y}^2} - \widetilde{k}^2 - 1\right)\xi_1 + \xi_3\right] + \widetilde{k}\xi_1\left[\widetilde{\beta} - \widetilde{U}_{1\tilde{y}\tilde{y}} + \widetilde{U}_1 - \widetilde{U}_3\right] \tag{4.5a}$$

$$\widetilde{\sigma}\left[\left(\frac{\partial^2}{\partial \widetilde{y}^2} - \widetilde{k}^2 - 1\right)\xi_3 + \xi_1\right] = \widetilde{k}\widetilde{U}_3\left[\left(\frac{\partial^2}{\partial \widetilde{y}^2} - \widetilde{k}^2 - 1\right)\xi_3 + \xi_1\right] + \widetilde{k}\xi_3\left[\widetilde{\beta} - \widetilde{U}_{3\tilde{y}\tilde{y}} + \widetilde{U}_3 - \widetilde{U}_1\right] \tag{4.5b}$$

In these equations, horizontal distance is measured in units of λ^{-1}, velocity in units of V, and time in units of $(V\lambda)^{-1}$. So the non-dimensional quantities are $\tilde{k} = k/\lambda$, $\tilde{\sigma} = \sigma/(V\lambda)$, $\tilde{\beta} = \beta/(V\lambda^2)$, $\tilde{U}_j = U_j/V$, and $(\tilde{x}, \tilde{y}, \tilde{a}) = \lambda(x, y, a)$. The equations with dimensional quantities are given by Mak (2011)[Ch. 8C.2] and reprinted in the appendix (A). The non-dimensional equations (4.5) are discretised in the meridional direction on $N = 99$ grid points by using centred differences for the derivatives. They can then be expressed as a matrix equation, where $\vec{F}$ is a 2N vector containing ξ_1, ξ_3 and $\underline{A}$, $\underline{B}$ are 2N x 2N matrices (see appedix A for details).

$$\widetilde{\sigma}\underline{B}\vec{F} = \underline{A}\vec{F} \tag{4.6}$$

The non-dimensional growth rates and frequency of the normal mode solutions ($\Im(\tilde{\sigma})$ and $\Re(\tilde{\sigma})$) can be found by calculating the eigenvalues of $\underline{B}^{-1}\underline{A}$. The spatial structure of these solutions is given by the eigenvectors of $\underline{B}^{-1}\underline{A}$ for the amplitude function $\xi_j(\tilde{y})$. The specific solutions to this eigenvalue problem are determined by the choice of parameters and the basic state wind profile. Mak (2011) uses a 8000km wide domain, $\lambda = 10^{-6}\mathrm{m}^{-1}$, $V = 30\mathrm{m/s}$ and $\beta = 1.5 \times 10^{-11}\mathrm{m}^{-1}\mathrm{s}^{-1}$ (corresponds to 49°N). His wind profiles (4.7) consist of a meridionally independent baroclinic component and a vertically independent Gaussian jet

$$U_1 = V\left(u_{1o} + \epsilon \exp\left(-(y/a)^2\right)\right) \tag{4.7a}$$

$$U_3 = V\left(u_{3o} + \epsilon \exp\left(-(y/a)^2\right)\right) \tag{4.7b}$$

This setup with a foremost baroclinic jet ($u_{1o} = 1.0$, $u_{3o} = 0.2$) and a weak, broad barotropic component ($\epsilon = 0.7$, $\tilde{a} = 1.5$) is used by Mak (2011) to demonstrate the barotropic governor.

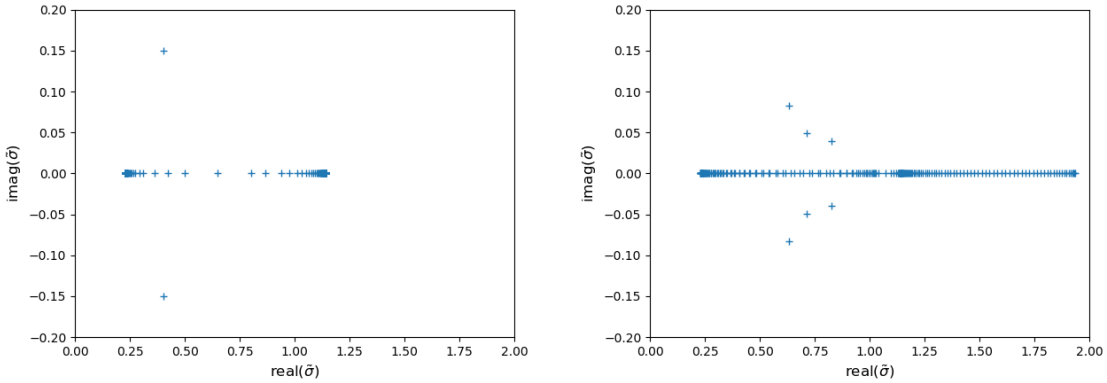

(a) *Baroclinic shear* **(b)** *Baroclinic shear + small barotropic shear*

Figure 4.1.: *Distribution of eigenvalues in the complex plane for two different basic state wind profiles ($u_{1o} = 1$, $u_{3o} = 0.2$, $\tilde{a} = 1.5$, $\epsilon = 0$ or 0.7) at wavelength 5.5 (non-dimensional).*

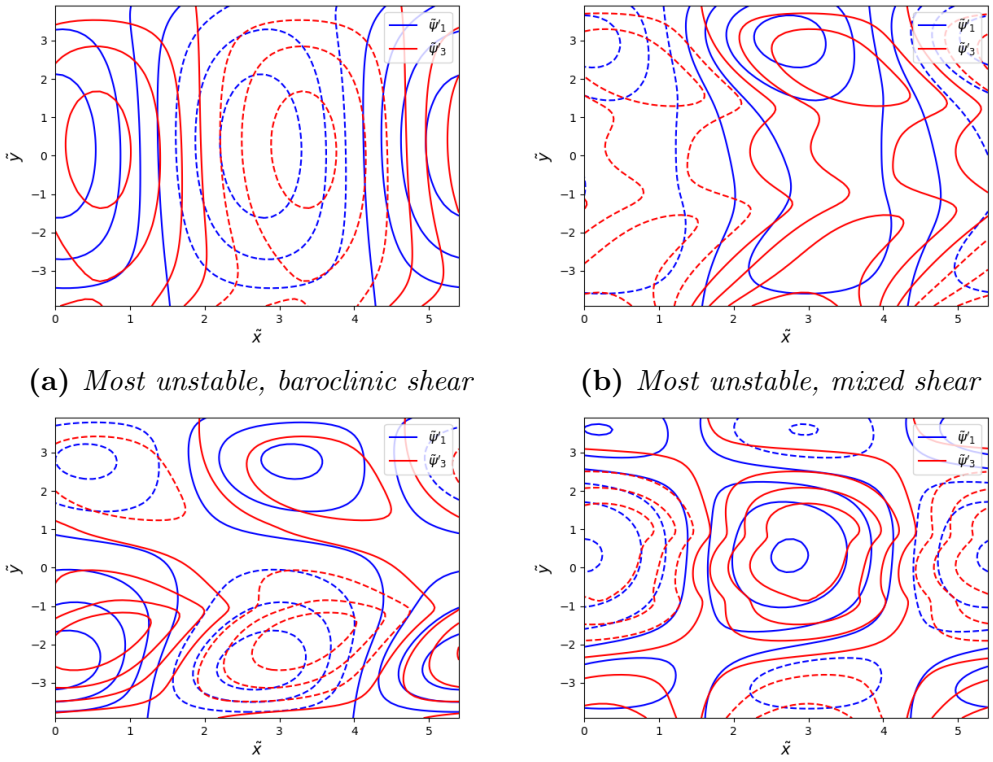

(a) *Most unstable, baroclinic shear* **(b)** *Most unstable, mixed shear*

(c) *2nd most unstable, mixed shear* **(d)** *3rd most unstable, mixed shear*

Figure 4.2.: *Streamfunction ψ'_1 & ψ'_3 of the unstable normal modes for two different basic state wind profiles (level with higher velocity in blue; $u_{1o} = 1$, $u_{3o} = 0.2$, $\tilde{a} = 1.5$, $\epsilon = 0$ or 0.7) at wavelength 5.5 with arbitrary contour spacing (non-dimensional).*

Growth rate, frequency, and spatial structure of the normal modes also depend on non-dimensional zonal wavelength ($2\pi\tilde{k}^{-1}$) of the disturbance in addition to the basic state. Mak (2011) chooses 5.5. His results are reproduced and plotted in figure (4.1). The non-dimensional eigenvalues are shown in the complex plane with growth rates ($\Im(\tilde{\sigma})$) and frequencies ($\Re(\tilde{\sigma})$) in units of $V\lambda$. Most of the eigenvalues have no imaginary part. These correspond to so-called continuum modes with discontinuities in their spatial structure, spanning the space of any arbitrary disturbances (Mak, 2011, Ch. 8B.2.2). In contrast to the continuum modes, the number of the true or discrete normal modes with a non-zero imaginary part does not depend on model resolution, i.e the number of meridional grid points. The discrete normal modes always come in pairs, one is growing and one is damped. The spatial structure of the unstable modes for the barotropic governor are shown in figure (4.2).

For the flow with pure baroclinic shear (Fig. 4.1a), there is a single unstable normal mode with an e-folding scale of 2.5 days, a period of 6 days, and a half-cosine meridional structure. The growing mode's phase is tilted vertically backwards as it is necessary to grow by baroclinic instability (Fig. 4.2a). When a small barotropic shear is added (Fig. 4.1b) the growth rate is reduced to an e-folding scale of 4.8 days, the frequency is increased to a period of 3.8 days, and the half-cosine meridional structure is disturbed, being split into a northern and a southern maximum (Fig. 4.2b). In addition to that, two new unstable modes develop with higher meridional wavenumbers, higher frequencies, but lower growth rates (Fig. 4.2c,d). James (1987) concludes that the distortion of a baroclinically unstable normal mode by a horizontal shear reduces its ability to extract potential energy from the background state.

There are two important dynamical mechanisms for the growth of atmospheric disturbances: baroclinic and barotropic instability. These mechanisms conserve pseudomomentum or wave-activity density, respectively (Mak, 2011, Ch. 8.B). From these conservation laws, one can derive a necessary condition for instability: The basic potential vorticity gradient (4.3) has to change its sign within the domain. In other words, the stabilising beta-effect has to be overcome by either baroclinic shear, barotropic shear, or the sum of both. Figure (4.3) shows non-dimensional growth rates and zonal phase velocities ($\tilde{\sigma}/\tilde{k}$) for several combinations of baroclinic and barotropic shear. As in figure (4.1), a broad Gaussian jet ($\tilde{a} = 1.5$) and a non-dimensional wavelength of 5.5 are used. The largest growth rates are reached for strong baroclinic shear without any barotropic shear (Fig. 4.3a). Growth rates decrease when either the baroclinic shear is reduced or a small barotropic shear is introduced by increasing the amplitude ϵ of the Gaussian jet. Increasing the barotropic shear leads to a minimum in growth rates for intermediate values, followed by an increase in growth rates due to barotropic instability. Interestingly, for a large baroclinic shear, the minimum growth rate is at a higher barotropic shear than for an intermediate baroclinic shear. The zonal phase speed of the most unstable mode increases for higher barotropic and lower baroclinic shear (Fig. 4.3b).

The setup used in figure (4.3) does not show a significant baroclinic governor, i.e. no reduction of growth rate when a small baroclinic shear is added to a barotropic jet. However, the properties of the normal modes depend on zonal wavelength and the width of the Gaussian jet. These parameters are varied in figure (4.4). The wavelength-dependent behaviour of the barotropic governor is depicted in figure (4.4a): With a small barotropic shear the max-

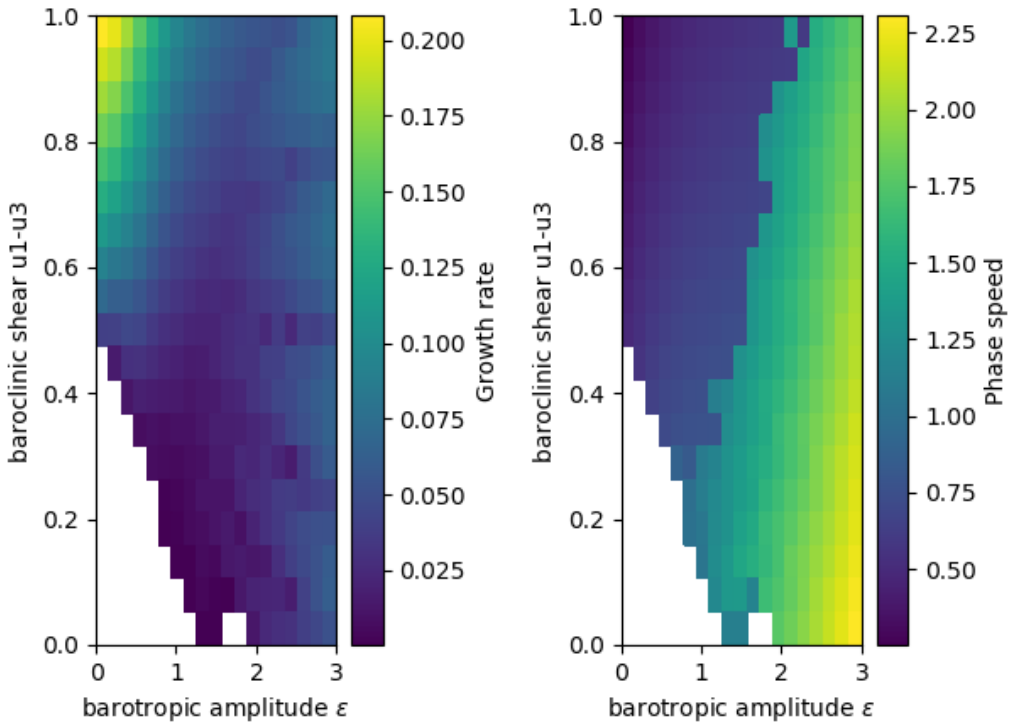

Figure 4.3.: *Nondimensional growth rates and phase velocities for the most unstable mode at a non-dimensional wavelength of 5.5 with a broad Gaussian jet ($u_{1o} = 1.0$, $\tilde{a} = 1.5$) of different amplitudes.*

imum growth rates are shifted to a higher wavelength (orange line) compared to a purely baroclinic shear (green line). The zonal phase speeds show a linear decrease for increasing wavelength, although, there are interesting discontinuities. These correspond to changes of the most unstable mode. A plot similar to figure (4.4a) is shown by Mak (2011, Fig. 8C.2), not for the most unstable mode but for the mode with the broadest meridional extent. That mode has a long-wave cutoff, meaning it becomes stable for longer wavelenths. Figure (4.4a) illustrates that for higher wavelengths other modes with a different meridional structure and a higher frequency grow more unstable. Furthermore, figure (4.4a) depicts a Doppler effect: The zonal phase speed of the most unstable mode increases (green line compared to blue line) without altering the growth rate when a uniform velocity is added to the flow (blue line exactly underneath green line in left subplot).

In figure (4.4b), purely barotropic jets of different widths are compared. First, the width of the Gaussian jet with a given amplitude ϵ influences the maximum barotropic shear and therefore the maximum growth rates. This can be compensated by modifying ϵ. Second, there is a shift in the wavelength for the maximum growth rate and the short-wave cutoff. A narrower jet (green line) is barotropically unstable at shorter zonal wavelengths. Zonal phase speeds do not provide additional insight and, hence, are not shown here.

Mak (2011) uses a wind profile with a Gaussian jet of intermediate width ($u_{1o} = 0.2$, $u_{3o} = 0.1$, $\epsilon = 1.0$, $\tilde{a} = 0.75$) to demonstrate the baroclinic governor. The reduction in

growth rate, however, is only slight (analysed at a wavelength equal to 4). Here, it is found to be more convincing for a very narrow jet. With the influence of jet width already discussed, this question is particularly relevant since the instantaneous jet is probably more narrow than the climatological one. For a very narrow jet and non-dimensional wavelengths between 4-8, the growth rates of the most unstable mode are reduced significantly when a small baroclinic shear is added to the barotropic jet (see Fig. 4.4c; blue line is the purely barotropic jet). The fastest growing modes with a jet like this, however, are found at a short wavelength equal to 2.5 where the mitigation of growth rates is much weaker. In other words, this two-layer QG-model does point towards the existence of a baroclinic governor but it is not fully convincing since instabilities usually take the dimensions of the fastest growing modes.

The picture might become more convincing for a different set of parameters. In addition to wavelength, baroclinic shear, width and amplitude of the barotropic jet, there is the deformation radius λ^{-1} to be tuned. In fact, the size of the deformation radius could be quite influential, weighting the contribution of barotropic and baroclinic shear to the basic state potential vorticity gradient (4.3). This pins down to the question of which vertical mode is responsible for the baroclinic governor of barotropic instability? Possibly, it differs from that mode which is subject to baroclinic instability causing the RWS for the upper-tropospheric flow. At this stage, no further tuning of the addressed parameters will be attempted since the answer to this question requires further analysis and modelling.

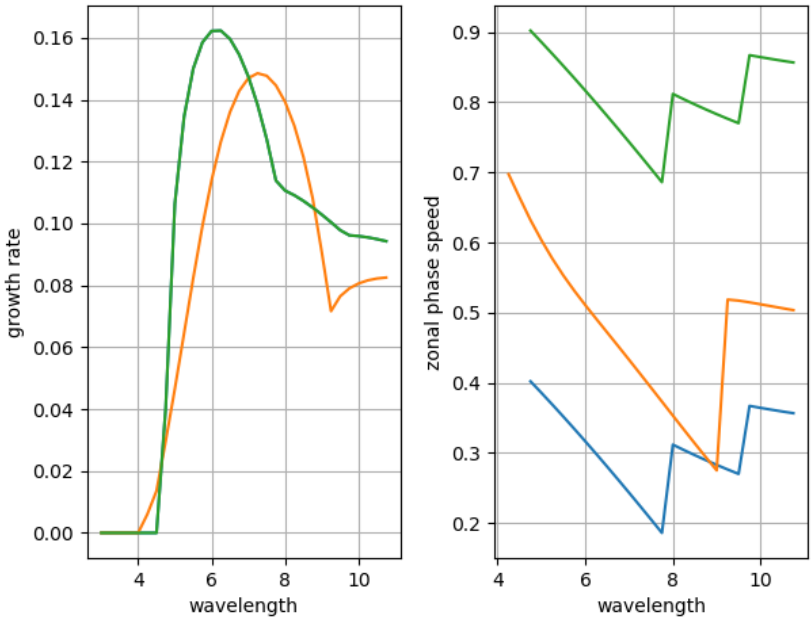

(a) *Barotropic governor (blue line* $u_{1o} = 1.0$, $u_{3o} = 0.2$, $\epsilon = 0.0$, $\tilde{a} = 1.5$*; orange line* $u_{1o} = 1.0$, $u_{3o} = 0.2$, $\epsilon = 0.7$, $\tilde{a} = 1.5$*; and green line* $u_{1o} = 1.5$, $u_{3o} = 0.7$, $\epsilon = 0.0$, $\tilde{a} = 1.5$*)*

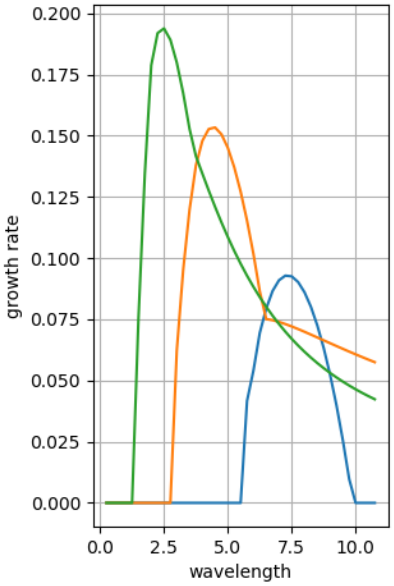

(b) *Barotropic instability with different jet width (blue line* $u_{1o} = 0.0$, $u_{3o} = 0.0$, $\epsilon = 2.0$, $\tilde{a} = 1.5$*; orange line* $u_{1o} = 0.0$, $u_{3o} = 0.0$, $\epsilon = 1.0$, $\tilde{a} = 0.8$*; and green line* $u_{1o} = 0.0$, $u_{3o} = 0.0$, $\epsilon = 0.5$, $\tilde{a} = 0.4$*)*

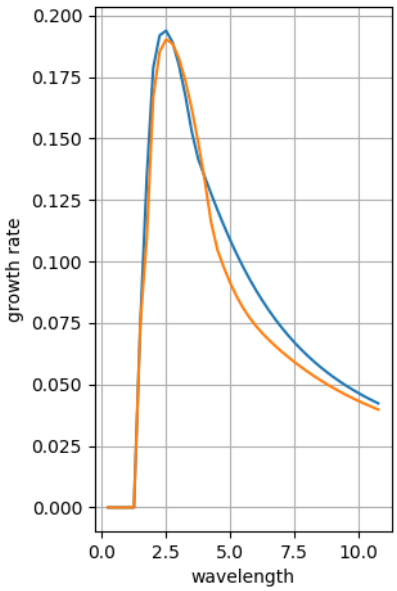

(c) *Baroclinic governor for very narrow jet (blue line* $u_{1o} = 0.0$, $u_{3o} = 0.0$, $\epsilon = 0.5$, $\tilde{a} = 0.4$*; and orange line* $u_{1o} = 0.1$, $u_{3o} = 0.2$, $\epsilon = 0.5$, $\tilde{a} = 0.4$*)*

Figure 4.4.: *Growth rates and phase velocities of the most unstable mode plotted against wavelength for different wind profiles with parameters given for equations (4.7).*

5. A more complete Rossby wave source

5.1. Importance of vertical momentum advection

A prominent result of chapter (3.2) is the spurious easterly wind at the equator, too strong by a factor of ten as visible for example in figure (3.10). Apparently, the barotropic model driven by upper-tropospheric Rossby wave source (RWS) misses an essential part of the equatorial dynamics to balance these easterlies. Usually, the equatorial momentum equations are discussed in flux form. Lee (1999), for example, analyses the various contributions to the zonal-mean zonal momentum convergence in renalysis (see Ch. 1.2 for details). Hoskins et al. (1999) perform an idealised modelling study and find a balance in the zonal-mean zonal momentum equation between a Hadley cell term and the non-linear momentum flux convergence associated with pertubations. However, in the barotropic framework, with RWS defined by Sardeshmukh and Hoskins (1988), the momentum equations cannot be written in flux form because they allow horizontal divergence but neglect vertical advection. This is inconsistent with the continuity equation.

In the following, the effect of that inconsistency on the zonal-mean zonal momentum equation is discussed. In order to do so, it is made use of the continuity equation, that is

$$u_{\chi,x} + v_{\chi,y} + \omega_p = 0 \tag{5.1}$$

, the product rule of differentiation, and of a couple of identities

$$u_{\psi,x} = -v_{\psi,y} \tag{5.2a}$$
$$u_{\chi,y} = v_{\chi,x} \tag{5.2b}$$
$$[v_\psi] = 0 \tag{5.2c}$$
$$[u_\chi] = 0 \tag{5.2d}$$
$$[(\quad)_x] = 0 \tag{5.2e}$$
$$[uu_x] = \tfrac{1}{2}[(u^2)_x] = 0 \tag{5.2f}$$

where brackets [ ] denote a zonal mean and subscript χ and ψ indicate irrotational and nondivergent velocity components. Note that the continuity equation is written pressure coordinates with the vertical velocity $\omega = Dp/Dt$. An important consequence of these identities is the disappearance of the meridional advection of zonal momentum by the irrotational flow a the zonal-mean perspective:

$$[v_\chi u_{\chi,y}] = [v_\chi v_{\chi,x}] = 0 \tag{5.3}$$

where first equal sign uses (5.2b) and the second (5.2f). Using equation (5.3), it follows that

without vertical momentum advection the zonal-mean zonal momentum equation is

$$[u_t] = -[uu_x] - [vu_y] + f[v] \tag{5.4a}$$
$$= -[v_\psi u_{\psi,y}] - [v_\psi u_{\chi,y}] - [v_\chi u_{\psi,y}] + f[v_\chi] \tag{5.4b}$$
$$= -[v_\psi u_\psi]_y - [v_\psi u_\chi]_y - [v_\chi u_\psi]_y - [\omega_p u_\psi] + f[v_\chi] \tag{5.4c}$$

Equation (5.4c) is the attempt to write the zonal-mean zonal momentum equation in flux form. It shows that horizontal momentum flux convergence and horizontal momentum advection are connected by $-[\omega_p u_\psi]$ which is a part of the vertical momentum flux convergence. For the detailed transformation between (5.4b) and (5.4c), refer to appendix (A). Interestingly, equation (5.4c) does not include products of irrotational velocities. In order to consider also the effect of $-[u_\chi v_\chi]_y$, one has to include vertical advection into the horizontal momentum equations:

$$u_t + uu_x + vu_y + \omega u_p - fv = -\Phi_x \tag{5.5a}$$
$$v_t + uv_x + vv_y + \omega v_p + fu = -\Phi_y \tag{5.5b}$$

These equations can easily be written in flux form by combining them with the continuity equation. The zonal-mean zonal momentum equation becomes

$$[u_t] = -[uu_x] - [vu_y] - [\omega u_p] + f[v] \tag{5.6a}$$
$$= -[v_\psi u_{\psi,y}] - [v_\psi u_{\chi,y}] - [v_\chi u_{\psi,y}] - [\omega u_p] + f[v_\chi] \tag{5.6b}$$
$$= -[v_\psi u_\psi]_y - [v_\psi u_\chi]_y - [v_\chi u_\psi]_y - [v_\chi u_\chi]_y - [\omega u]_p + f[v_\chi] \tag{5.6c}$$

Note that the equations (5.6) are written in a way to match the equations (5.4). Obviously, these expressions are more complete since they include zonal-mean vertical momentum advection or vertical momentum flux convergence, respectively. The flux form (5.6c) is obtained from (5.6b) by adding the continuity equation (5.1) as shown in appendix (A). By subtracting (5.4c) from (5.6c), one can see that the zonal-mean vertical momentum advection equals the missing contribution to the vertical momentum flux convergence and also, perhaps more importantly, the horizontal momentum flux convergence due to divergent velocities $-[v_\chi u_\chi]_y$ (see appendix (A) for details).

$$-[\omega u_p] \tag{5.7a}$$
$$= -[\omega u_{\psi,p}] - [\omega u_{\chi,p}] \tag{5.7b}$$
$$= -[\omega u_{\psi,p}] - [\omega u_\chi]_p - [v_\chi u_\chi]_y \tag{5.7c}$$

Zonal-mean zonal momentum in reanalysis To illustrate the relative importance of vertical momentum advection, in particular at the equator, the various terms of the zonal-mean zonal momentum equation (5.6b) are diagnosed from reanalysis. Figure (5.1) shows vertical sections of the temporal mean quantities. It is confirmed that in the Eulerian mean, Coriolis force and horizontal advection almost cancel each other (Held and Hou, 1980). However, these terms (Fig. 5.1b,c,d) do not balance at the equator since they are both either close to zero or negative. A positive acceleration at the equator is given by vertical advection (Fig. 5.1a). It peaks around 1.2 m/s^2 at 200 hPa. In the extratropics it is small, however, it can

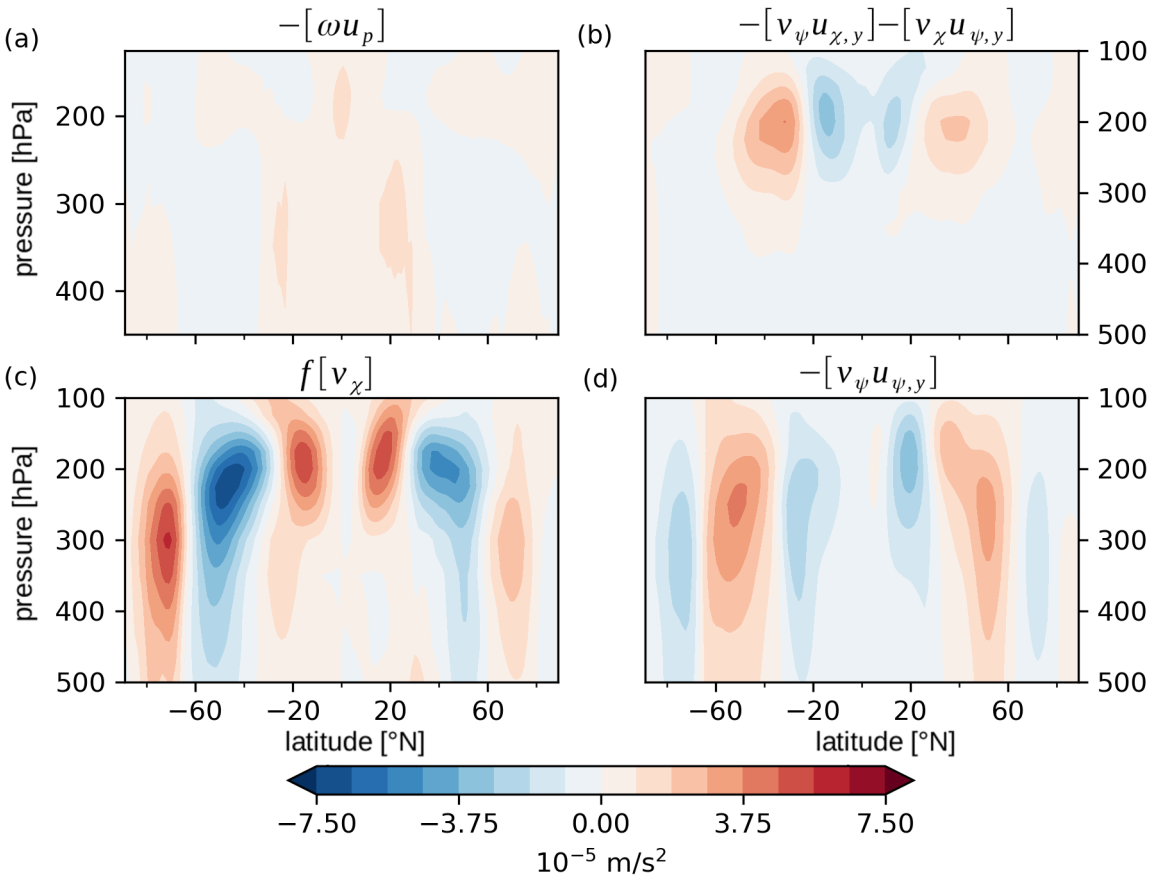

Figure 5.1.: *Temporal mean of the respective terms in the zonal-mean zonal momentum equation (5.6b) computed from daily mean reanalysis data. Note that $-[v_\psi u_{\psi,y}]$ can be simulated by a barotropic model, the other terms have to be specified as forcing.*

still be significant given the close balance of the larger terms. Note that locally, the zonal-mean vertical momentum advection could be larger than shown by figure (5.1a) since the reanalysis data has been interpolated vertically from model coordinates to pressure levels and vertical gradients are calculated using centred differences (see Ch. 2.3).

It is interesting to see that the advection by rotational velocities (Fig. 5.1d) is rather barotropic. In contrast to that, the advection by mixed products (Fig. 5.1b) and vertical velocity (Fig. 5.1a) shows a strong baroclinic nature. Mixed advection and tropical Coriolis force maximise at 200 hPa whereas Coriolis force at higher latitudes has its highest values at lower levels. The latitude of the strongest acceleration due to vertical advection above 250hPa is the equator. Below 250hPa, the maximum is found around 20° N/S at the descending branches of the Hadley cell.

A vorticity equation model explicitly simulates the advection of momentum due to products of nondivergent velocities. Both Coriolis force and the horizontal advection by mixed products of nondivergent and irrotational velocities contribute to the traditional RWS defined by Sardeshmukh and Hoskins (1988). The advection of momentum by the vertical flow is

neither simulated by the model velocities nor included in the traditional RWS. However, figure (5.1) suggests that it should be included in the forcing of a barotropic model for the upper tropospheric flow since it can accelerate the flow along the equator and cure the easterly bias of the barotropic model in this study.

5.2. Curl of vertical momentum advection

In the section above, it is shown that a part of the horizonal momentum flux convergence ($[u_\chi v_\chi]_y$) is missing in the zonal-mean zonal momentum equation when vertical advection is neglected. This is not surprising, after all, because the traditional RWS does not include products of divergent velocities. To obtain the corrected Rossby wave source for the upper troposphere, one has to compute the curl of the horizontal momentum equations that include vertical advection (eq. 5.5),

$$\zeta_t + \vec{u_\psi} \cdot \nabla_h(\zeta + f) = RWS_h - \omega\zeta_p - \omega_x v_p + \omega_y u_p \tag{5.8a}$$

$$RWS_h = -(\nabla_h \cdot \vec{u_\chi})(\zeta + f) - \vec{u_\chi} \cdot \nabla_h(\zeta + f) \tag{5.8b}$$

$$\nabla_h = (\tfrac{\partial}{\partial x}, \tfrac{\partial}{\partial y}, 0) \tag{5.8c}$$

In addition to the Sardeshmukh and Hoskins (1988) expression, given by $\mathrm{RWS_h}$, this RWS contains the curl of the vertical momentum advection:

$$\text{vert\_forcing} = -\omega\zeta_p - \omega_x v_p + \omega_y u_p \tag{5.9}$$

The new vertical vorticity forcing term consists of vertical vorticity advection ($-\omega\zeta_p$), and zonal ($-\omega_x v_p$) and meridional vortex tilting ($\omega_y u_p$). The seasonal means of these three contributions, calculated with daily means from reanalysis for DJF and JJA at 200hPa, are plotted in figure (5.2). As for figures (3.1, 3.2, 3.4), these fields were smoothed to a spectral resolution of T42 for the purpose of plotting to remove extreme small scale peaks. Vertical vorticity advection and meridional vortex tilting exhibit a strong seasonal cycle. In boreal summer, strong positive vertical vorticity advection can be found north to the Maritime Continent at the equatorward flank of the jet and over India. In boreal winter, the vertical vorticity advection has no such pronounced maximum but it tends to be negative in the tropics and subtropics. Zonal vortex tilting has a weaker seasonal cycle. It is distributed relatively uniformly across the globe with negative values in the northern and positive values in the southern hemisphere. In many places, there is a close balance between vertical vorticity advection and zonal vortex tilting. Meridional vortex tilting forms a dipole around the equator with positive vorticity forcing in the northern and negative forcing in the southern hemisphere. That would drive equatorial westerlies. It is strongest in boreal summer over the western Indian ocean. The small scale peaks removed by the smoothing to T42 occur most strongly for the vertical vorticity advection at mountain ranges and throughout the year.

The annual mean sum of the three contributions to the curl of vertical momentum advection is plotted for 200hPa and 300hPa in figure (5.3) together with its variance of daily means. Obviously, there is a strong cancellation between the different contributions to the curl of vertical momentum advection. At 200hPa, the main remnants are a dipole, caused

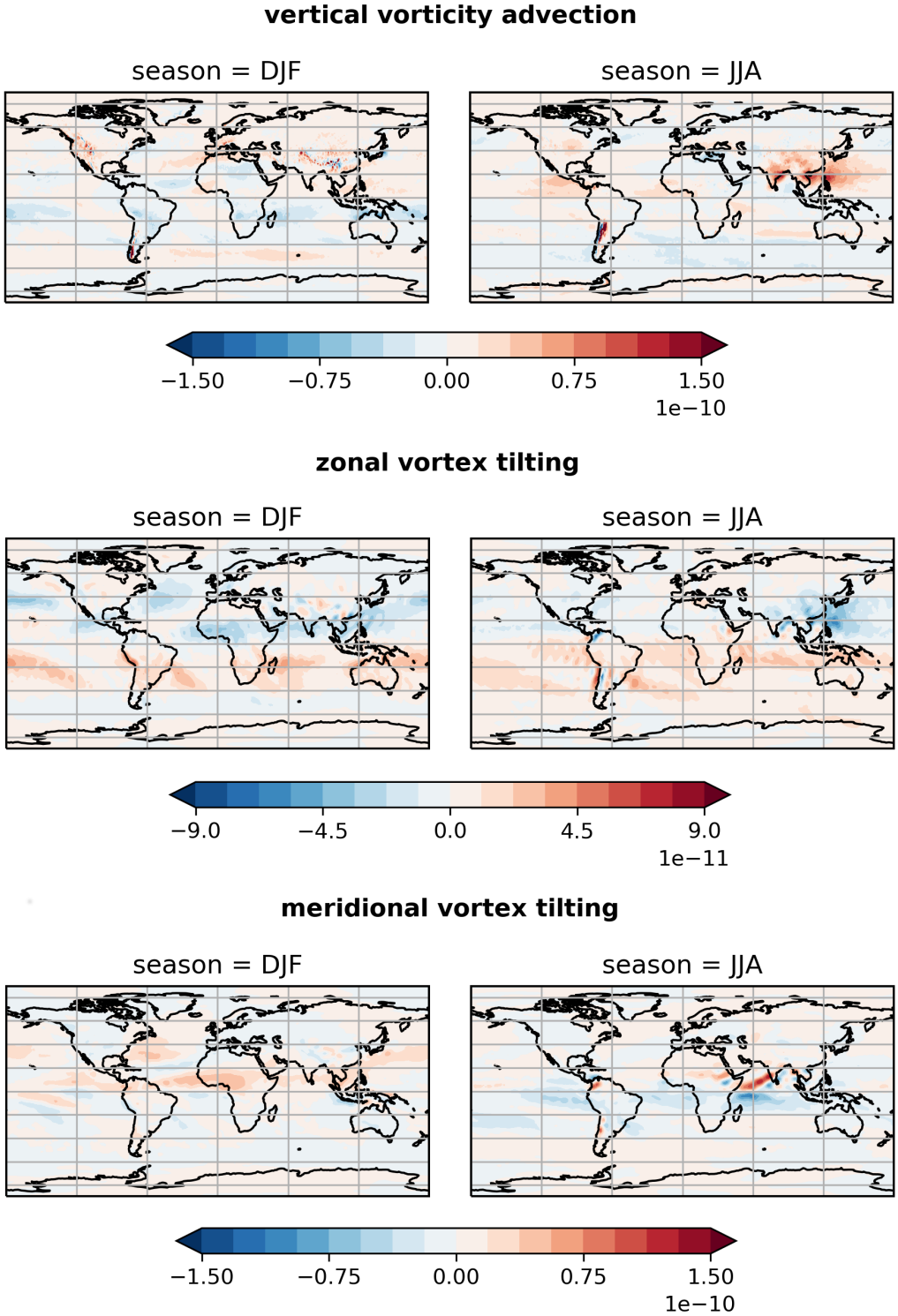

Figure 5.2.: *Seasonal means of vertical vorticity advection* $[s^{-2}]$*, zonal vortex tilting* $(-\omega_x v_p)$ $[s^{-2}]$*, and meridional vortex tilting* $(\omega_y u_p)$ $[s^{-2}]$ *for summer and winter at 200hPa from reanalysis smoothed to T42 for the purpose of plotting.*

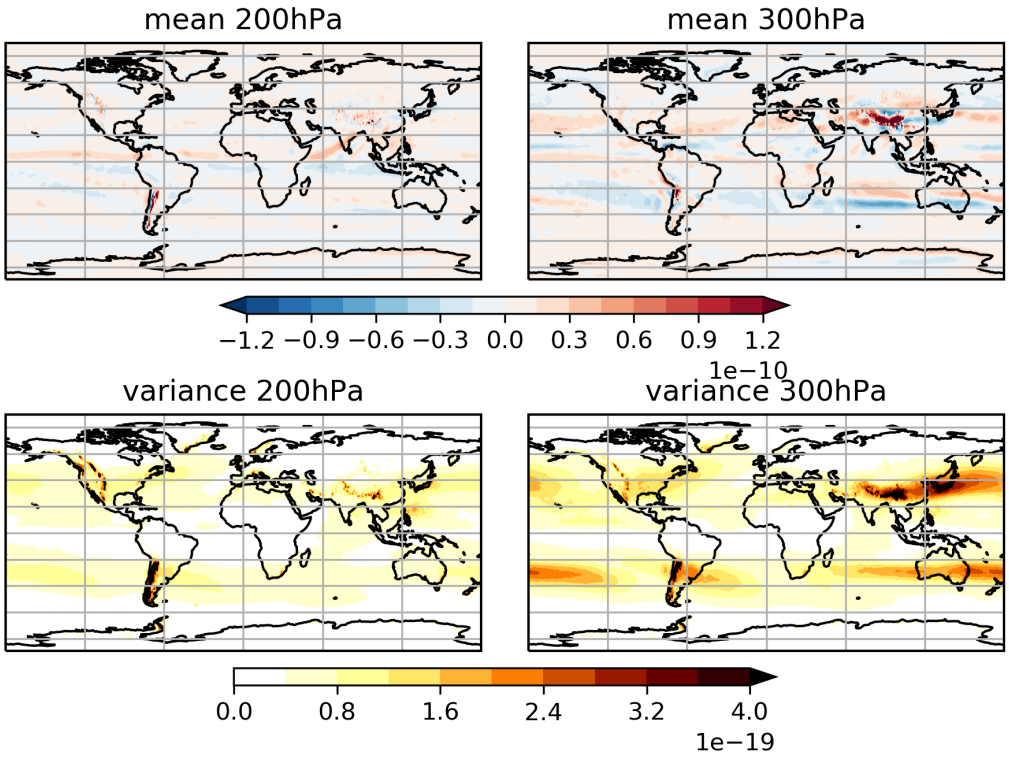

Figure 5.3.: *Annual mean & variance of daily means of the curl of vertical momentum advection [s^{-2}] at 200hPa & 300hPa from reanalysis smoothed to T42 for the purpose of plotting.*

by meridional vortex tilting, that forces equatorial westerlies. The values at 300hPa are significantly stronger. In addition to the strengthening, the annual mean changes its shape, shifting its maxima polewards. There is no equatorial dipole but one dipole at the descending branch of the Hadley cell on either hemisphere. That is in good agreement with the plot of vertical momentum advection (Fig. 5.1). Also, the variance of daily mean vertical forcing is stronger at 300hPa than at 200hPa. At 300hPa, the westerly jets are regions of strong variability whereas at 200hPa mountain ranges are the only places of considerable variance.

In comparison with the traditional RWS (Fig. 3.1), the curl vertical momentum advection is smaller but non-negligible both in terms of the temporal mean and daily mean variance. At 300hPa, the mean and variance are about one-fourth of the traditional RWS and about one-tenth at 200hPa. Relating these terms more closely to physical phenomena is, therefore, desirable. However, a simple explanation cannot fully explain the physical origin of this vertical vorticity forcing because it can be variability-driven as it includes products of vertical and horizontal velocities. Against this background, the following sketches can only provide some guidance.

Figure (5.4a) shows a latitude-pressure section of a tropical Hadley cell and a subtropical baroclinic jet. By meridional vortex tilting ($\omega_y u_p$), an arrangement like this, symmetric around the equator, could produce one equatorial dipole at 200hPa and one dipole at the descending branch of Hadley cell at 300hPa in each hemisphere. These dipoles would drive

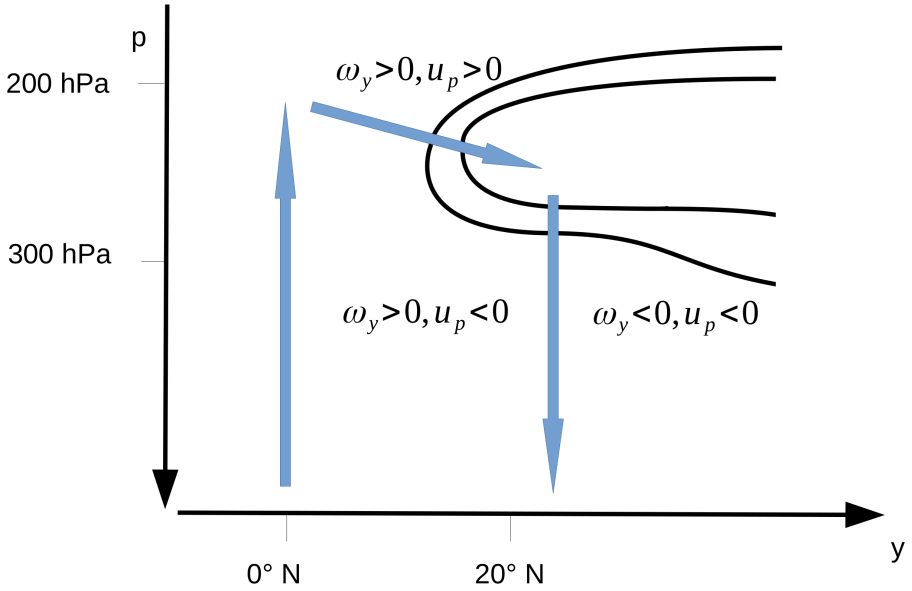

(a) *Meridional vortex tilting in a section of a tropical Hadley cell and a subtropical baroclinic jet.*

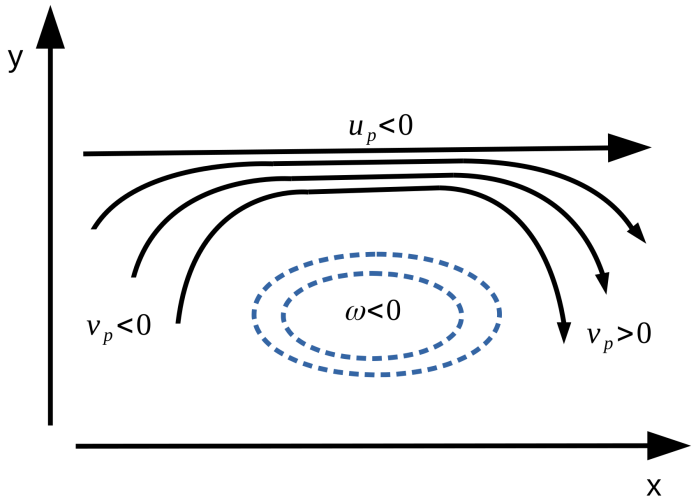

(b) *Vertical vorticity advection and zonal vortex tilting in a horizontal plane with convective ascent and a local maximum of the baroclinic jet.*

Figure 5.4.: *Sketches to provide guidance for the physical origin of the respective terms in the curl of vertical momentum advection. Meridional vortex tilting produces different dipoles at 200hPa and 300hPa. Vertical vorticity advection and zonal vortex tilting have counteracting effects in a region of localised ascent.*

westerly momentum and show how meridional vortex stretching depends critically on the distribution of the vertical gradient u_p. Figure (5.4b) tries to visualize the counteracting effect of zonal vortex tilting ($-\omega_x v_p$) and vertical vorticity advection ($-\omega\zeta_p$) for localised convective ascent ($\omega < 0$), as found for example at the Maritime Continent. A local maximum of the baroclinic, westerly jet is located north of the convective ascent. The jet's velocity is lower at higher pressure levels and, consequently, $(-\omega\zeta_p) > 0$ at the location of the ascent. The local jet maximum is also associated with meridional convergence to the west and meridional divergence to the east. Moreover, the ascent is associated with cyclonic circulation at low levels (Gill, 1980). So, the vertical vorticity advection by the ascend would be balanced by $(-\omega_x v_p) < 0$.

A nonlinear model with the new forcing The model results presented in chapter (3.2) are driven by the traditional RWS only. In light of the relevance of vertical momentum advection, these results will now be compared to model experiments that include the new forcing. More specifically, all experiments were repeated with the sum of both forcings, which will be named *3d_forcing*, or with the curl of vertical momentum advection only, named *vert_forcing*.

A comparison by means of temporal mean, zonal-mean quantities is conducted in figure (5.5). It presents zonal wind and zonal-mean eddy kinetic energy ($\overline{\mathrm{eKE}}$) at 200hPa and 300hPa, comparable to figures (3.10) and (3.11a). The importance of vertical momentum advection is clearly visible. The zonal-mean equatorial easterlies (Fig. 5.5a,b) are reduced by the inclusion of vertical forcing (*3d_forcing* compared to *rws*) at both 200hPa and 300hPa, although they are not completely cured when compared to reanalysis. There is also a small improvement in the extratropics, especially at 300hPa, with a strengthening of the westerlies at 40°N/S and a weakening at 70°N/S. Note that this describes the model configuration with a 12 days linear friction time scale. The model with stronger friction (6 days) still produces extratropical easterlies and is not improved fundamentally by the inclusion of vertical forcing (not shown). Interestingly, the experiments driven by *vert_forcing* without the traditional RWS, show significant zonal-mean zonal wind speeds, too, in both the tropics and extratropics. At 200hPa, equatorial westerlies up to 10 m/s and southern hemispheric extratropical westerlies up to 5 m/s are reached. At 300hPa, equatorial velocities are low but subtropical westerlies and midlatitude easterlies up to 11 m/s can be seen. With a 6 days linear friction time scale, wind velocities due to *vert_forcing* are similar in shape but about half in strength compared to 12 days friction (not shown). To some extent the model results driven by the sum of RWS and vertical forcing can be seen as the sum of the respective model outputs. Take for example the reduction of equatorial zonal-mean easterlies at 200hPa. However, the details are more complex. For example a similar reduction of equatorial easterlies can be seen at 300hPa as well, even though equatorial zonal-mean wind speeds are low when driven by vertical forcing only.

As noted before, time-mean, zonal-mean zonal wind does not change regardless of whether a single realisation of the model is looked at or the ensemble mean. To compare the effect of vertical forcing on forced and internal variability, figures (5.5c,d) show time-mean, zonal-mean eddy kinetic energy of the total flow ($\overline{\mathrm{eKE}}$). The experiments with *vert_forcing* only have significant eddy kinetic energy both in a single realisation of the model and in the ensemble mean. That is more strongly the case at 300hPa than at 200hPa, which is in good

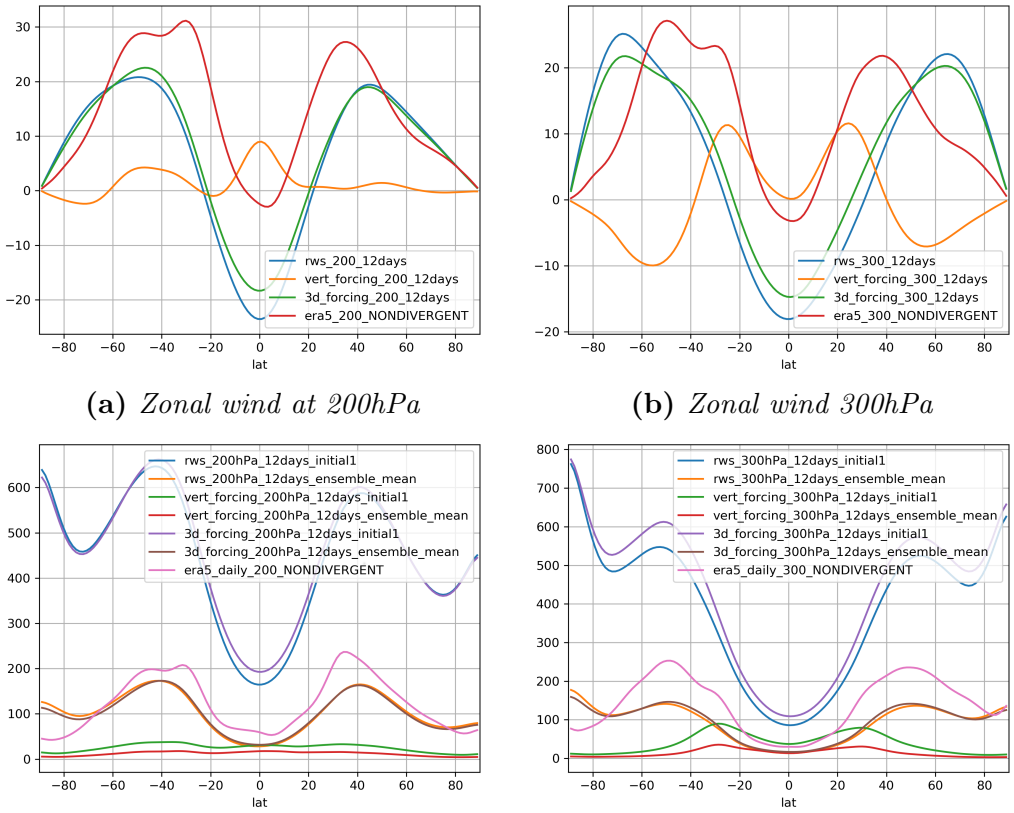

(a) *Zonal wind at 200hPa* **(b)** *Zonal wind 300hPa*

(c) *Eddy kinetic energy at 200hPa* ($\overline{eKE}$) **(d)** *Eddy kinetic energy at 300hPa* ($\overline{eKE}$)

Figure 5.5.: *Time-mean, zonal-mean diagnostics from various model experiments with different forcings and reanalysis at two pressure levels.*

agreement with the variance of vertical forcing (Fig. 5.3). That difference between these two levels holds as well when the model includes the sum of both forcings (*3d_forcing*). However, the increase of eddy kinetic energy with *3d_forcing* does not survive ensemble averaging. That is the case for both the total flow (time mean + transients, Fig. 5.5c,d) and the transient flow (not shown).

A consecutive question could be whether the correction on the mean flow and the energisation of the transient flow due to vertical forcing improves the model performance in terms of temporal coherence. Table (5.1) shows correlations (Spearman' r) of area-averaged kinetic energy of the transient flow (KEzm′ & e′KE) between model and reanalysis. See chapter (3.2) for the introduction of these quantities. Vertical forcing does improve the model performance at 300hPa substantially, most strongly for the extratropical zonal-mean flow, and both for single realisation and the ensemble mean. For example, the correlation of daily mean, ensemble mean extratropical KEzm′ increases from 0.35 to 0.62. In contrast, the change of temporal coherence is negligible at 200hPa. The different responses of the two levels to vertical forcing might be attributed to the much larger variance of vertical forcing at 300hPa (Fig. 5.3). Findings from chapter (3.2), like the good performance of extratropical e′KE on short time scales regardless of ensemble size and the benefit of ensemble

Table 5.1.: *Spearman rank correlation coefficients of area-averaged kinetic energy of the transient flow from model experiments with energies from reanalysis. All correlations are significant to a 99.9% level.*

daily means at 200hPa	90N-20N KEzm′	90N-20N e′KE	20N-20S KEzm′	20N-20S e′KE
3d_forcing_12days_initial1	0.31	0.52	0.23	0.37
3d_forcing_12days_ensembel_mean	0.65	0.58	0.48	0.49
rws_12days_initial1	0.24	0.52	0.25	0.38
rws_12days_ensemble_mean	0.61	0.59	0.47	0.49
90-day means at 200hPa	**90N-20N KEzm′**	**90N-20N e′KE**	**20N-20S KEzm′**	**20N-20S e′KE**
3d_forcing_12days_initial1	0.77	0.48	0.58	0.68
3d_forcing_12days_ensembel_mean	0.84	0.83	0.74	0.82
rws_12days_initial1	0.77	0.54	0.63	0.71
rws_12days_ensemble_mean	0.83	0.82	0.76	0.79
daily means at 300hPa	**90N-20N KEzm′**	**90N-20N e′KE**	**20N-20S KEzm′**	**20N-20S e′KE**
3d_forcing_12days_initial1	0.28	0.78	0.18	0.36
3d_forcing_12days_ensembel_mean	0.62	0.78	0.37	0.42
rws_12days_initial1	0.12	0.74	0.12	0.25
rws_12days_ensemble_mean	0.35	0.75	0.29	0.34
90-day means at 300hPa	**90N-20N KEzm′**	**90N-20N e′KE**	**20N-20S KEzm′**	**20N-20S e′KE**
3d_forcing_12days_initial1	0.81	0.42	0.53	0.62
3d_forcing_12days_ensembel_mean	0.85	0.71	0.67	0.76
rws_12days_initial1	0.44	0.28	0.42	0.60
rws_12days_ensemble_mean	0.52	0.61	0.57	0.75

averaging on KEzm′, still hold.

All in all, the inclusion of vertical forcing does affect the model output substantially. However, the non-linear model used in this thesis, with widespread deficiencies as discussed in chapter (3.2), might not be appropriate to analyse the effect of the curl of vertical momentum advection in detail. A vorticity equation model linearised about the mean flow would be instructive to compare the signal of the different forcings.

6. Conclusion

This thesis attempts to simulate the large-scale upper-tropospheric flow using a barotropic vorticity equation model and a 41-year long time series of Rossby wave source (RWS) forcing diagnosed from reanalysis. In the model, the realistic RWS is expected to produce a realistic climate by an inverse energy cascade representing the barotropic decay of baroclinic disturbances. The subtropical and eddy-driven jets form waveguides for Rossby wave trains excited by the RWS and are expected to give rise to well-known teleconnections patterns. In particular, this model setup differs from previous barotropic modelling studies that either apply idealised forcing or linearise the model using an initial time step correction. The fully non-linear setup in this thesis is meant to enable the analysis of comprehensive upper-tropospheric variability.

However, the expectation of this model to reproduce the rotational flow from reanalysis cannot be realised. Both the mean state and variance of the modelled flow are deteriorated when compared to reanalysis. More specifically, the mean state westerlies are too weak and their variance is too strong. Model results with strong linear friction (6-day friction time scale) show a lesser amplification of variance than with weak linear friction (12 days). The weakening of the westerlies is, though, more severe and a 12-day linear friction time scale can, thus, be considered the better choice. Using the 12-day time scale, horizontal maps of the climatological zonal wind at 200hPa reveal a reduction of maximum speed to half the value in reanalysis; the variance of daily means is increased more than twice compared to reanalysis. To separate internal and forced variability, ten-member-ensemble experiments have been conducted and the ensemble mean is compared to a single realisation. Ensemble averaging reduces time-mean, zonal-mean eddy kinetic energy successfully to values seen in reanalysis. One can conclude that internal variability, i.e. barotropic instability, is responsible for the deterioration of the climatological mean state in the barotropic model, transferring energy from the mean state into eddy motion. Globally averaged power spectra of vorticity reveal that barotropic instabilities create excess variance on short time scales. Ensemble averaging, however, reduces variance on all time scales.

To increase the understanding of these instabilities, domain-averaged kinetic energies and an NAO index representing regional climate variability from a single realisation of the model and the ensemble mean flow are compared with reanalysis. Interestingly, the model performs very differently from the global than from the regional perspective. From the global perspective, the time series of realistic RWS creates a reasonable temporal coherence between the model and reality seen by the correlations of domain-averaged kinetic energy. The temporal coherence is improved by ensemble averaging and lowpass filtering. This coherence exists despite the instabilities that deteriorate the climatological flow. However, one can speculate that the instabilities create a spatial incoherence of anomalies between the model and reanalysis, but also between individual realisations of the model. That spatial incoherence would give rise to the temporal incoherence in terms of a regional climate index

between the model and reanalysis as demonstrated by the NAO index analysis. Shown by the vorticity spectra, the instabilities increase power in comparison to reanalysis on small time scales. Unfortunately, the resulting deterioration of the flow and the spatial incoherence of anomalies extends to long time scales. So all in all, this model is not well-suited for the analysis of teleconnections.

The unstable nature of the instantaneous, or even the climatological, jets in a barotropic model is an interesting result that might not have received enough attention yet. Many barotropic modelling studies maintain their basic state artificially by applying an initial time step correction (e.g. Simmons, 1982; Hoskins and Ambrizzi, 1993; O'Reilly et al., 2018; Baker et al., 2019). It is not clear what effect that has on the instabilities seen in this thesis. These studies investigate steady-state responses to certain anomalous forcings and, therefore, give no indication of variability in barotropic models. Surprisingly, the barotropic instabilities remain unnoted by Vallis et al. (2004) too, although, they evaluate the same model as used in this thesis with a different forcing only. More specifically, Vallis et al. (2004) apply random stirring of the form of a Markov process exciting a small range of wavenumbers in a meridionally confined region. The amplitude of stirring is tuned to create a zonally averaged eddy-driven jet of 10m/s which is assumed to be representative for the vertically averaged jet. Such a forcing, however, is very different from the upper-tropospheric RWS diagnosed from reanalysis used here. First, its spectral power extends to wavenumbers much larger than those considered by Vallis et al. (2004) (not shown). Second, the zonally-averaged jets in the upper troposphere and in this model are twice to three times larger than the vertical average of 10m/s used by Vallis et al. (2004) to calibrate their model. The influence of small scale forcing is not easily estimated. A smaller jet velocity, however, might be sufficient to suppress barotropic instability. Furthermore, a modelling study that uses random stirring, cannot aim to simulate the Hadley cell's effect driving the subtropical jet, in contrast to the present study in which the subtropical jet is included. Possibly, the instabilities remain unnoticed in such idealised studies concerning the eddy-driven jet because it is the subtropical (baroclinic) jet that is the source of the instability rather than the eddy-driven (barotropic) jet.

Although rarely discussed nowadays, the notion of a barotropically unstable climatological basic state of the upper troposphere is not new. Simmons et al. (1983) find rapidly growing normal modes in a barotropic model that is linearised around a realistic basic state. Specifically, they find that rates of energy conversion depend more strongly on the basic state than on the shape of the applied forcing. The finding of unstable normal modes is then related to the existence of prominent atmospheric teleconnection patterns. Furthermore, Simmons et al. (1983) find a competing influence between barotropic and baroclinic instability and discuss the limits of the barotropic model design. In this thesis, the competing influence of barotropic and baroclinic shear is investigated in a two-level quasi-geostrophic model. This approach is used by James (1987) introducing the barotropic governor, i.e. the suppression of baroclinic instability in a horizontally sheared flow. In the light of the modelling results presented in this study, it is possible that a baroclinic governor suppresses barotropic instability in a baroclinic world. The simple quasi-geostrophic model does not produce a fully convincing picture of a baroclinic governor. However, that model is subject to a number of parameters that still need tuning, most prominently the Rossby radius of deformation.

The model error is unfortunate and limits the use of the barotropic model for teleconnection

studies. However, there might be a lot to be learned from its deficiencies. More specifically, the lack of a baroclinic or barotropic governor could be relevant for the "signal-to-noise paradox" seen in sophisticated seasonal prediction systems. Dunstone et al. (2016) demonstrate that, although, the stochastic behaviour of the NAO restricts predictability, a significant skill can be seen in large-ensemble predictions. Using a 40-member ensemble they find skill predicting the NAO index with $r = 0.41$ and $p = 0.01$ in retrospective forecasts that are initialized 13 months ahead. The skill depends critically on ensemble size and, though, skill is large, the amplitude of the signal in the ensemble mean is too weak compared to observations. Actually, the ensemble mean is more strongly correlated with observations than with individual ensemble members. The co-occurrence of large skill and a small signal-to-noise ratio indicates an underestimation of predictability by the model (Eade et al., 2014). This behaviour is referred to as a "signal-to-noise paradox" and has received much attention ever since. Based on a simple toy model, Strommen and Palmer (2019) raise the hypothesis that a low signal-to-noise ratio accompanying significant prediction skill can be explained by reduced regime persistence in forecast models. They identify potential sources for that lack of persistence. Among those is the assumption that excess inherent stochasticity quickly causes regime transitions. Unsuppressed barotropic or baroclinic instability gives a reason for excess stochasticity.

Admittedly, the NAO index simulated by this barotropic model cannot serve as an analogy to the "signal-to-noise paradox" in the hindcasts by Dunstone et al. (2016) because its correlation with reanalysis is so low. However, the lowpass-filtered domain-averaged kinetic energies show reasonable temporal coherence with reanalysis but small coherence between individual ensemble members indicated by the small variance of the ensemble mean. Additional analysis would be expedient but it might be still justified to claim that the barotropic model underestimates the information about domain-averaged kinetic energies contained in the RWS diagnosed from reanalysis. The respective reasons for excess internal variability in the idealised barotropic model and sophisticated seasonal prediction systems are most probably diverse. The baroclinic governor of barotropic instability and the effect of its absence in a barotropic model may simply serve as an analogy for systematic errors in modern climate models, although, it might be worth investigating the influence of baroclinic shear or vertical resolution on barotropic instability in atmospheric general circulation models. Excess internal variability due to absent "governors" can remain unnoticed due to over-tuning of dissipation schemes. The study by James and Gray (1986) may serve as an example since they find suppressed baroclinic instability in a numerical model when the surface drag is reduced.

Another interesting result of this thesis is the incompleteness of the traditional RWS that contains vortex stretching and horizontal advection of vorticity by the divergent flow as defined by Sardeshmukh and Hoskins (1988). It is found that permitting horizontal divergence but neglecting the curl of vertical momentum advection is inconsistent with the conservation of mass and that, consequently, the horizontal momentum equations cannot be written in flux form. More specifically, neglecting vertical advection is equivalent to omitting the momentum flux convergence $[u_\chi v_\chi]_y$ by divergent velocities u_χ and v_χ in the zonal-mean zonal momentum equation, which proves important for the tropical momentum flux balance. A more complete RWS for the upper-troposphere has to include the curl of vertical momentum advection, i.e. the contributions due to vortex tilting and vertical

vorticity advection. The new terms offer more ways for a range of baroclinic processes to interact with the rotational flow. This is particularly relevant in the tropics where values of the traditional RWS remain low. On the one hand, the new formulation of RWS constitutes an improved forcing for barotropic modelling studies. But it is also relevant for statistical analyses that, for example, try to attribute predictability of teleconnections to tropical phenomena (e.g. Scaife et al., 2017). A sound quantification of the influence of the curl of vertical momentum advection is, therefore, important.

Driven by the traditional RWS, the non-linear barotropic model shows strong equatorial easterlies. These easterlies are reduced when the model is forced by the more complete Rossby wave source including vortex tilting and vertical vorticity advection. However, the instabilities seen in a fully non-linear barotropic model compromise the analysis of the new forcing and a linearised model might be useful. It would facilitate a decomposition of the mean flow into contributions by eddy fluxes and the respective terms of the RWS. Furthermore, a linearised model could shed light on the extratropical response to tropical phenomena, a question particularly relevant for seasonal to sub-seasonal weather prediction. One could investigate the anomalous flow caused by typical RWS patterns associated with ENSO, the MJO, or the QBO (quasi-biennial oscillation). It would also be interesting to see how the RWS regressed on extratropical indices like the NAO or PNA is related to these phenomena.

All in all, reproducing the rotational flow from reanalysis in a simplified dynamical model is more difficult than expected. Theoretically, all influence of the divergent on the rotational flow should be included in the RWS. However, in this numerical model the RWS cannot be calculated interactively by specifying the divergent flow only because with that procedure the model grows numerically unstable. One might expect that directly specifying reanalysis' RWS would improve model performance but a non-interactive vortex stretching appears to be a severe idealization. In addition to that, there is no feedback of the rotational on the divergent flow in the model. On the other hand, a comparison between a simplified barotropic model and an atmospheric reanalysis product that is based on a much more complex model including moist thermodynamics, clouds, etc. and involves the assimilation of observational data, might be uneven and the comparison with a baroclinic dry dynamical model more appropriate. In fact, diagnosing the RWS from a simple baroclinic model instead of reanalysis could be useful to analyse the baroclinic governor of barotropic instability in more detail. More specifically, an idealised baroclinic model setup with more control on the shape of the flow could allow to identify the part of the flow that is barotropically stable in a baroclinic but unstable in a barotropic model. In this study, there is some evidence that it is the subtropical or zonal-mean jet which is subject to a baroclinic governor. Furthermore, it would be interesting to examine the radius of deformation thoroughly to evaluate the importance of interactive vortex stretching. The barotropic governor in comparison to the baroclinic governor could be investigated following James and Gray (1986) by means of the response to a differently sized surface drag.

List of Figures

List of Acronyms and Symbols

Acronyms

BVE	barotropic vorticity equation
CDO	climate data operators
CFL	Courant-Friedrichs-Lewy
DJF	December, January, and February
eKE	eddy kinetic energy
ENSO	El Niño Southern Osciallation
FFT	fast Fourier transfrom
ECMWF	European Centre for Medium-Range Weather Forecasts
EOF	empirical orthogonal function
ERA5	fifth generation of ECMWF atmospheric reanalysis
GFDL	Geophysical Fluid Dynamics Laboratory
IFS	Integrated Forecasting System
ITCZ	Intertropical Convergence Zone
JJA	June, July, and August
KEzm	kinetic energy of the zonal-mean flow
MAM	March, April, and May
MJO	Madden-Julian Oscillation
NAO	North Atlantic Oscillation
NetCDF	Network Common Data Format
PNA	Pacific-North American pattern
PSD	power spectral density
QBO	quasi-biennial oscillation
RWS	Rossby wave source
SON	September, October, and November
T85	triangular truncation at wavenumber 85

vert_forcing	curl of vertical momentum advection
WKBJ	Wentzel–Kramers–Brillouin-Jeffreys
3d_forcing	sum of traditional RWS & curl of vertical momentum advection

Symbols

$\frac{D}{Dt}$	material derivative
$_x$	partial derivative with respect to longitude
$_y$	partial derivative with respect to latitude
$_p$	partial derivative with respect to pressure
∇	Nabla operator
∇_h	horizontal Nabla operator
∇^2	Laplace operator
$\vec{e}$	unit vector
u	zonal velocity
v	meridional velocity
ω	vertical velocity / angular frequency
ψ	stream function
$\vec{u}_\psi$	rotational (nondivergent) flow
ζ	relative vorticity
f	Coriolis parameter
β	meridional gradient of Coriolis parameter
q	absolute vorticity / potential vorticity
χ	velocity potential
$\vec{u}_\chi$	divergent (irrotational) flow
Φ	geopotential
U	typical velocity scale
$\overline{}$	temporal mean / basic state
$'$	deviation from temporal mean /basic state
$[\ ]$	zonal mean
*	deviation from zonal mean

c	zonal phase velocity / gravity wave speed
c_g	group velocity
k	plane wave zonal wavenumber
l	plane wave meridional wavenumber / total wavenumber of spherical harmonic
k_i	scale of energy input
r	linear friction coefficient / correlation coefficient
κ	biharmonic viscosity
λ	longitude / inverse radius of deformation
θ	latitude
a	radius of sphere / width of Gaussian jet
μ	$\mu = \sin\theta$
$Y_{l,m}$	spherical harmonic with wavenumbers l and m
m	zonal wavenumber of spherical harmonic
n	meridional wavenumber of spherical harmonic / time step index
$\widetilde{\ }$	spectral space / non-dimensional
N	number of meridional gridpoints
ξ	meridional amplitude function of normal mode
ϵ	small parameter / amplitude of Gaussian jet
$\Re$	real part
$\Im$	imaginary part
γ	Robert-Asselin filtering coefficient

A. Appendix

This appendix holds information on the derivation of some equations that is omitted in the chapters above for the sake of readability:

Two-layer quasi-geostrophic model In chapter (4), a two-layer quasi-geostrophic model is used to investigate growth rates of normal mode solutions for a set of different basic-state wind profiles. The governing equations (4.5) are given in non-dimensional form. Without non-dimensionalising they take the form

$$\begin{aligned}\sigma\left[\left(\frac{\partial^2}{\partial y^2}-k^2-\lambda^2\right)\xi_1+\lambda^2\xi_3\right] =& kU_1\left[\left(\frac{\partial^2}{\partial y^2}-k^2-\lambda^2\right)\xi_1+\lambda^2\xi_3\right] \\ &+k\xi_1\left[\beta-U_{1yy}+\lambda^2(U_1-U_3)\right]\end{aligned} \tag{A.1a}$$

$$\begin{aligned}\sigma\left[\left(\frac{\partial^2}{\partial y^2}-k^2-\lambda^2\right)\xi_3+\lambda^2\xi_1\right] =& kU_3\left[\left(\frac{\partial^2}{\partial y^2}-k^2-\lambda^2\right)\xi_3+\lambda^2\xi_1\right] \\ &+k\xi_3\left[\beta-U_{3yy}+\lambda^2(U_3-U_1)\right]\end{aligned} \tag{A.1b}$$

These can be written as a matrix equation when discretized on N meridional gridpoints using the centred differences-approximation with a grid point interval of $\Delta y = 2Y/(N+1)$. For the non-dimensional problem the matrix equation is given by (4.6). It includes a vector $\vec{F}$ and matrices $\underline{A}$ and $\underline{B}$. More specifically

$$\vec{F} = \begin{pmatrix} \xi_{1,1} \\ \vdots \\ \xi_{1,N} \\ \xi_{3,1} \\ \vdots \\ \xi_{3,N} \end{pmatrix} \tag{A.2}$$

The matrix $\underline{B}$ has entries:

- $-\frac{2}{(\Delta\tilde{y})^2}-\widetilde{k}^2-1$ on the main diagonal
- $\frac{1}{(\Delta\tilde{y})^2}$ on the two neighboring diagonals
- 1 on the main diagonals of the upper right and lower left quadrant

The matrix $\underline{A}$ can be expressed with diagonal matrices $\underline{D1}$ and $\underline{D2}$ and matrix $\underline{B}$ by

$$\underline{A} = \widetilde{k}\underline{D1}\,\underline{B} + \widetilde{k}\left[(\widetilde{\beta}-\widetilde{U}_{j\tilde{y}\tilde{y}})\underline{1}+\underline{D2}\right] \tag{A.3}$$

with

$$\underline{D1} = \begin{pmatrix} \widetilde{U}_1 & & & & & \\ & \ddots & & & & \\ & & \widetilde{U}_1 & & & \\ & & & \widetilde{U}_3 & & \\ & & & & \ddots & \\ & & & & & \widetilde{U}_3 \end{pmatrix} \tag{A.4}$$

$$\underline{D2} = \begin{pmatrix} \widetilde{U}_1 - \widetilde{U}_3 & & & & & \\ & \ddots & & & & \\ & & \widetilde{U}_1 - \widetilde{U}_3 & & & \\ & & & \widetilde{U}_3 - \widetilde{U}_1 & & \\ & & & & \ddots & \\ & & & & & \widetilde{U}_3 - \widetilde{U}_1 \end{pmatrix} \tag{A.5}$$

There are analytic expressions for $\widetilde{U}_{j\tilde{y}\tilde{y}}$ for the wind profiles used in this thesis . The non-dimensional normal mode growth rates $\Im(\tilde{\sigma})$ can be found by calculating the eigenvalues of $\underline{B}^{-1}\underline{A}$. Inverting the matrix $\underline{B}$, multiplicating matrices, and solving the eigenvalue problem can be done easily with the python module`numpy.linalg`*.

Flux form of zonal-mean zonal momentum equations As discussed in chapter (5.1), permitting horizontal divergence but neglecting vertical advection is inconsistent with the continuity equation (5.1). Due to this inconsistency the zonal-mean zonal momentum equation cannot easily be written in flux form. In the following a detailed transformation of the advective formulation (5.4b) into a flux form-like equation (5.4c) is presented:

$$\begin{aligned}
[u_t] &= -[v_\psi u_{\psi,y}] - [v_\psi u_{\chi,y}] - [v_\chi u_{\psi,y}] + f[v_\chi] && \text{(A.6a)}\\
&= -[v_\psi u_{\psi,y}] - [v_\psi u_{\chi,y}] - [v_\chi u_{\psi,y}] + f[v_\chi] - [u_\psi(u_{\chi,x} + v_{\chi,y} + \omega_p)] && \text{(A.6b)}\\
&= -[v_\psi u_{\psi,y}] - [v_\psi u_{\chi,y}] - [v_\chi u_\psi]_y - [u_\psi u_{\chi,x}] - [u_\psi \omega_p] + f[v_\chi] && \text{(A.6c)}\\
&= -[v_\psi u_\psi]_y + [u_\psi v_{\psi,y}] - [v_\psi u_\chi]_y + [u_\chi v_{\psi,y}] - [v_\chi u_\psi]_y - [u_\psi u_{\chi,x}] \\
&\quad - [u_\psi \omega_p] + f[v_\chi] && \text{(A.6d)}\\
&= -[v_\psi u_\psi]_y - [u_\psi u_{\psi,x}] - [v_\psi u_\chi]_y - [u_\chi u_{\psi,x}] - [v_\chi u_\psi]_y - [u_\psi u_{\chi,x}] \\
&\quad - [u_\psi \omega_p] + f[v_\chi] && \text{(A.6e)}\\
&= -[v_\psi u_\psi]_y - [u_\psi u_{\psi,x}] - [v_\psi u_\chi]_y - [v_\chi u_\psi]_y - [(u_\psi u_\chi)_x] - [u_\psi \omega_p] + f[v_\chi] && \text{(A.6f)}\\
&= -[v_\psi u_\psi]_y - [u_\psi u_{\psi,x}] - [v_\psi u_\chi]_y - [v_\chi u_\psi]_y - [u_\psi \omega_p] + f[v_\chi] && \text{(A.6g)}\\
&= -[v_\psi u_\psi]_y - [v_\psi u_\chi]_y - [v_\chi u_\psi]_y - [\omega_p u_\psi] + f[v_\chi] && \text{(A.6h)}
\end{aligned}$$

These seven steps involve adding the continuity equation multplied by $(-u_\psi)$, the product rule of differentiation to write $[v_\chi u_\psi]_y$, the product rule to write $[v_\psi u_\psi]_y$ & $[v_\psi u_\chi]_y$, identity

*see `https://numpy.org/doc/stable/reference/routines.linalg.html`

(5.2a), the product rule to write $[(u_\psi u_\chi)_x]$, identity (5.2e), and finally identity (5.2f) with u_ψ instead of u. When vertical advection is included, one obtains the complete flux form:

$$
\begin{aligned}
[u_t] =& -[v_\psi u_{\psi,y}] - [v_\psi u_{\chi,y}] - [v_\chi u_{\psi,y}] - [\omega u_p] + f[v_\chi] && \text{(A.7a)}\\
=& -[v_\psi u_{\psi,y}] - [v_\psi u_{\chi,y}] - [v_\chi u_{\psi,y}] - [\omega u_p] + f[v_\chi] - [u(u_{\chi,x} + v_{\chi,y} + \omega_p)] && \text{(A.7b)}\\
=& -[v_\psi u_{\psi,y}] - [v_\psi u_{\chi,y}] - [v_\chi u_\psi]_y - [u u_{\chi,x}] - [u_\chi v_{\chi,y}] - [\omega u]_p + f[v_\chi] && \text{(A.7c)}\\
=& -[v_\psi u_{\psi,y}] - [v_\psi u_{\chi,y}] - [v_\chi u_\psi]_y - [u u_{\chi,x}] - [u_\chi v_{\chi,y}] - [v_\chi u_{\chi,y}] \\
& - [\omega u]_p + f[v_\chi] && \text{(A.7d)}\\
=& -[v_\psi u_\psi]_y + [v_{\psi,y} u_\psi] - [v_\psi u_\chi]_y + [v_{\psi,y} u_\chi] - [v_\chi u_\psi]_y - [u u_{\chi,x}] - [v_\chi u_\chi]_y \\
& - [\omega u]_p + f[v_\chi] && \text{(A.7e)}\\
=& -[v_\psi u_\psi]_y - [u_{\psi,x} u_\psi] - [v_\psi u_\chi]_y - [u_{\psi,x} u_\chi] - [v_\chi u_\psi]_y - [u u_{\chi,x}] - [v_\chi u_\chi]_y \\
& - [\omega u]_p + f[v_\chi] && \text{(A.7f)}\\
=& -[v_\psi u_\psi]_y - [v_\psi u_\chi]_y - [u_{\psi,x} u] - [v_\chi u_\psi]_y - [u u_{\chi,x}] - [v_\chi u_\chi]_y - [\omega u]_p + f[v_\chi] && \text{(A.7g)}\\
=& -[v_\psi u_\psi]_y - [v_\psi u_\chi]_y - [v_\chi u_\psi]_y - [u u_x] - [v_\chi u_\chi]_y - [\omega u]_p + f[v_\chi] && \text{(A.7h)}\\
=& -[v_\psi u_\psi]_y - [v_\psi u_\chi]_y - [v_\chi u_\psi]_y - [v_\chi u_\chi]_y - [\omega u]_p + f[v_\chi] && \text{(A.7i)}
\end{aligned}
$$

These eight steps involve adding the continuity equation muliplied by $(-u)$, the product rule to write $[v_\chi u_\psi]_y$ & $[\omega u]_p$, adding equation (5.3), the product rule to write $[v_\psi u_\psi]_y$ & $[v_\psi u_\chi]_y$, identity (5.2a), combining $[u_{\psi,x} u_\psi]$ & $[u_{\psi,x} u_\chi]$, combining $[u_{\psi,x} u]$ & $[u_{\chi,x} u]$, and finally identity (5.2f). It become visible that zonal-mean vertical momentum advection equals the difference between (5.4c) and (5.6c):

$$
\begin{aligned}
& -[\omega u_p] && \text{(A.8a)}\\
=& -[\omega u_{\psi,p}] - [\omega u_{\chi,p}] && \text{(A.8b)}\\
=& -[\omega u_{\psi,p}] - [\omega u_{\chi,p}] - [u_\chi(u_{\chi,x} + v_{\chi,y} + \omega_p)] && \text{(A.8c)}\\
=& -[\omega u_{\psi,p}] - [\omega u_\chi]_p - [u_\chi u_{\chi,x}] - [u_\chi v_{\chi,y}] && \text{(A.8d)}\\
=& -[\omega u_{\psi,p}] - [\omega u_\chi]_p - [u_\chi v_{\chi,y}] && \text{(A.8e)}\\
=& -[\omega u_{\psi,p}] - [\omega u_\chi]_p - [u_\chi v_{\chi,y}] - [v_\chi v_{\chi,x}] && \text{(A.8f)}\\
=& -[\omega u_{\psi,p}] - [\omega u_\chi]_p - [u_\chi v_{\chi,y}] - [v_\chi u_{\chi,y}] && \text{(A.8g)}\\
=& -[\omega u_{\psi,p}] - [\omega u_\chi]_p - [v_\chi u_\chi]_y && \text{(A.8h)}
\end{aligned}
$$

These seven steps involve decomposing u_p, adding the continuity equation muliplied by $(-u_\chi)$, the product rule to write $[\omega u_\chi]_p$, identity (5.2f) with u_χ instead of u, identity (5.2f) with v_χ instead of u, identity (5.2b), and finally the product rule to write $[v_\chi u_\chi]_y$.

Bibliography

Asselin, R. et al. (1972). Frequency filter for time integrations. *Mon. Wea. Rev*, 100(6):487–490.

Baker, H. S., Woollings, T., Mbengue, C., Allen, M. R., O'Reilly, C. H., Shiogama, H., and Sparrow, S. (2019). Forced summer stationary waves: the opposing effects of direct radiative forcing and sea surface warming. *Climate Dynamics*, 53(7-8):4291–4309.

Barnes, E. A., Hartmann, D. L., Frierson, D. M., and Kidston, J. (2010). Effect of latitude on the persistence of eddy-driven jets. *Geophysical Research Letters*, 37(11):1–5.

Barnston, A. G. and Livezey, R. E. (1987). Classification, seasonality and persistence of low-frequency atmospheric circulation patterns. *Monthly Weather Review*, 115(6):1083–1126.

Baxter, S. and Nigam, S. (2013). A subseasonal teleconnection analysis: PNA Development and Its relationship to the NAO. *Journal of Climate*, 26(18):6733–6741.

Charney, J. G. (1971). Geostrophic turbulence. *Journal of the Atmospheric Sciences*, 28(6):1087–1095.

Dawson, A. (2016). Windspharm: A High-Level Library for Global Wind Field Computations Using Spherical Harmonics. *Journal of Open Research Software*, 4(1).

Deser, C. (2000). On the teleconnectivity of the 'Arctic Oscillation'. *Geophysical Research Letters*, 27(6):779–782.

Dima, I. M., Wallace, J. M., and Kraucunas, I. (2005). Tropical zonal momentum balance in the NCEP reanalyses. *Journal of the Atmospheric Sciences*, 62(7 II):2499–2513.

Dommenget, D. and Latif, M. (2002). A cautionary note on the interpretation of eofs. *Journal of climate*, 15(2):216–225.

Dunstone, N., Smith, D., Scaife, A., Hermanson, L., Eade, R., Robinson, N., Andrews, M., and Knight, J. (2016). Skilful predictions of the winter north atlantic oscillation one year ahead. *Nature Geoscience*, 9(11):809–814.

Durran, D. R. (1991). The third-order adams-bashforth method: An attractive alternative to leapfrog time differencing. *Monthly weather review*, 119(3):702–720.

Durran, D. R. (2010). *Numerical methods for fluid dynamics: With applications to geophysics*. Springer.

Eade, R., Smith, D., Scaife, A., Wallace, E., Dunstone, N., Hermanson, L., and Robinson, N. (2014). Do seasonal-to-decadal climate predictions underestimate the predictability of the real world? *Geophysical Research Letters*, 41(15):5620–5628.

Gill, A. E. (1980). Some simple solutions for heat-induced tropical circulation. *Quarterly Journal of the Royal Meteorological Society*, 106(449):447–462.

Gollan, G. and Greatbatch, R. J. (2015). On the extratropical influence of variations of the

upper-tropospheric equatorial zonal-mean zonal wind during boreal winter. *Journal of Climate*, 28(1):168–185.

Held, I. M. and Hou, A. Y. (1980). Nonlinear axially symmetric circulations in a nearly inviscid atmosphere. *Journal of the Atmospheric Sciences*, 37(3):515–533.

Held, I. M. and Phillips, P. J. (1987). Linear and nonliear barotropic decay on the sphere. *Journal of the atmospheric sciences*, 44(1):200–207.

Hersbach, H., Bell, B., Berrisford, P., Horányi, A., Sabater, J. M., Nicolas, J., Radu, R., Schepers, D., Simmons, A., Soci, C., et al. (2019). Global reanalysis: goodbye era-interim, hello era5. *ECMWF Newsl*, 159:17–24.

Holton, J. and Hakim, G. (2013). *An introduction to dynamic meteorology*. Academic Press.

Horel, J. D. and Wallace, J. M. (1981). Planetary-scale atmospheric phenomena associated with the southern oscillation. *Monthly Weather Review*, 109(4):813–829.

Hoskins, B., Neale, R., Rodwell, M., and Yang, G. Y. (1999). Aspects of the large-scale tropical atmospheric circulation. *Tellus, Series B: Chemical and Physical Meteorology*, 51(1 SPEC. ISS.):33–44.

Hoskins, B. J. and Ambrizzi, T. (1993). Rossby wave propagation on a realistic longitudinally varying flow. *Journal of the Atmospheric Sciences*, 50(12):1661–1671.

Hoskins, B. J. and Karoly, D. J. (1981). The steady linear response of a spherical atmosphere to thermal and orographic forcing. *Journal of the Atmospheric Sciences*, 38(6):1179–1196.

Hurrell, J. W. and Deser, C. (2010). North atlantic climate variability: the role of the north atlantic oscillation. *Journal of marine systems*, 79(3-4):231–244.

James, I. and Gray, L. (1986). Concerning the effect of surface drag on the circulation of a baroclinic planetary atmosphere. *Quarterly Journal of the Royal Meteorological Society*, 112(474):1231–1250.

James, I. N. (1987). Suppression of baroclinic instability in horizontally sheared flows. *Journal of the Atmospheric Sciences*, 44(24):3710–3720.

Jansen, M. F., Held, I. M., Adcroft, A., and Hallberg, R. (2015). Energy budget-based backscatter in an eddy permitting primitive equation model. *Ocean Modelling*, 94:15–26.

Kantha, L. H. and Clayson, C. A. (2000). *Numerical models of oceans and oceanic processes*. Elsevier.

Kolmogorov, A. N. (1941). Dissipation of energy in locally isotropic turbulence. *Akademiia Nauk SSSR Doklady*, 32:16.

Kraichnan, R. H. (1967). Inertial ranges in two-dimensional turbulence. *The Physics of Fluids*, 10(7):1417–1423.

Krishnamurti, T., Bedi, H., and Hardiker, V. (1998). *An introduction to global spectral modeling*. Oxford University Press, New York.

Lee, S. (1999). Why are the climatological zonal winds easterly in the equatorial upper troposphere? *Journal of the Atmospheric Sciences*, 56(10):1353–1364.

Lilly, D. K. (1969). Numerical simulation of two-dimensional turbulence. *Physics of Fluids*, 12(12):II–240.

Lindborg, E. (2015). A helmholtz decomposition of structure functions and spectra calculated from aircraft data. *Journal of Fluid Mechanics*, 762:R4.

Lorenz, E. N. (1963). Deterministic nonperiodic flow. *Journal of the atmospheric sciences*, 20(2):130–141.

Mak, M. (2011). *Atmospheric dynamics*. Cambridge University Press.

Maltrud, M. and Vallis, G. (1991). Energy spectra and coherent structures in forced two-dimensional and beta-plane turbulence. *Journal of Fluid Mechanics*, 228:321–342.

Marshall, J., Adcroft, A., Hill, C., Perelman, L., and Heisey, C. (1997). A finite-volume, incompressible navier stokes model for studies of the ocean on parallel computers. *Journal of Geophysical Research: Oceans*, 102(C3):5753–5766.

Messinger, J. and Arakawa, A. (1976). Numerical methods used in atmospheric models. *GARP Publ., 17, World Meteorol. Org.*

O'Reilly, C. H., Woollings, T., Zanna, L., and Weisheimer, A. (2018). The impact of tropical precipitation on summertime euro-Atlantic circulation via a circumglobal wave train. *Journal of Climate*, 31(16):6481–6504.

Rhines, P. B. (1975). Waves and turbulence on a beta-plane. *Journal of Fluid Mechanics*, 69(3):417–443.

Rhines, P. B. (1979). Geostrophic Turbulence. *Annual Review of Fluid Mechanics*, 11(1):401–441.

Robert, A. J. (1966). The integration of a low order spectral form of the primitive meteorological equations. *Journal of the Meteorological Society of Japan. Ser. II*, 44(5):237–245.

Rossby, C. (1939). elations between variations in the intensity of the zonal circulation of the atmosphere and the displacements of the semipermanent centers of action. *J. Mar. Res*, 3:38–55.

Sardeshmukh, P. D. and Hoskins, B. J. (1988). The generation of global rotational flow by steady idealized tropical divergence. *Journal of the Atmospheric Sciences*, 45(7):1228–1251.

Scaife, A. A., Comer, R. E., Dunstone, N. J., Knight, J. R., Smith, D. M., MacLachlan, C., Martin, N., Peterson, K. A., Rowlands, D., Carroll, E. B., Belcher, S., and Slingo, J. (2017). Tropical rainfall, Rossby waves and regional winter climate predictions. *Quarterly Journal of the Royal Meteorological Society*, 143(702):1–11.

Simmons, A. (1982). The forcing of stationary wave motion by tropical diabatic heating. *Quarterly Journal of the Royal Meteorological Society*, 108(457):503–534.

Simmons, A., Wallace, J., and Branstator, G. (1983). Barotropic wave propagation and instability, and atmospheric teleconnection patterns. *Journal of the Atmospheric Sciences*, 40(6):1363–1392.

Simmons, A. J. and Hoskins, B. J. (1978). The life cycles of some nonlinear baroclinic waves. *Journal of the Atmospheric Sciences*, 35(3):414–432.

Simmons, A. J. and Hoskins, B. J. (1980). Barotropic influences on the growth and decay of nonlinear baroclinic waves. *Journal of the Atmospheric Sciences*, 37(8):1679–1684.

Smith, D. M., Scaife, A. A., and Kirtman, B. P. (2012). What is the current state of

scientific knowledge with regard to seasonal and decadal forecasting? *Environmental Research Letters*, 7(1):015602.

Strommen, K. and Palmer, T. N. (2019). Signal and noise in regime systems: A hypothesis on the predictability of the north atlantic oscillation. *Quarterly Journal of the Royal Meteorological Society*, 145(718):147–163.

Thuburn, J., Kent, J., and Wood, N. (2014). Cascades, backscatter and conservation in numerical models of two-dimensional turbulence. *Quarterly Journal of the Royal Meteorological Society*, 140(679):626–638.

Vallis, G. K. (2017). *Atmospheric and oceanic fluid dynamics*. Cambridge University Press.

Vallis, G. K., Gerber, E. P., Kushner, P. J., and Cash, B. A. (2004). A mechanism and simple dynamical model of the North Atlantic Oscillation and annular modes. *Journal of the Atmospheric Sciences*, 61(3):269–280.

Von Storch, H. and Zwiers, F. W. (2001). *Statistical analysis in climate research*. Cambridge university press.

Wallace, J. M. and Gutzler, D. S. (1981). Teleconnections in the geopotential height field during the northern hemisphere winter. *Monthly Weather Review*, 109(4):784–812.

Webster, P. J. (1981). Mechanisms determining the atmospheric response to sea surface temperature anomalies. *Journal of the Atmospheric Sciences*, 38(3):554–571.

Erklärung

Hiermit erkläre ich, dass ich die vorliegende Arbeit selbstständig und ohne fremde Hilfe angefertigt und keine anderen als die angegebenen Quellen und Hilfsmittel verwendet habe. Die eingereichte schriftliche Fassung der Arbeit entspricht der auf dem elektronischen Speichermedium.

Name der Datei: Wicker_1014728.pdf

Weiterhin versichere ich, dass diese Arbeit noch nicht als Abschlussarbeit an anderer Stelle vorgelegen hat.

Wolfgang Wicker, Kiel, den 29.05.2020